Antenna and system design for controlled delivery of microwave thermal ablation

by

Hojjatollah Fallahi

B.S., Shiraz University of Technology, 2010
M.S., Tarbiat Modares University, 2013

AN ABSTRACT OF A DISSERTATION

submitted in partial fulfillment of the requirements for the degree

DOCTOR OF PHILOSOPHY

Department of Electrical and Computer Engineering
Carl R. Ice College of Engineering

KANSAS STATE UNIVERSITY
Manhattan, Kansas

2020

Abstract

Microwave ablation is an established minimally invasive modality for thermal ablation of unresectable tumors and other diseases. The goal of a microwave ablation procedure is to deliver microwave power in a manner localized to the targeted tissue, with the objective of raising the target tissue to ablative temperatures (~60 °C). Engineering efforts in microwave applicator design have largely been focused on the design of microwave antennas that yield large, near-spherical ablation zones, and can fit within rigid needles or flexible catheters. These efforts have led to significant progress in the development and clinical application of microwave ablation systems, particularly for treating tumors in the liver and other highly vascular organs. However, currently available applicator designs are ill-suited to treating targets of diverse shapes and sizes. Furthermore, there are a lack of non-imaging-based techniques for monitoring the transient progression of the ablation zone as a means for providing feedback to the physician. This dissertation presents the design, implementation, and experimental evaluation of microwave ablation antennas for site-specific therapeutic applications with these issues in mind.

A deployable 915 MHz loop antenna is presented, providing a minimally-invasive approach for thermal ablation of the endometrial lining of the uterus for treatment of heavy menstrual bleeding. The antenna incorporates a radiating loop, which can be deployed to adjustable shapes within the uterine cavity, and a passive element, to enable

thermal ablation, to 5.7–9.6 mm depth, of uterine cavities ranging in size from 4–6.5 cm in length and 2.5–4.5 cm in width. Electromagnetic–bioheat transfer simulations were employed for design optimization of the antennas, and proof-of-concept applicators were fabricated and extensively evaluated in *ex vivo* tissue. Finally, feasibility of using the broadband antenna reflection coefficient for monitoring the ablation progress during the course of ablation was evaluated. Experimental studies demonstrated a shift in antenna resonant frequency of 50 MHz correlated with complete ablation.

For treatment of 1–2 cm spherical targets, water-cooled monopole antennas operating at 2.45 and 5.8 GHz were designed and experimentally evaluated in *ex vivo* tissue. The technical feasibility of using these applicators for treating 1–2 cm diameter benign adrenal adenomas was demonstrated. These studies demonstrated the potential of using minimally-invasive microwave ablation applicators for treatment of hypertension caused by benign aldosterone producing adenomas.

Since tissue dielectric properties have been observed to change substantially at elevated temperatures, knowledge of the temperature-dependence of tissue dielectric properties may provide a means for estimating treatment state from changes in antenna reflection coefficient during a procedure. The broadband dielectric properties of bovine liver, an established tissue for experimental characterization of microwave ablation applicators, were measured from room temperature to ablative temperatures. The measured dielectric data were fit to a parametric model using piecewise linear functions,

providing a means for readily incorporating these data into computational models. These data represent the first report of changes in broadband dielectric properties of liver tissue at ablative temperatures and should help enable additional studies in ablation system development.

Antenna and system design for controlled delivery of microwave thermal ablation

by

Hojjatollah Fallahi

B.S., Shiraz University of Technology, 2010
M.S., Tarbiat Modares University, 2013

A DISSERTATION

submitted in partial fulfillment of the requirements for the degree

DOCTOR OF PHILOSOPHY

Department of Electrical and Computer Engineering
Carl R. Ice College of Engineering

KANSAS STATE UNIVERSITY
Manhattan, Kansas

2020

Approved by:

Major Professor
Dr. Punit Prakash

Copyright

Abstract

Microwave ablation is an established minimally invasive modality for thermal ablation of unresectable tumors and other diseases. The goal of a microwave ablation procedure is to deliver microwave power in a manner localized to the targeted tissue, with the objective of raising the target tissue to ablative temperatures (~60 °C). Engineering efforts in microwave applicator design have largely been focused on the design of microwave antennas that yield large, near-spherical ablation zones, and can fit within rigid needles or flexible catheters. These efforts have led to significant progress in the development and clinical application of microwave ablation systems, particularly for treating tumors in the liver and other highly vascular organs. However, currently available applicator designs are ill-suited to treating targets of diverse shapes and sizes. Furthermore, there are a lack of non-imaging-based techniques for monitoring the transient progression of the ablation zone as a means for providing feedback to the physician. This dissertation presents the design, implementation, and experimental evaluation of microwave ablation antennas for site-specific therapeutic applications with these issues in mind.

A deployable 915 MHz loop antenna is presented, providing a minimally-invasive approach for thermal ablation of the endometrial lining of the uterus for treatment of heavy menstrual bleeding. The antenna incorporates a radiating loop, which can be deployed to adjustable shapes within the uterine cavity, and a passive element, to enable

thermal ablation, to 5.7–9.6 mm depth, of uterine cavities ranging in size from 4–6.5 cm in length and 2.5–4.5 cm in width. Electromagnetic–bioheat transfer simulations were employed for design optimization of the antennas, and proof-of-concept applicators were fabricated and extensively evaluated in *ex vivo* tissue. Finally, feasibility of using the broadband antenna reflection coefficient for monitoring the ablation progress during the course of ablation was evaluated. Experimental studies demonstrated a shift in antenna resonant frequency of 50 MHz correlated with complete ablation.

For treatment of 1–2 cm spherical targets, water-cooled monopole antennas operating at 2.45 and 5.8 GHz were designed and experimentally evaluated in *ex vivo* tissue. The technical feasibility of using these applicators for treating 1–2 cm diameter benign adrenal adenomas was demonstrated. These studies demonstrated the potential of using minimally-invasive microwave ablation applicators for treatment of hypertension caused by benign aldosterone producing adenomas.

Since tissue dielectric properties have been observed to change substantially at elevated temperatures, knowledge of the temperature-dependence of tissue dielectric properties may provide a means for estimating treatment state from changes in antenna reflection coefficient during a procedure. The broadband dielectric properties of bovine liver, an established tissue for experimental characterization of microwave ablation applicators, were measured from room temperature to ablative temperatures. The measured dielectric data were fit to a parametric model using piecewise linear functions,

providing a means for readily incorporating these data into computational models. These data represent the first report of changes in broadband dielectric properties of liver tissue at ablative temperatures and should help enable additional studies in ablation system development.

Table of Contents

List of Figures

List of Tables

Acknowledgements

I am grateful to my Advisor Dr. Punit Prakash for his continuous support, encouragement and mentorship during my PhD years. He has guided me in research and inspired me to love and enjoy research. It was a great pleasure to work with him and I learnt a lot from countless discussions I had with him.

I would like to express my appreciation to my dissertation committee: Dr. Steven Warren, Dr. Bill Kuhn and Dr. Warren Beard for their insightful comments and feedback that helped me to improve my dissertation.

Special thanks goes to my friends and fellow labmates at Biomedical Computing and Devices Laboratory: Pegah Faridi, Jan Sebek, Austin Pfannenstiel, Faraz Chamani and Ghina Zia. I really enjoyed working and collaborating with them.

It is my fortune to gratefully acknowledge the support of my dearest friends at K-State: Heman Shakeri, Behnaz Moradi, Mahboobe Jassas, Hamid Rashidi, and Hazhar Sufi Karimi. They were always beside me during the happy and sad moments to encourage and motivate me.

I would like to thank my parents and my siblings who have provided me through moral and emotional support in my life.

Words cannot express how grateful I am to my beloved wife, Sahar Lashkarbolooki, who always supports me with her unconditional love through thick and thin.

Dedication

To Sahar, love of my life.

1 Introduction

1.1 Overview

Thermal ablation is a minimally invasive technique clinically used to destroy diseased tissues by localized heating or freezing for treatment of cancer and other disease. An ideal thermal ablation system may have the following features:

- **Quantifiable:** it should be able to deliver a quantifiable treatment in a localized manner. For example, in heat-based ablations, it is necessary to raise the target tissue temperature to approximately 60 °C while limiting unintended heating of surrounding non-targeted tissue.
- **Controllable:** the system would provide a means for the clinician to adjust the treatment profile, so it can be tailored to targets of varying size and shape.
- **Predictable:** it should be possible to predict the treatment outcome based on the input parameters of the ablation system such as input power and ablation duration as well as the target tissue's physical and physiological properties.
- **Monitoring:** The system should provide a means for monitoring the transient evolution of the treatment.

Ablation procedures are usually performed in an out-patient setting by making a small incision on the body to guide the ablation device toward the target percutaneously or inserting the device into the body through a catheter endoscopically, intravenously, or via body cavities. While ablation has been applied in oncology for destruction of tumors in liver [1], lung [2], kidney [3], bone [4], prostate [5], and brain [6], a variety of ablative systems have been developed for treatment of cardiac arrhythmia [7], Barrett's esophagus [8], menorrhagia [9], and other benign conditions. Ablation may be delivered by a variety of energy modalities, such as radiofrequency, microwaves, ultrasound, laser, freezing (cryoablation), irreversible electroporation, and toxic chemicals.

Radiofrequency devices create ablation zones based on resistive heating (the Joule effect). When the radiofrequency applicator in inserted into the target tissue, high frequency currents (typically at ~460 kHz) from the applicator flow through the surrounding tissue and return to the applicator via another electrode in contact with the body. Direct radiofrequency heating occurs within several millimeters of the electrodes, and the ablation zone grows passively to encompass distant tissue regions via thermal conduction [1].

During a microwave ablation (MWA) procedure (e. g. at 915 MHz or 2.45 GHz), heat is generated by dielectric heating, where the dielectric media is the target tissue. When microwaves travel through tissue, heating occurs because the electromagnetic fields force the polar molecules (e.g. water) in the tissue to oscillate. More heat is generated in

the tissues with higher water content (e.g. solid tumors) while less heat is created in tissues with less water (e.g. fat). Direct microwave heating occurs within the vicinity of the microwave applicator and the rest of the ablation zone is created by thermal conduction [10].

Ultrasound is generated by applying an alternating voltage with a frequency in the range of 6-10 MHz across a piezoelectric material. The resulting ultrasound wave propagates through tissues, causing alternating cycles of increased and reduced pressure (compression and rarefaction, respectively). The pressure fluctuations induced lead to vibration of tissue at a microscopic level, which results in frictional heating. In high intensity focused ultrasound, an array of transducers with input voltages alternating at 0.8-3.5 MHz are employed to focus the ultrasound wave at a given point similar to the focusing of light. During a high intensity focused ultrasound ablation procedure, a high power beam is swept over the target tissue while sparing the surrounding tissues [11], [12].

Destruction of tissue during laser ablation is caused by thermal conversion of focused electromagnetic energy, most commonly at a wavelength of 1064 nm, which raises tissue temperature to lethal levels. The extent of the tissue destruction is dependent on the level of the delivered heat energy and the depth of penetration. Small (800–980 nm) diode lasers are gaining popularity due to their portability, power, and cost effectiveness and water-cooled laser application sheaths are being employed to allow for higher laser power output (50 W) [13], [14].

Cryoablation is the destruction of the target tissue by decreasing the tissue temperature to lower than –40 °C. In modern cryoablation procedures, a high-pressure cryogenic fluid such as argon or nitrogen is circulated through the lumen of thin probes because of its low viscosity. Low pressure within the lumen of the probe results in rapid expansion of the cryogen, which creates a very low temperature (Joule-Thompson effect). This low temperature (<–100 °C) creates an ice ball around the tip of the probe. Clinical cryoablation protocols incorporate multiple freeze – thaw cycles leading to tissue necrosis by a variety of direct and indirect mechanisms. Usually, the freezing interval is rapid and thawing interval is slow in order to maximize the ablation zone. The freeze-thaw cycle is repeated multiple times until achieving the required temperature in the target along with a margin of normal tissue around the tumor [15], [16].

Irreversible electroporation is a novel non-thermal focal ablation technique that uses paired electrodes to deliver a series of short high power electric pulses into a targeted region of tissue, killing the cells by irreversibly disrupting cellular membrane integrity. Currently, 70–90 pulses with pulse width of 70–90 μs and voltage level of 1500 V/cm are used for tumor ablation [17]. The IRE effect is not uniform and depends on the intrinsic conductivity of the tissue, the number of pulses delivered, the current flow achieved, and the total time for the treatment [18].

Chemoablation techniques employ toxic substances, such as ethanol and acetic acid, which are directly injected into the target tissue. Toxicity of the chemical destroys

the target tissue by immediate dehydration of the cytoplasm and protein denaturation. Compared to thermal ablation therapy, devices for chemical ablation therapy are less complicated and are easy to use. However, the challenges in using chemoablation are the toxicity of ablation reagents and inability to control the ablation pattern [19]. A new modality under development is thermochemical ablation where two chemical substances such as alcohol, acid or alkali are injected by syringes to the target site. Upon injection, chemicals mix and generate enough heat to destroy the target [20].

Microwave ablation is distinct from other modalities for thermal therapy application in a number of ways. Microwaves are capable of propagating through tissue of varying biophysical state, including water vapor and charred tissue created during an ablation procedure. Microwave ablation also does not require direct electrical contact of the applicator with the tissue under treatment. Ablation using microwave power can heat tissue to higher temperatures than when using other ablation modalities, enabling the creation of large ablation zones in highly perfused tissues such liver. For these reasons, microwave has become an attractive choice for large volume thermal ablation.

1.2 Overview of microwave ablation systems

MWA systems operating at frequencies of 915 MHz and 2.45 GHz have been developed and are in clinical use for select indications. Applicators have largely been optimized to create large near spherical heating patterns, and are suitable for treating

large tumor volumes in vascular tissue. Physicians have relied on the *ex vivo* ablation size data provided by MWA system manufacturers and preoperative imaging for determining how to set the ablation parameters - input power and duration. There are few methods for monitoring the growth of the ablation zone during the procedure. Therefore, success of the ablation has been heavily dependent on the clinician experience and skill. Although it has been possible to develop these applicators and systems without complete understanding of the microwaves and tissue interaction, development of MWA applicators for applicators other than tumor ablation demands an improved knowledge of microwaves and tissue interaction. Characterization of tissue properties at microwave frequencies also opens an avenue for developing feedback signals from the ablation growth during the course of ablation. Addition of feedback signals from the ablation status to MWA systems could assist clinicians in devising more effective treatment plans.

1.3 Research approach

To address the above-mentioned limitations and gaps in the MWA area, this dissertation describes the development of MWA applicators with non-spherical ablation zones for site-specific applications. Antennas with a planar heating pattern were designed for ablation of the endometrial lining of the uterine cavity, with application to treatment of menstrual heavy bleeding. Antennas operating at 5.8 GHz, a higher frequency band

compared to the 915 MHz and 2.45 GHz typically investigated in other studies, were designed and evaluated for creation of small, spherical ablation patterns.

We also investigated the potential use of antenna reflection coefficient as a feedback signal for monitoring the evolution of the treatment zone. The dielectric properties of bovine liver tissue were measured and modeled at ablative temperatures across a wide range of frequencies. The final data will provide the foundation for further model-based design and development of next-generation minimally invasive MWA systems as well as wideband techniques for real-time monitoring of MWA. Finally, with the insight obtained from the tissue characterization experiments, the potential use of antenna reflection coefficient as a feedback signal for monitoring the ablation status during the course of ablation was investigated.

In this regard, this dissertation addressed the following research questions:

Question 1: Menorrhagia, a condition when menstrual periods have abnormally heavy or prolonged bleeding, significantly affects quality of life, and affects ~20% of women of reproductive age. Global endometrial ablation (GEA) is a minimally invasive alternative to surgical options such as hysterectomy. Is it feasible to design a MW antenna for GEA with near triangular shaped ablation pattern with ablation depth of 3–9 mm, conformal to the anatomy of diverse range of uterine cavities?

Question 2: In a GEA procedure, there is no imaging or non-imaging based mechanism for monitoring the ablation zone growth. A real-time feedback signal during

the ablation would provide the clinician with an extra source of information. What parameters of an ablation system could be used as a feedback signal to monitor the transient evolution of the ablation zone?

Question 3: Primary aldosteronism is characterized by the excessive secretion of aldosterone from the adrenal gland, and is responsible for up to 11.2% of all cases of hypertension. This excess of aldosterone is attributable to an adenoma (a benign adrenal gland tumor). The average adrenal adenoma is around 5–20 mm wide, which is much smaller than the majority of the malignant tumors in the liver, kidney, and lungs. One of the advantages of MWA is its ability to create large ablation zones when operating at frequencies of 915 MHz and 2.45 GHz. Is it feasible to create small ablation zones with MWA for destruction of adrenal adenomas? What is the effect of frequency on the ablation zone size and shape?

Question 4: There is a lack knowledge of tissue dielectric properties at ablative temperatures. In order to investigate ablation systems at different operating frequencies, and wideband approaches for monitoring treatment progress, characterization of tissue dielectric properties across a broad range of frequencies in the ablative temperature range is critical. What is the broadband temperature dependence of tissue dielectric properties?

1.4 Contributions

In order to address the aforementioned questions, this dissertation contributes to the state of the art of MWA as follows:

Contribution 1: In early years of MWA introduction, many efforts were focused on designing needle form MWA applicators with omnidirectional heating patterns [21]. We performed a comprehensive search on the MWA applicator designs, with a focus on applicators developed after 2006. These studies introduced applicators designs capable of creating directional and planar heating patterns, and ablation length control with integrated matching networks, chokes, and sleeves, as well as mechanisms for active cooling of applicators. This contribution is discussed in detail in chapter 2 and in the following review article:

[22] **H. Fallahi** and P. Prakash, "Antenna designs for microwave tissue ablation," *Crit. Rev. Biomed. Eng., vol. 46, no. 6, 2018.*

Contribution 2: Endometrial ablation is a minimally invasive treatment option for menorrhagia. Radiofrequency as the most commonly used endometrial ablation modality has two disadvantages: large applicator diameter and the need for direct contact of the applicator with the target tissue. The former requires dilation of the cervix that causes discomfort for the patient, and the latter requires integrating a suction mechanism into the applicator. As microwave applicators may not need direct contact with the target tissue, and thus allow for compact small-diameter applicators, we investigated the

feasibility of a microwave global endometrial ablation applicator. The specific anatomy of the uterine cavity led to design of a MWA applicator with a planar heating pattern, allowing ablation of the entire target with a single positioning of the applicator and capability of ablating a range of different uterine cavity sizes. Details of this study are discussed in chapter 3 and the following publications:

[23] **H. Fallahi**, J. Šebek, E. Frattura, J. Schenck, and P. Prakash, "Global microwave endometrial ablation for menorrhagia treatment," *in Proc. of SPIE Vol, 2017, vol. 10066, pp. 100660K–1.*

[24] **H. Fallahi** and P. Prakash, "Design of a Microwave Global Endometrial Ablation Device," *IEEE J. Electromagn. RF Microw. Med. Biol., 2019.*

[25] P. Faridi, **H. Fallahi**, and P. Prakash, "Evaluation of the effect of uterine fibroids on microwave endometrial ablation profiles," *in 2018 40th Annual International Conference of the IEEE Engineering in Medicine and Biology Society (EMBC), 2018, pp. 3236–3239.*

Contribution 3: Broadband reflection coefficient of the MWA loop antenna was measured and monitored during the course of ablation for the application of endometrial ablation. The shift of resonant frequency in the reflection coefficient and drop of transmission coefficient values were related to the ablation state of the target tissue. Details of this investigation are summarized in chapter 4 and the following patent application:

[26] P. Prakash, **H. Fallahi**, J. T. Schenck, E. A., Frattura, "Microwave global endometrial ablation systems and methods of use," WO2019241439A1, PCT/US20 19/036845 Filed: 06/12/2019.

Contribution 4: We investigated the effect of frequency of operation on the ablation size. A MWA antenna was fabricated to operate at 5.8 GHz and its performance was compared with an antenna operating at 2.45 GHz, one of the common operation frequencies of commercial MWA systems. The ability of the antennas to create small, spherical ablation zones ($<$ 10 mm) was assessed for the application of destroying benign adrenal adenomas. The antennas were experimentally evaluated in *ex vivo* and *in vivo* settings. Findings of this study are presented in chapter 5 and the following papers.

[27] **H. Fallahi**, A. Shahzad, D. Clausing, M. O'Halloran, M. C. Dennedy, and P. Prakash, "Technological requirements for microwave ablation of adrenal masses," in *Antennas and Propagation (EUCAP), 2017 11th European Conference on*, 2017, pp. 3713–3716.

[28] **H. Fallahi**, D. Clausing, A. Shahzad, M. O'Halloran, M. C. Dennedy, and P. Prakash, "Microwave antennas for thermal ablation of benign adrenal adenomas," *Biomed. Phys. Eng. Express, vol. 5, no. 2, p. 025044, 2019.*

[29] P. T. Donlon, **H. Fallahi**, W. L. Beard, A. Shahzad, L. Heflin, W. Cox, B. Bloomberg, J. D. Lillich, C. K. Ganta, G. J. O'Sullivan, G. Ruvio, P. M. O'Shea, M. O'Halloran, P. Prakash, M. C. Dennedy, "Using microwave thermal ablation to develop a

subtotal, cortical-sparing approach to the management of primary aldosteronism," *Int. J. Hyperthermia, vol. 36, no. 1, pp. 905–914, 2019.*

Contribution 5: *Ex vivo* bovine liver tissue is the most widely used tissue model for benchtop characterization of ablation technology. While it is well established that the dielectric properties of tissue change dynamically during the course of an ablation, the temperature dependency of liver tissue dielectric properties at ablative temperatures has not been reported at frequencies other than 2.45 GHz. Broadband temperature-dependent dielectric measurements were conducted on *ex vivo* bovine liver in the frequency range of 0.5 to 6 GHz. Different heating rates were tested and temperatures as high as 130 °C were recorded. The measured data were processed in order to parameterize the data to linear piecewise functions. The derived dielectric properties functions were incorporated within computational models of microwave ablation and applied to study transient changes in MWA antenna return loss during ablation. The contributions of this study are discussed in chapter 6 and the following papers:

[30] **H. Fallahi** and P. Prakash, "Measurement of Broadband Temperature-Dependent Dielectric Properties of Liver Tissue," in *2018 IEEE International Microwave Biomedical Conference (IMBioC)*, 2018, pp. 91–93.

[31] **H. Fallahi**, J. Šebek, and P. Prakash, "Broadband Dielectric Properties of *Ex Vivo* Bovine Liver Tissue Characterized at Ablative Temperatures," *IEEE Trans. Biomed. Eng.,* 2020.

1.5 Dissertation outline

This dissertation is organized as follows. A brief background of thermal ablation followed by an extensive review of MWA antenna designs is presented in chapter 2. Development of a MWA antenna for global endometrial ablation is illustrated in chapter 3. A technique for monitoring ablation zone growth in real-time for microwave endometrial ablation is discussed in chapter 4. Feasibility of using a 5.8 GHz antenna for creation of small size ablation zones is demonstrated in chapter 5. In chapter 6, Measurement results of broadband temperature-dependent dielectric properties are presented. Finally, concluding remarks and directions for future work are provided in chapter 7.

2 Background[1]

2.1 Thermal ablation

Thermal ablation is destruction of tissue by localized heating to elevated temperatures, typically in excess of 50 °C. Its medical applications includes tumor destruction in the liver, lung, kidney, and other organs, disrupting conduction pathways for treatment of cardiac arrhythmias, neuromodulation by destroying nerves (e.g. renal denervation), and tissue reshaping. Heating can be achieved through a variety of energy sources, including: microwave (MW), laser, radiofrequency (RF) current, and ultrasound (US) [32]–[36]. Ablative effects can also be obtained by freezing, termed cryoablation, and irreversible electroporation (IRE), which is a non-thermal ablative modality using high voltage pulsed electric fields [16], [37]. Technologies have been developed for delivering ablative energy via percutaneous, intracavitary, endovascular, endoscopic, laparoscopic, and open surgical approaches to a range of tissue targets. Suitable approaches for specific

[1] This chapter has been published as: H. Fallahi and P. Prakash, "Antenna designs for microwave tissue ablation," Crit. Rev. Biomed. Eng., vol. 46, no. 6, 2018. (DOI: 10.1615/CritRevBiomedEng.2018028554)

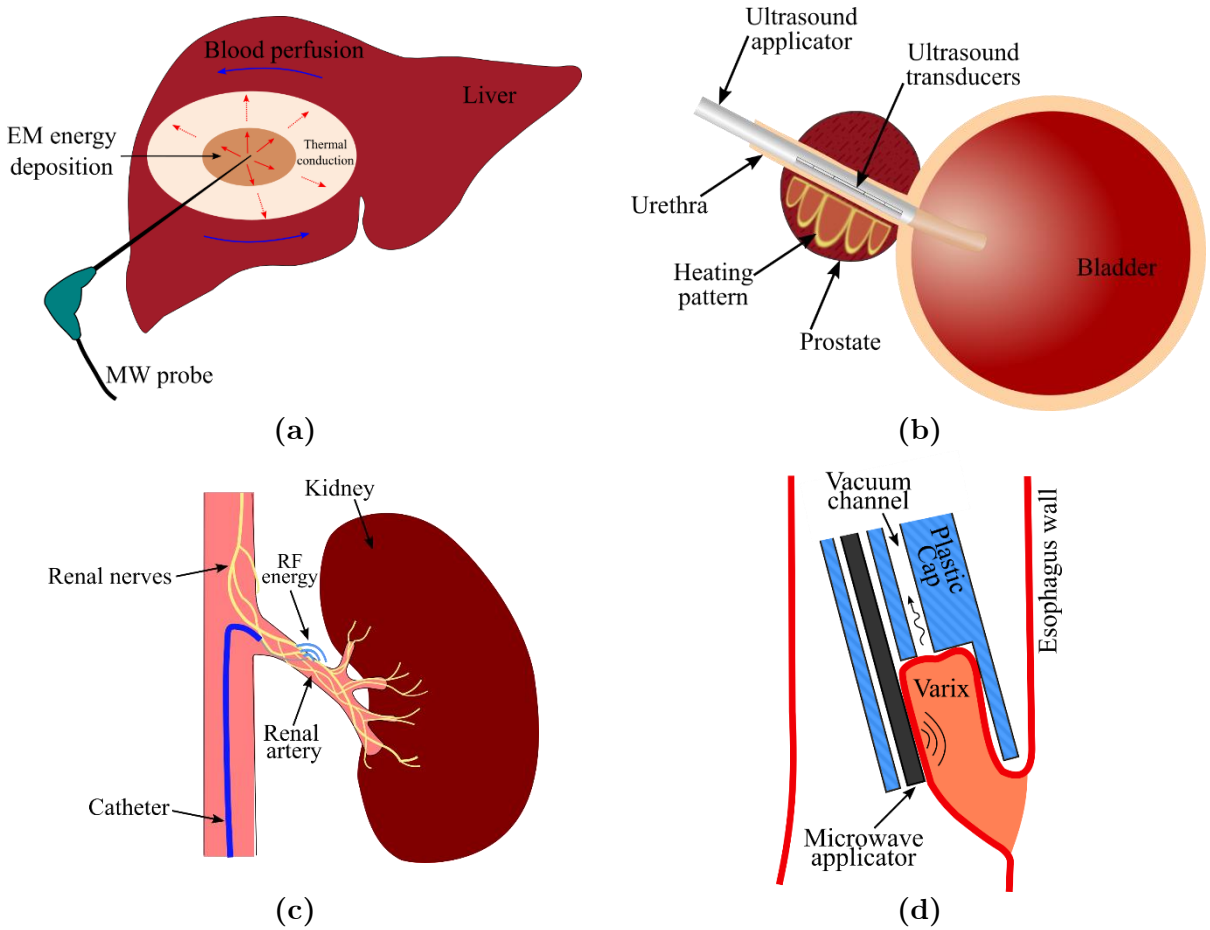

Figure 2-1: Examples of technologies for delivering ablative energy via a) percutaneous, b) intracavitary (adapted from Burtnyk *et al.* [38]), c) endovascular (adapted from Fernández-Ruiz [39]), and d) endoscopic approaches (adapted from Sebek *et al.*[40]).

target sites are determined by factors such as the size, location within the body, accessibility, and biophysical properties of the targeted tissue. Figure 2-1 illustrates schema for thermal ablation devices that have been developed, and are in clinical use, for use in the liver, urethra, renal artery, and esophageal tract.

Regardless of the energy modality, the biological effects of tissue heating are a function of the intensity of heating and the time for which the tissue is exposed to that temperature. In general, the higher the temperature, the shorter the amount of time tissue required to

be exposed to heating in order to deliver ablative treatment. A review of mathematical models of thermal damage following heating is provided in [41].

Of the various ablation technologies in clinical use, RF ablation devices have been most widely used, with major applications including treatment of cardiac arrhythmias and tumor ablation. The use of microwave energy for thermal tissue ablation was first reported in the late 1970s, where several studies described monopolar microwave antennas for surgical coagulation in soft tissues [42]. To date, the vast majority of development of microwave ablation technology has been focused on thermal ablation of large unresectable tumors in vascular organs such as the liver. In contrast to RF ablation, radiative MW ablation devices enable heating of larger tissue volumes. Researchers focused on optimizing needle-based microwave applicators such as dipole, monopole and coaxial slot antennas to provide large spherical ablation pattern. As reviewed in Bertram *et al.* and O'Rourke *et al.* [21], [43], efforts were focused on suppressing the backward current on the surface of the coaxial cable outer conductor by adding chokes and sleeves as well as keeping the electric fields concentrated around the antenna tip antenna [44], [45]. Another technique was to create a better coupling between the antenna and the surrounding tissue by loading the antenna with a dielectric material with electrical permittivity closer to that of the tissue [46]. While these modifications improved the ablation pattern, there was still room to make the applicators thinner and less invasive. Thinner applicators were introduced by integrating a matching network into the coaxial cable, using an air-filled coax section to

at the end of a Teflon-filled coaxial line, and integrating a balun on the coaxial cable outer conductor itself [47]–[49]. Medical applications other than hepatic cancer has led to some newer designs that offer directional heating pattern, making it possible to ablate diseased tissues safely next to critical structures [50], [51]. While the goal in design of coaxial-feedline-based antennas has been treatment of tumors, helix and spiral antennas have been primarily developed for intracavitary applications such as cardiac ablation and Barrett's esophagus [7], [8]. Microwave energy is usually delivered to the tissue through a coupling solution or gel kept around the antenna inside a balloon. Small and localized ablation patterns have been achieved by using transmission line based applicators for collagen reshaping on the cornea, endometrial ablation, and bone drilling [9], [52], [53]. Coaxial cable and circular waveguides can create a hotspot at their tip. One of the main requirements in minimally invasive ablation is the small diameter of the device. This has limited the design to coaxial applicators. However, applicability of printed circuit board technology in microwave ablation has been investigated by choosing a higher operation frequency aiming for small ablation zone and designing dual-mode devices for dielectric measurement and ablation [54], [55].

The antenna is an integral element of a MW ablation device and has a significant impact on the ablation pattern. This chapter reviews antenna designs that have been developed to address clinical needs for a diverse set of applications.

2.2 Overview of microwave ablation

2.2.1 Biophysics of microwave tissue heating

Propagation of electromagnetic energy is determined by the dielectric permittivity and magnetic permeability of the media within which the waves are induced and travel. Like many other materials, the relative magnetic permeability of most biological tissues is approximately equal to one. However, the dielectric permittivity varies widely amongst tissue types, and is generally complex valued. The complex permittivity of tissue, ϵ_r^*, is often expressed in terms of relative permittivity, ϵ_r', and effective electrical conductivity, σ, which are defined as in Eq. (1):

$$\epsilon_r^* = \epsilon_r' - j\epsilon_r'' = \epsilon_r' - j\frac{\sigma}{\omega\epsilon_0}, \qquad (1)$$

where ω [rad/s] is the angular frequency and ϵ_0 is vacuum permittivity. The Poynting theorem, Eq. (2), describes the conservation of electromagnetic energy:

$$\nabla \cdot \mathbf{P} = -\frac{\partial}{\partial t}\left(\frac{1}{2}\epsilon_0\epsilon_r^*\mathbf{E}\cdot\mathbf{E}\right) - \frac{\partial}{\partial t}\left(\frac{1}{2}\mu_0\mu_r^*\mathbf{H}\cdot\mathbf{H}\right), \qquad (2)$$

where $\mathbf{P}$ is the Poynting vector, and $\mathbf{E}$ and $\mathbf{H}$ are electric and magnetic fields, respectively. Poynting vector represents the directional energy flux of an electromagnetic field and is given by $\mathbf{P} = \mathbf{E} \times \mathbf{H}$. The real component of $\nabla \cdot \mathbf{P}$ in Eq. (2) quantifies the ability of a material to support electrical and magnetic energy whereas the imaginary component of $\nabla \cdot \mathbf{P}$ determines how well electromagnetic energy is absorbed by a material. It is noted that effective conductivity (computed from imaginary part of ϵ_r^* in Eq. (1)) captures the

contribution from time-varying electric fields (displacement current), specifically rotation of dipoles in polar materials as they constantly realign themselves with an alternating electric field. In most biological tissues, the main contribution to losses at microwave frequencies is the displacement current. The rotation of dipoles generates heat inside biological tissues which is known as dielectric heating [56], [57].

Both relative permittivity and effective conductivity are dependent on frequency, temperature, and other factors in biological tissues such as water content. As an example, Figure 2-2 shows the relative permittivity and effective conductivity of liver tissue as function of frequency in the range of 10 Hz to 100 GHz.

The electromagnetic wavelength in tissue can be calculated from the relative permittivity using the relationship ($\lambda = \frac{c_0}{f\sqrt{\epsilon_r}}$, c_0 is light velocity in free space). The wavelength is a particularly important parameter for antenna design; antennas are often efficient when their critical dimension is of the order of wavelength. The relatively long wavelength (on the order of centimeters) in biological tissue places constraints on the minimum antenna size that can be employed for practical ablation applications. Electromagnetic wavelength in liver tissue as a function of frequency is shown in Figure 2-3.

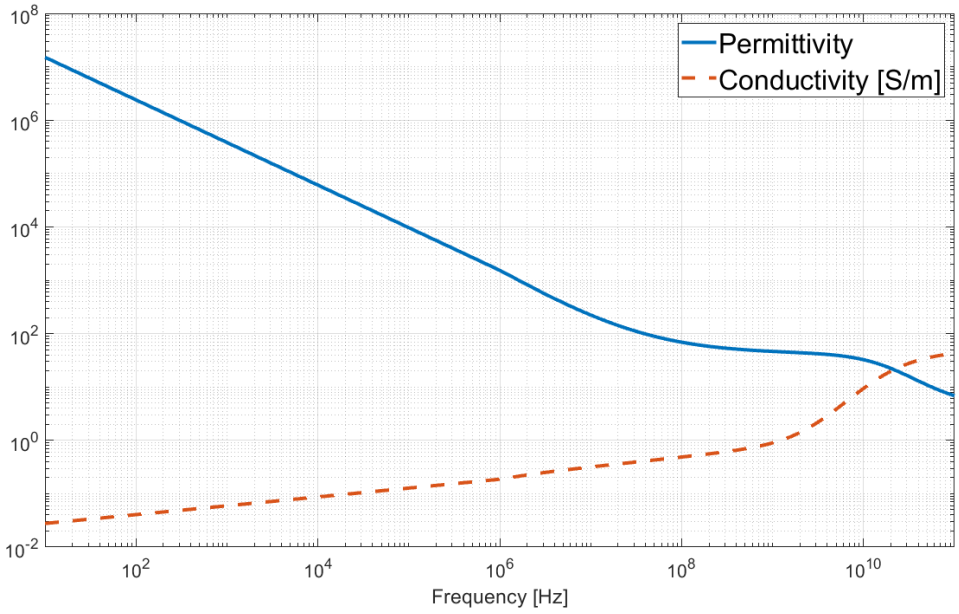

Figure 2-2: Dependence of liver dielectric properties on frequency based on technology described by Gabriel *et al.* [58].

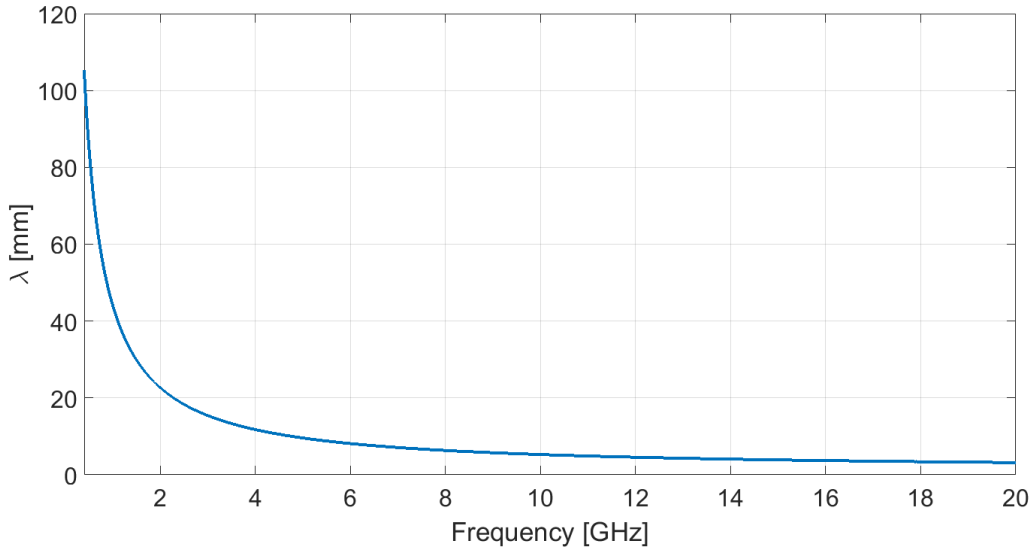

Figure 2-3: Electromagnetic wavelength in liver tissue vs. frequency.

2.2.2 Microwave ablation systems

A block diagram of an image-guided microwave ablation system is shown in Figure 2-4. In this system, power is transferred from a high power microwave source to the target

tissue through an applicator. An imaging system assists the physician in locating the targeted tissue, and positioning the applicator accordingly. The imaging system, as well as auxiliary sensors (potentially integrated within the applicator), may provide some assessment of the treatment progress, which the physician may use to adjust the treatment parameters. For example, in the case of percutaneous tumor ablation, changes in Hounsfield unit observed on CT imaging may provide some assessment of the region where ablative energy is deposited. Other physical variables that may provide some assessment of treatment progress include antenna impedance mismatch (as assessed by changes in reflected power), temperature, and pressure. Selection of the treatment delivery parameters (e.g. applicator positioning, applied power level, and treatment duration) for individual treatments are most often selected based on the physician's experience. Model-based treatment planning tools guiding ablation procedures are the subject of active research [59].

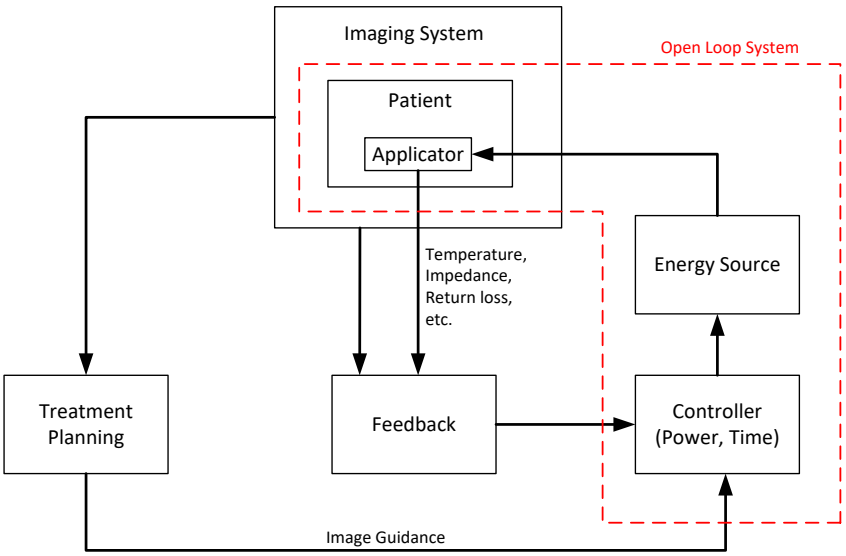

Figure 2-4: Components of an image-guided microwave ablation system.

Most microwave ablation systems in clinical use operate at 915 MHz and 2.45 GHz. The rationale for selection of these frequencies is that they fall within industrial, scientific, and medical (ISM) band, as well as they exhibit larger penetration depth and less cable heating, which increases with frequency. However, there are some merits to go to higher frequencies as explored at 9.2 GHz, 10 GHz, 14.5 GHz, 900 MHz-18 GHz, and 24 GHz [9], [60]–[62], [55], [63], [64]. In Yoon *et al.* [55] and Sawicki *et al.* [63], the effect of microwave frequency on ablation zones was assessed using dipole and planar antennas. These studies suggested thermal conduction has a more significant role in creation of the ablation zone at higher frequencies compared to low frequencies, where microwave power absorption is dominant. Furthermore, the ablation zone dimensions remain comparable in size over frequency for constant input power and ablation duration although the active length of the device becomes smaller as frequency increases. A smaller antenna could allow more flexible routing near organ boundaries or around major blood vessels. However, a drawback of using high frequencies is larger ohmic heating along the feedline due to the smaller skin depth, which can lead to a teardrop ablation zone at high power levels.

Different components of the ablation system have been under investigation in order to achieve an effective treatment. Much effort has been focused on designing applicators capable of creating large spherical ablation patterns in highly vascular organs such as the liver or ablation patterns conformal to the organ under treatment. Some researchers have characterized thermal and electrical properties of different tissues and investigated

biological effect of different energy modalities in order to improve the simulation models for device design. This would reduce the cost and number of iterations in the device design process. Incorporation of an imaging system capable of real-time monitoring of the ablation progress would be a significant step towards enabling delivery of adequate thermal doses to targeted tissues. Finding a parameter to estimate the growth of the ablation zone instead of an imaging system is another option to be employed as a feedback. One example of a feedback parameter is tissue impedance change relative to its desiccation rate, as commonly employed in RF ablation systems. Novasure is an impedance controlled global endometrial ablation system that monitors the tissue impedance to control the ablation depth [65]. All the feedback parameters would be used to adjust the power and time of the energy source.

2.3 Microwave ablation applicators

The goal of thermal ablation procedures is to heat targeted tissue regions to ablative temperatures, while minimizing damage to non-targeted tissue regions. Applicators for microwave ablation consist of a feeding transmission line terminated by a radiating antenna; the electric field radiated by the antenna is absorbed in surrounding tissue regions leading to heating.

Since practical transmission lines are made of conductors and dielectrics with non-negligible attenuation, the transmission line heats up when microwave power supplied

from the generator passes through. The geometry of the radiating antenna, frequency of operation, and the electromagnetic properties of the surrounding media, determine the spatial profile of the radiated electric field into tissue, as well as the applicator's efficiency at transferring power from the feeding transmission line to the radiating antenna.

Antenna return loss (RL) represents the ratio of power delivered to the antenna to the power reflected back to the source due to impedance mismatch between the transmission line and antenna:

$$RL_{dB} = 10 \log_{10} \frac{P_i}{P_r} \qquad (3)$$

While it is desirable to maximize RL, in practice $RL > 10\ dB$ provides an approximate design goal, representing 90% power transferred to the antenna. Inefficient applicators will require larger applied power levels at the transmission line input terminal to achieve the same ablation size, as an efficient applicator. Attenuation within the feeding transmission line leads to heating of the applicator, which often requires the use of active cooling strategies to maintain applicator integrity and minimize passive heating of tissue that may be in contact with the applicator. Thus, highly efficient applicators are desirable as they reduce the burden on cooling of the feeding transmission line.

A typical cooling system integrated to the applicator consists of circulating coolant fluid through two inflow and outflow lumens. The fluid could be a saline solution or pressurized CO2 gas [66],[67]. Advantages of cooling are sparing the healthy tissue along the feedline, increasing the sphericity of ablation zone by mitigating the backward heating

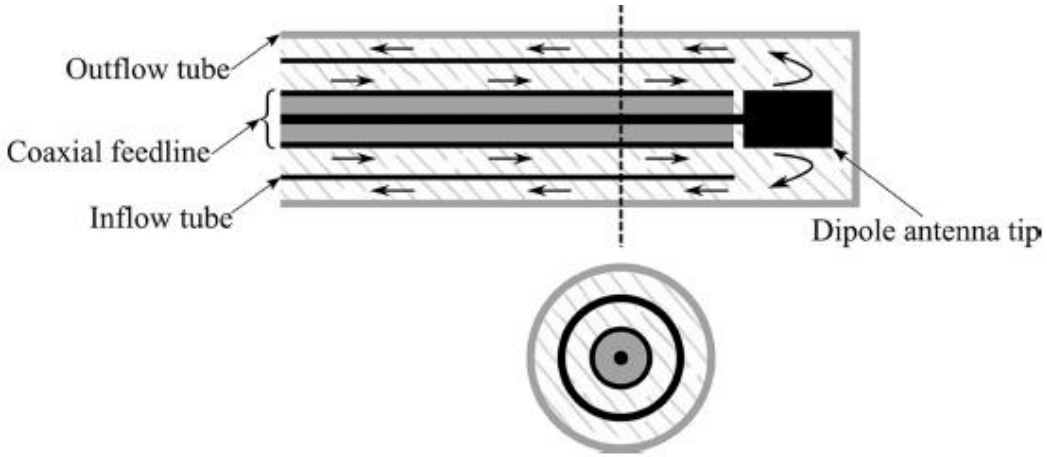

Figure 2-5: Integration of a cooling system to a coaxial dipole antenna.

and higher power delivery. Figure 2-5 shows a cooling strategy on a dipole antenna. Cooling may be implemented using an arrangement of concentric tubes for coolant inflow/outflow. If the coolant used is electromagnetically lossy, circulating the coolant to the distal tip of the radiating antenna will result in microwave absorption within the fluid, coupling less power to the tissue, and potentially reducing the efficacy of the cooling.

The antenna geometry, relative to the electromagnetic wavelength at the operating frequency, also determines the pattern of the radiated electric fields. It is desirable to select antenna geometries that yield electric field radiation patterns that are well matched to the tissue regions targeted for ablation. While the electromagnetic power absorbed is proportional to $|\mathbf{E}|^2$, thermal profiles in tissue are also affected by passive conduction of heat and cooling due to blood flow, and these effects should be considered during antenna design optimization [68].

The efficiency and ablation pattern of candidate microwave applicator designs can be evaluated under a variety of experimental conditions. Antenna RL can be measured

by immersing the antenna in a tissue mimicking load. A variety of tissue-mimicking phantoms with tunable dielectric properties have been reported in the literature [69], [70]. Measurement of the antenna's SAR pattern may be helpful for assessing the radiation pattern of an antenna, but neglects the effects of thermal conduction on ablation zone profiles [71]. Furthermore, SAR measurements typically do not account for the changes in antenna radiation pattern due to temperature dependent changes in tissue dielectric properties. Ablation devices are often characterized on the benchtop in *ex vivo* tissue. The size and shape of the ablation is defined by tissue discoloration at elevated temperatures [72]. To account for effects of blood perfusion, which acts as a heat sink, ablation zones must be evaluated in an *in vivo* animal model or by emulating the perfusion using a perfusion chamber [73], [74]. Ablated tissue is resected after *in vivo* ablations for histopathologic analysis; viability stains may assist in accurate determination of the ablation zone boundary.

2.3.1 Early microwave ablation applicators

Semi-rigid coaxial cables have been widely used as feeding transmission lines within microwave ablation applicators. This is because their cylindrical geometry facilitates insertion within rigid catheters, and antennas can be readily integrated by modifying the geometry of the distal tip of the cable. Ablation applicators are designed to fit within an insulating material (e.g. a rigid catheter) to facilitate insertion, prevent the device from adhering to the ablated tissue, provide protection and mechanical stability, and improve

Figure 2-6: Original antennas: dipole, monopole, and slot (black metal, grey: dielectric).

power coupling to the tissue. Figure 2-6 illustrates insulated coaxial dipole, monopole and slot antennas that have been extensively characterized for moderate hyperthermia and thermal ablation [75]–[77].

Generic dipole antennas consist of two equal length conductors separated by a small gap, where the feeding transmission line is connected. As illustrated in Figure 6, the coaxial dipole antenna incorporates a $\lambda_{effective}/4$ length of conductor separated from the cable, where $\lambda_{effective}$ represents the effective wavelength for a concentric multi-layered structure of an insulated conductor, surrounded by electromagnetically lossy tissue [78]. The effective wavelength is a function of the coaxial cable diameter, thickness of the insulating catheter, and dielectric properties of the surrounding tissue and the catheter. For instance, the $\lambda_{effective}/4$ length for liver tumor ablation could be around 10.9 mm at 2.45 GHz for a dipole made of UT-85 coaxial cable (0.085" O.D.), inserted within a thin polyolefin heat-shrink tubing ($\epsilon_r \sim 2.1$). The length of the gap is usually designed to be much smaller than the wavelength in order to approximate it as an infinitesimal source. The gap acts as an effective source for propagation of electromagnetic waves. The second

leg of the dipole is formed by the section of the coaxial cable proximal to the gap. The differences in the length of these two legs leads to an unbalanced dipole antenna. The difference in construction of the dipole and slot is that in the dipole, the distal end is a solid metallic cylinder while in the slot, it is a coaxial cable shorted at the end. The monopole antenna is formed by stripping a $\lambda_{\text{effective}}/4$ section of the coaxial cable's outer conductor.

Major shortcomings of these antennas are the dependence of the ablation profile and resonant frequency on the insertion depth of the device, backward heating, and non-spherical ablation profile. Current travels toward the antenna inside the coaxial cable on the inner conductor surface and inside surface of the outer conductor. A part of the current would travel back toward the microwave source on the outer surface of the outer conductor due to unbalanced structure of coaxial cable. This current generates unwanted heat along the feed cable and decreases the sphericity of the ablation pattern. One effective solution to these limitations is the addition of a choke or sleeve to the outer conductor of the cable to suppress the backward currents and keep the power deposition localized to the radiating part of the antenna [44], [45]. Another solution to improve the ablation pattern sphericity are addition of a cap and dielectric loading of the antenna radiating section with materials such as Teflon, Alumina or ceramic [46],[79]–[81].

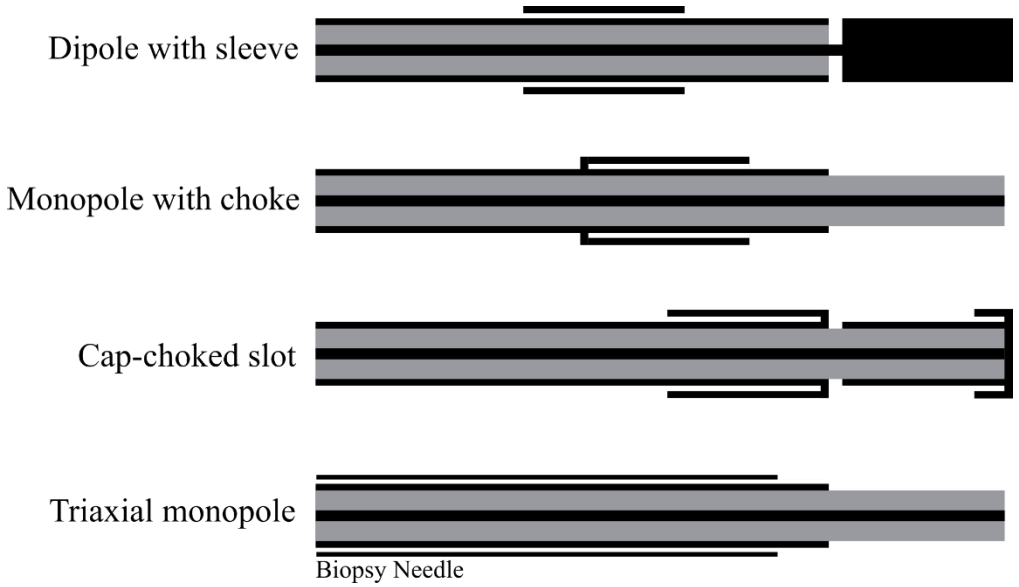

Figure 2-7: Examples of coaxial antennas with sleeve, choke, and cap and a monopole in a triaixal configuration (black metal, grey: dielectric).

Figure 2-7 shows incorporation of chokes, a sleeve, and a cap in the original antennas. The difference between a choke and a sleeve is the electrical connection of the choke with the coaxial cable outer conductor. A dielectric such as Teflon is usually used to hold the sleeve in place and prevent electrical connection to the outer conductor. Length of a choke is usually $\lambda_{effective}/4$ while that of sleeve is approximately $\lambda_{effective}/2$ [45]. It could be placed at a short distance from the gap based on the antenna type. Optimization technique for sleeve designs are presented in Prakash *et al.* [68], [82]. The principle of operation of a choke is similar to a balun in a coaxial dipole antenna. It has been also observed that addition of a choke also aids in impedance matching [80], [83]. One technique to localize the radiation of the antenna to the distal end of the applicator is to add a cap to tip of the antenna. The cap increases capacitance and may be implemented using a variety of shapes such as disk, ring and arrow. Figure 2-7 also illustrates a design

which employs a biopsy needle as both an introducer and a choke to obtain a thinner device [73], [83], [84].

Another antenna design to improve the radiation localization with the goal of achieving a more spherical ablation pattern even without a choke is a multi-slot coaxial antenna [85]–[87]. The multi-slot antenna is similar to the single slot antenna shown in Figure 2-6, except with more slots scattered along the coaxial cable. In a dual-slot antenna, an active choke is created by destructive interference of the phase of currents from the proximal and distal slots along the antenna shaft that suppresses the backward current and truncates the heating pattern [87], [88].

As an example, the steps for fabricating a dipole antenna with a sleeve are illustrated in Figure 2-8. The simulated and measured return loss of two dipole antennas, one with and another without the sleeve, are compared in Figure 2-9. Both antennas exhibit a very wide bandwidth. Simulated SAR and temperature profiles of the dipoles

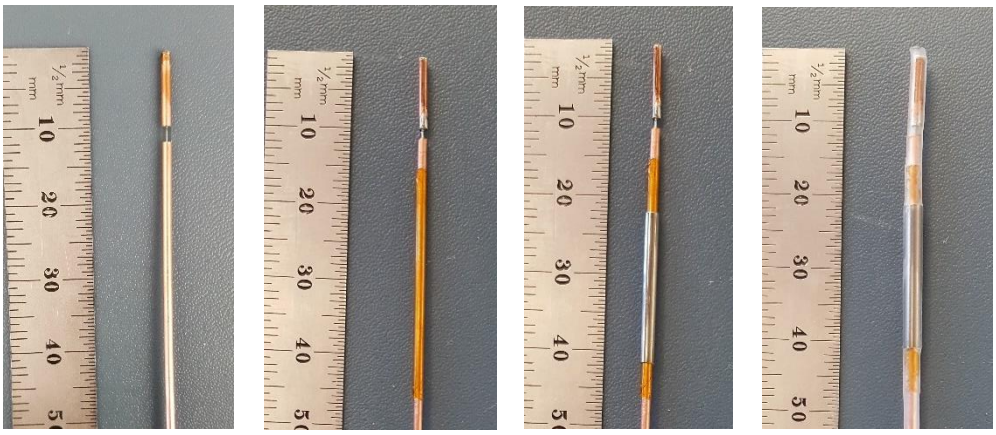

(a) (b) (c) (d)

Figure 2-8: Fabrication steps of a dipole antenna with sleeve: a) simple dipole, b) addition of an insulation layer (polyimide), c) addition of the metal sleeve, and d) covering of the dipole with heat shrink.

are shown in Figure 2-10. Photos of experimental ablation patterns of the two dipole antennas in *ex vivo* muscle tissue are also shown in Figure 2-11.

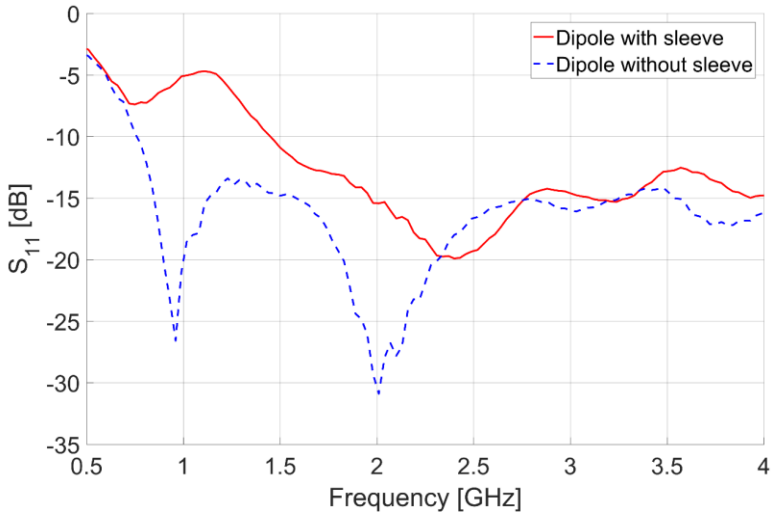

Figure 2-9: Measured reflection coefficient (S_{11}) of dipoles antennas with and without sleeve.

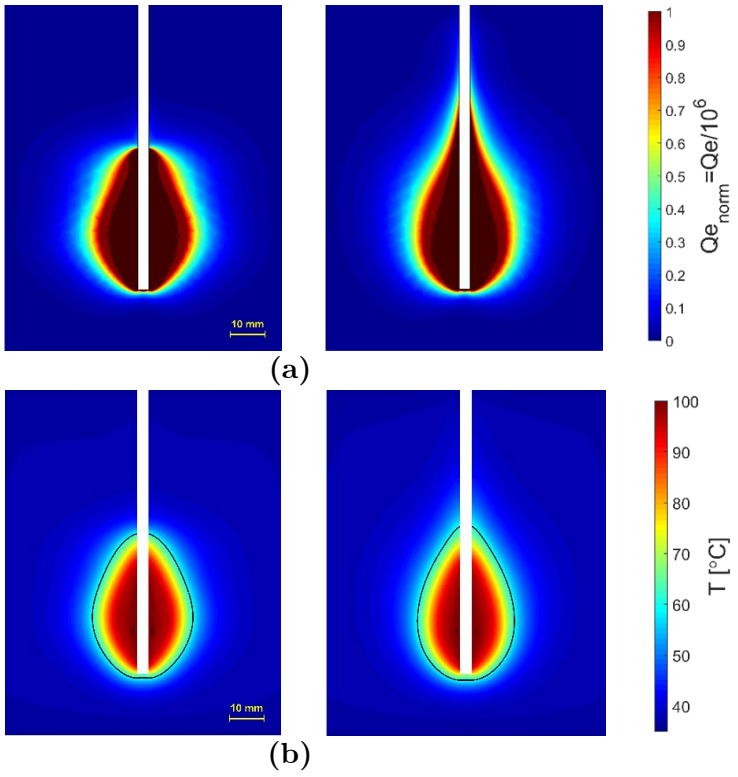

Figure 2-10: Simulated a) power absorption profile and b) temperature profiles of dipole antennas with (left) and without (right) sleeve. Estimated extent of the ablation zone is overlaid in black (Pin = 60 W, duration = 2 minutes).

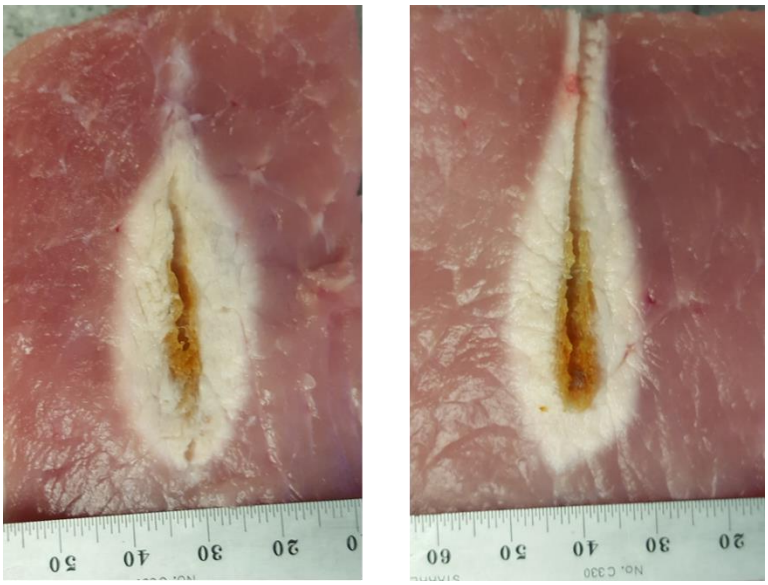

(a) (b)

Figure 2-11: Example ablation patterns of dipole antennas a) with and b) without sleeve in *ex vivo* porcine muscle (Pin = 60 W, duration = 2 minutes).

2.3.2 Reduced diameter microwave ablation antennas

Although integration of chokes and caps improves the antenna performance by achieving highly localized SAR patterns, these elements make the applicator more invasive by increasing the overall diameter. Recent efforts have been focused on integrating the choke or sleeve within the coaxial cable. Figure 2-12 shows three different designs for suppressing the backward current. Figure 2-12(a) shows a balun-free design [47]. The principle of this approach is to operate the antenna at the second resonant frequency where electrical length of the helical antenna is half a wavelength. The SAR pattern is then highly localized to the applicator tip as a result of a current minimum at the feed point of the helix. This current minimum provides a high feed impedance that acts as a natural choke and suppresses currents excited on the outer surface of the outer conductor. However, the input impedance creates a large mismatch between the coaxial feedline and

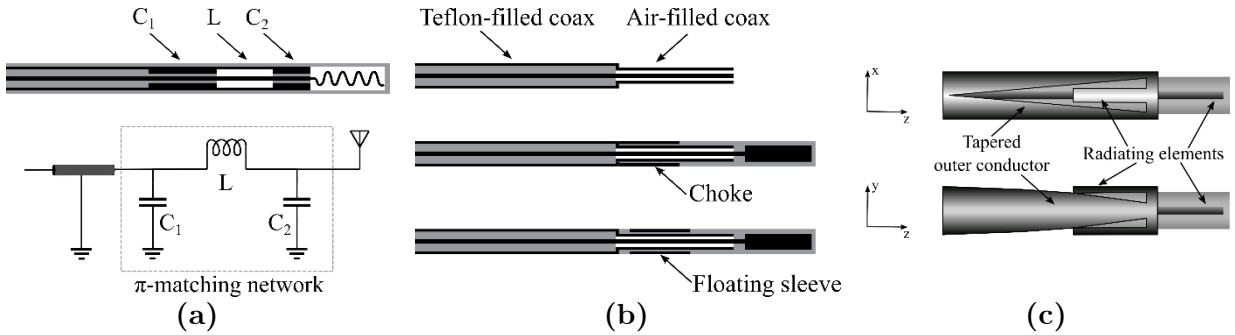

Figure 2-12: Techniques for reducing applicator diameter: a) Matching network [adapted from Luyen *et al.* [47]], b) reduced diameter by using a different dielectric material [adapted from Luyen *et al.* [48]], c) tapered balun [adapted from Luyen *et al.* [49]] (black metal, grey: dielectric, white: air).

antenna. This problem is resolved by integrating a quarter-wavelength transformer or π-matching network. These matching networks can be designed and implemented by choosing different dielectric materials such as air for the coaxial cable as well as altering the thickness and diameter of the inner and outer conductor.

Figure 2-12(b) shows a technique for incorporating a choke or sleeve within the antenna without increasing its diameter [48]. The technique utilizes an air-filled coax section at the end of the common Teflon-filled coaxial feedline with the goal of achieving a smaller diameter. Using air and Teflon permittivity to calculate the dimensions of a coaxial cable with 50 Ω characteristic impedance, a 30% smaller diameter is obtained for the same inner conductor diameter. A choke or sleeve can be implemented on the air-filled section of the coax to avoid increase in overall diameter of the applicator.

The main reason to use a choke or sleeve on a percutaneous microwave ablation antenna is to suppress the backward currents on the outer surface of the outer conductor of the coaxial feedline. Backward currents exist due to the inherent unbalanced structure

of the coax cable. By gradually changing the shape of the outer conductor to create a balanced transmission line, the backward current problem may be addressed. Figure 2-12(c) shows a dipole antenna design with a tapered balun [49]. The outer conductor has been gradually tapered into two parallel strips that act as the second arm of the dipole. The first arm of the dipole is the extension of the inner conductor. Besides achieving a highly localized SAR without using an external choke or sleeve, the tapered balun improves the antenna return loss by acting as a matching network. Further, the gradual taper of the balun increases the antenna bandwidth.

2.3.3 Directional applicators

Most microwave ablation applicators employ a needle-based design and yield ovoid ablation pattern. In practice, the applicator is usually placed in the center of the targeted tissue and the ablation zone progresses radially outward. In cases when the target is next to critical structures, caution must be taken to prevent any damage to non-targeted tissues. One technique to overcome this adverse effect is fluid instillation between the target and adjacent tissue (hydrodisplacement) to protect vulnerable organs. The fluid such as dextrose 5% in water (D5W) or saline increases the distance between the microwave source and the target structure, and further acts as a heat sink. In other words, this technique directs the energy only to sites where no fluid is surrounding them [89].

Recently, a few antenna designs restricting microwave radiation in a preferred direction, approximately one half of the angular expanse, have been reported. Such

applicators may be used for ablation of targets in proximity of critical structures, without requiring any space for fluid displacement. Figure 2-13 shows two antenna designs with directional radiation patterns suitable for integration within rigid catheters/needles. A proof of concept device is shown in Figure 2-13(a) [50]. This design consists of a monopole antenna with water-cooling incorporated through its shaft. The coaxial feedline is concentrically placed within two inner (water inflow) and outer (water outflow) tubes. The inner tube, made of metal, is cut into a semicylinder from the base of the monopole and extended beyond the tip of the monopole. This semicylinder would act as a reflector in order the direct the microwaves to one side of the monopole antenna. The outer tube, made of dielectric (polyimide or PEEK), extends beyond the reflector and allows water to circulate back to the reservoir. The circulating water provides active cooling which mitigates heating along the feedline. It makes the device less invasive by eliminating the need for choke or sleeve for backward heating. Additionally, water high electrical permittivity (ϵ_r = 78 @ 2.45 GHz) reduces the wavelength, thereby limiting overall antenna radiating length.

A thinner (2.5 mm diameter) with deeper radial ablation depth was obtained by modifying the monopole shape and reflector of Figure 2-13(a) in Sebek *et al.* [90]. The monopole antenna of Sebek *et al.* [90] is pushed toward the outer tube wall. The placement of the monopole antenna in close proximity to the outer tube wall and closer to the tissue would allow a larger portion of near field microwave energy to be coupled to the tissue

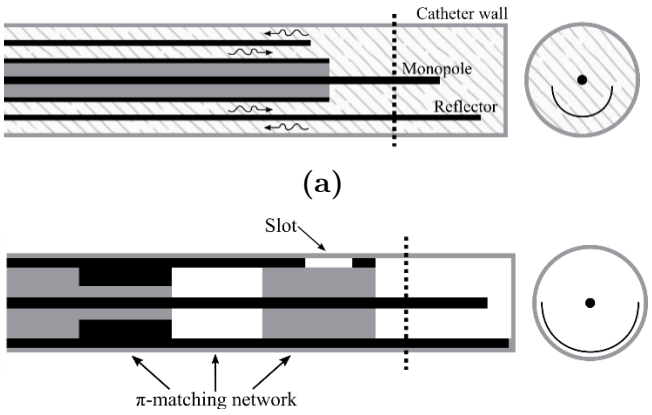

Figure 2-13: a) Proof of concept [adapted from McWilliams *et al.* [50]], and b) slot/monopole [adapted from Mohtashami *et al.* [51]] directional antennas (black metal, grey: dielectric, white: air, patterned: water).

and reduce the loss of energy to the cooling water. However, this placement increases the heating in the tissue behind the reflector. Shifting the reflector away from the monopole and toward the wall of the outer tube or using a parabolic shape reflector would help in increasing the radiation in the forward direction as well as providing a better shield in the reverse direction.

Figure 2-13(b) shows an applicator that provides a directional heating pattern by incorporating a reflector and a slot into a monopole antenna [51]. To limit the diameter of the device, the reflector is made by extending a portion of the coaxial cable's outer conductor. The slot is also etched out next to the base of the monopole. The reflector is the main component in reducing the radiation behind the reflector. However, addition of the slot would create constructive and destructive electric fields in front and behind the reflector, respectively. The slot improves the directionality of the applicator and suppresses the backward currents by creating a significant mismatch between the antenna

and coaxial feedline. Although use of a slot leads to a thinner applicator (2.9 mm diameter) by eliminating the need for a balun, but it creates a mismatch at the operation frequency that could be addressed by integrating a matching network into the coaxial cable. A π-matching network is implemented in the coaxial cable by using a different dielectric material inside the cable and changing the thickness of the outer conductor.

Sebek *et al.* [40] integrated a modified version of the directional device of McWilliams *et al.* [50] shown in Figure 2-13(a) into a standard endoscopic cap for the application of treating esophageal varices. The study investigates feasibility of using microwave ablation for treating esophageal varices with the goal of achieving a safer and more effective treatment compared to Endoscopic Variceal Ligation (EVL). A suction mechanism similar to variceal ligation captures the vessel by creation of a vacuum. When the vessel is sucked into the cap, the microwave antenna located in the wall of the cap delivers microwave energy to coagulate blood and seal the vessel. The antenna consists of a water-cooled monopole with a reflecting element. The monopole has been angled to improve the energy deposition to the vessel while sparing the surface. The distal end of the reflector has been formed into a hood to guide the water flow toward the backward flow channel. This would reduce the likelihood of air bubble formation that may come out of solution as the water trapped at the distal tip is heated.

Photo of a fabricated directional device is shown in Figure 2-14. Simulated normalized power absorption profiles for a conventional monopole antenna compared to

a directional antenna are shown in Figure 2-15. Experimental ablation patterns for both antennas are shown in Figure 2-16. These images illustrate the ability of the directional antennas to restrict ablation to approximately one half of the angular expanse.

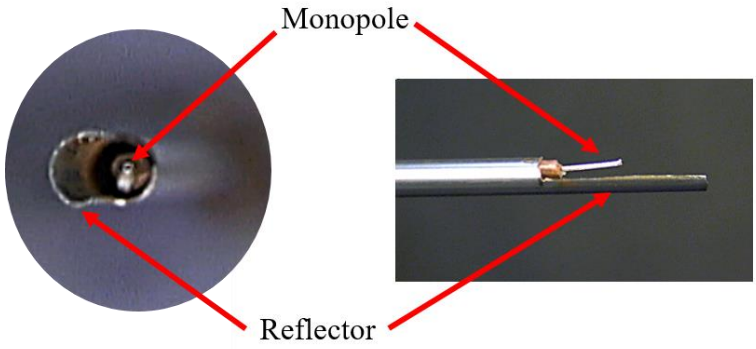

Figure 2-14: Example of a fabricated directional monopole antenna without the outflow polyimide tube [courtesy of Pegah Faridi].

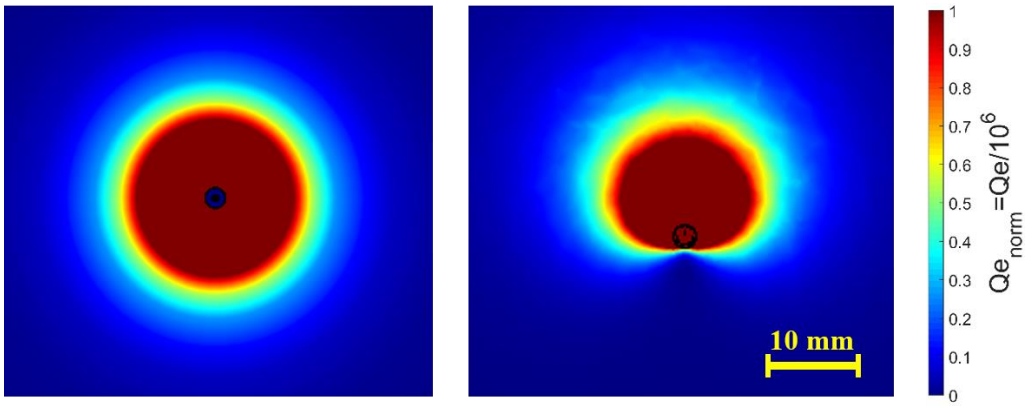

(a) **(b)**

Figure 2-15: Example power absorption profiles of a) a conventional and b) a directional antennas.

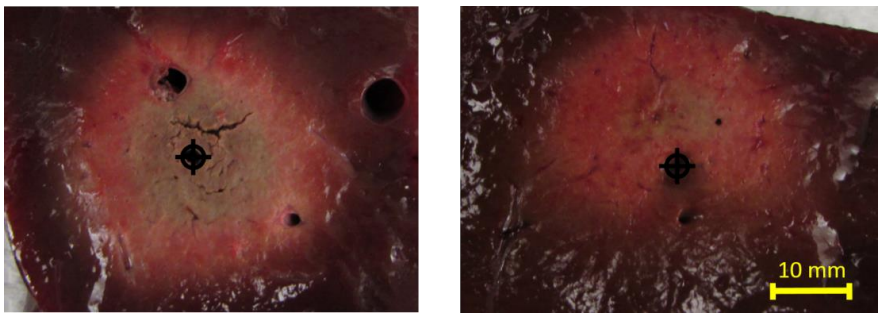

Conventional antenna **Directional antenna**

Figure 2-16: Comparison of directional and conventional monopole antenna ablation patterns in the liver tissue.

2.3.4 Helix and spiral antennas

The helical antenna is a basic antenna made of a wire wound in the form of a helix. The helix is usually connected to the inner conductor of a coaxial transmission line with the coaxial cable outer conductor as the ground. Helical antennas can be operated in axial and normal modes. When the helix diameter and spacing of the turns are comparable to the wavelength of the operation frequency, its maximum radiation intensity is along the axis of the helix. This end-fire radiation pattern could be obtained by adjusting the circumference of the each turn to the order of one wavelength and spacing between turns to approximately quarter of a wavelength. In the normal mode, the maximum radiation of the antenna is in the plane normal to the helix and minimum along its axis. This mode is achieved when diameter and spacing between turns are small compared to the wavelength [91].

Helical antenna for thermal therapy applications were originally designed and experimentally evaluated for hyperthermia applications. Figure 2-17 shows three variations of helical antennas investigated in [92]. The antennas were constructed by stripping off part of the outer conductor from one end of the coaxial cable. Coils made of

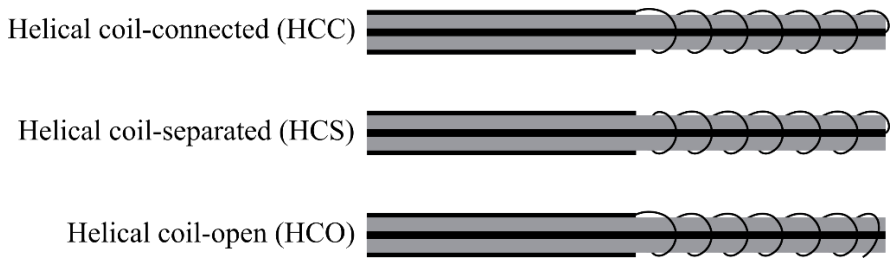

Figure 2-17: variations of helical antenna [adapted from Satoh *et al.* [92]] (black metal, grey: dielectric).

copper wire were installed on the dielectric of the coaxial cable. In the helical coil-connected (HCC) variation, the distal end of the coil is electrically connected to the coaxial cable inner conductor while its proximal end is shorted to the outer conductor. In the helical coil-separated (HCS) variation, only the distal end is connected to the coaxial cable inner conductor. In the helical coil-open (HCO) variation, only the proximal end is shorted. HCC configuration has been analytically characterized in Mirotznik *et al.* [93] and investigated in Reeves *et al.* [8] for treatment of Barrett's esophagus while Liu *et al.* [94] has investigated HCO configuration at 433 and 915 MHz. HCS has also been implemented for ablation of atrioventricular junction by Langberg *et al.* [95] Number of the turns, length of the radiating part and connection configuration of the coil are factors that can be optimized to obtain a desirable heating pattern [92]. Overall, advantages of the helical antenna over a simple dipole antenna are stable heating pattern regardless of the insertion depth, and uniform heating pattern along the helix axis with limited radial penetration.

In [7], a spiral antenna is proposed for cardiac ablation. The advantage of a spiral antenna is its radiation pattern maximum normal to its surface. The spiral antenna can be modeled as a large circular loop. The excited fields by currents on the loop add up constructively inside the loop and cancel out each other outside the loop. Thus, radiation pattern of the spiral antenna, similar to that of the loop, makes it a good candidate for creating a planar heating profile when placed on the tissue surface. The resonant frequency

of the spiral is dependent of the length of the antenna, and thickness and material of its dielectric coating. In another implementation the spiral antenna is deployed inside a balloon inflated with low loss low dielectric constant fluid such as air or nitrogen [96]. The fluid not only prevents heating of the blood within the heart chamber, it also deliver more power to the heart tissue when less fluid is in front of the spiral than behind it.

2.3.5 Transmission line based devices

For applications beyond oncology, it may be desirable to create small, localized ablation patterns. This may be achieved by employing open-ended transmission lines such as coaxial cables and waveguides. Fundamentally, an antenna plays the role of a matching network for coupling energy from a transmission line to a medium. Antennas are designed to provide desirable radiation pattern for the corresponding application. Nonetheless, open-ended transmission lines are capable of radiation without an antenna. Swicord *et al.* [97] have calculated the energy deposition pattern at the tip of an open-ended coaxial probe and shown that the total power is absorbed within a hemispherical region around the tip. This energy deposition pattern has been applied to cornea reshaping for correcting hyperopia, keratoconus, or myopia in Trembly *et al.* [52] An open-ended coaxial probe with an integrated cooling system is positioned in proximity of the cornea. Microwave energy is used to elevate the temperature to 55-58°C in order to shrink the cornea stroma permanently. The stroma is the central, thickest layer consisting of collagen fibers. While the region of shrinkage is a disk about 1 mm in diameter, the enforced cooling spares the

surface to a depth of 0.6 mm. The cooling is integrated to the transmission line by using a hollow inner conductor. The shrinkage results in a flattened cornea that leads to correction of keratoconus.

Eshet *et al.* [98] harnessed the capability of an open-ended coaxial cable to concentrate energy in a small hotspot to implement a microwave drill [53]. The inner conductor of the coaxial cable is extendable. When extended, the open-ended coaxial cable turns into a monopole antenna that functions as the drill bit (see Figure 2-18). The microwave drill can be used for bone drilling application [98]. First, the coaxial cable creates a confined hotspot under its tip. The hotspot increases the dielectric losses on the bone in a thermal runaway process that produces a soft or molten spot for penetration of the extendable inner conductor deeper. An advantage of the microwave drill is that there is no rotating part involved in the process and does not produce debris. Further, the generated heat under the drilling tip may immediately fuse bone vasculature, thereby eliminating hematomas.

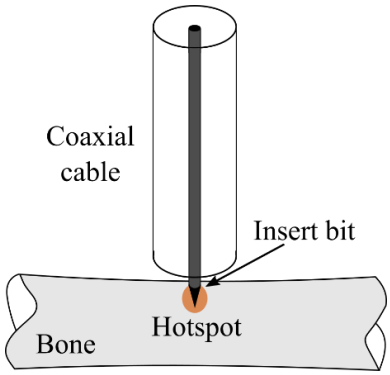

Figure 2-18: Microwave bone drill [adapted from Eshet *et al.* [98]].

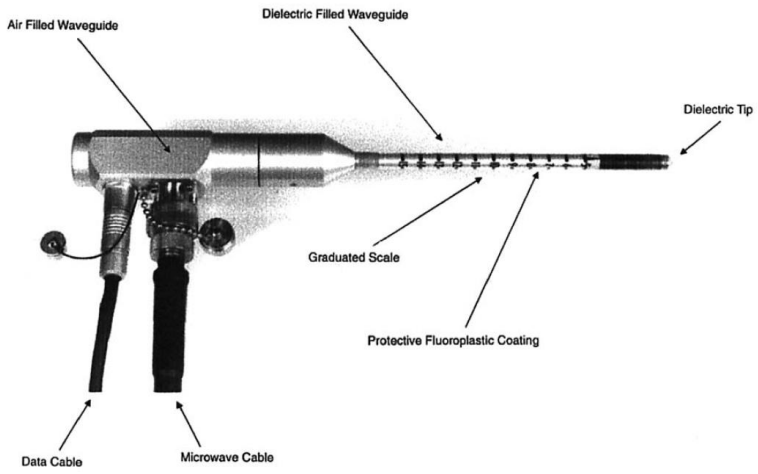

(a)

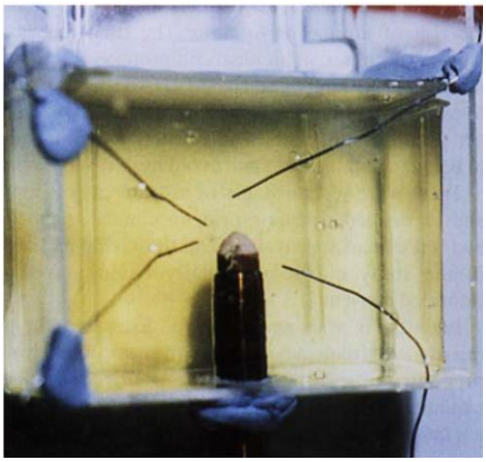

(b)

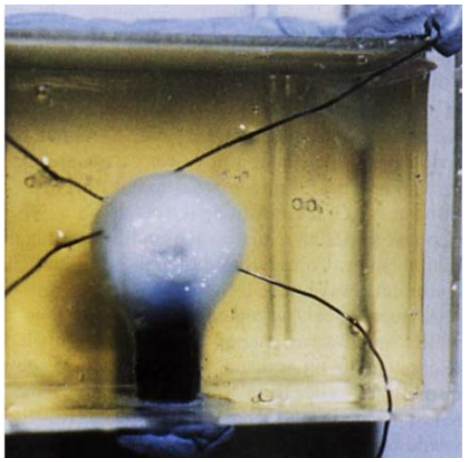

(c)

Figure 2-19: a) 9.2 GHz circular waveguide applicator for endometrial ablation in egg white b) before and c) after ablation [[Reprinted with permission from Hodgson *et al.* [9] Copyright 1999, Wiley].

In Hodgson et al. [9], an open-ended circular waveguide was utilized for endometrial ablation. Endometrial ablation is an alternative option to hysterectomy for treatment of heavy menstrual bleeding. The open-ended waveguide applicator can produce a local hemispherical ablation zone with a radius of 5-6 mm. The applicator is moved inside the uterine cavity in a point-to-point fashion to completely ablate the endometrium layer. A diameter of 8 mm for the applicator has been achieved by choosing an operation frequency

of 9.2 GHz and use of a dielectric inside the waveguide instead of air. The applicator and how it creates a hotspot inside an egg white phantom are shown in Figure 2-19. The dielectric has been extended beyond the waveguide tip and formed in a half circle to prevent perforation of the uterine tissue. The four wires around the tip are temperature sensors. Figure 2-19(b) shows the tip of the device prior to energizing the device and Figure 2-19(c) shows 5 mm coagulated egg white around the tip.

2.3.6 Printed planar applicators

Coaxial-based antennas are the dominant class of applicators for microwave ablation due to their symmetric and minimally invasive profiles. Although printed circuit board technologies such as microstrip provide the freedom to design antennas with diverse ablation patterns, achieving a practical device with an overall diameter less than 3 mm is not feasible at common microwave ablation frequencies of 915 MHz and 2.45 GHz due to large wavelength. In Colebeck *et al.*, a slot antenna was printed on the back side of a microstrip line with ultrawideand (UWB) characteristic [99]. The device is capable of creating ablation zones at 915 MHz, 2.45 GHz, and 5.8 GHz. However, the overall width of the device is 5.5 mm, making it practically unsuitable for most clinical microwave ablation applications.

Operation at higher frequencies allows for designing applicators with practical dimensions due to shorter wavelength of higher frequencies. Assessment-treatment dual-mode applicators have been developed based on open-ended planar coaxial aperture

structure in [54], [55]. In the assessment mode, broadband dielectric properties of the tissue in contact with the aperture is measured. In the treatment mode, power is delivered to the tissue for ablation at 18 GHz. The goal of such a device is to first distinguish malignant tissues from normal ones and then switch to treatment mode to destroy the tumor. A very compact and cost-effective microwave ablation device was implemented in Kim *et al.* [100] by integrating an entire microwave generator consisting of a voltage controlled oscillator, a driver amplifier, and a high power amplifier plus directional coupler and power detectors to a similar dual-mode device by monolithic microwave integrated circuits (MMIC) technology. Figure 2-20 shows another dual-mode applicator consisting of two oval split ring resonator (SRR) printed on the back side of a coplanar waveguide (CPW) [101]. SRR is coupled to the CPW line and is modeled as an LC resonant circuit. Resonant frequency of the SRR is a function of its dimensions and the material it is in contact. The unloaded resonance frequency of the SRR is 12 GHz. The resonance frequency would be different for malignant and normal tissues. Figure 2-21(a) shows measured transmission coefficient of the SRR when loaded with phantoms mimicking normal and tumorous tissues. A shift in frequency of $\Delta f = 350$ MHz has been observed. When tumor is detected, treatment mode is activated and ablation is performed at the resonance frequency. Figure 2-21(b)-(e) shows the simulated and experimental ablation zone of the SRR. In general, the dual-mode applicators are capable of creating ablation zones with input powers as small as 2 W. However, their ablation zone is limited to malignancies smaller than 20 mm [55].

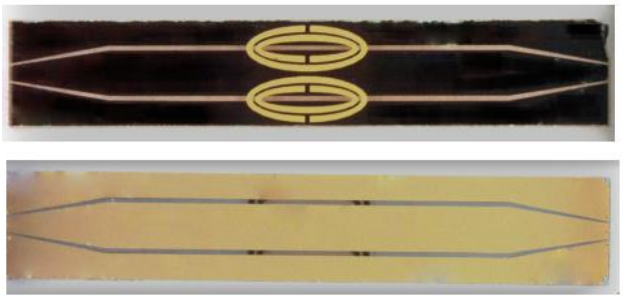

Figure 2-20: dual-mode applicators consisting of oval split ring resonator (SRR) on the back side of a coplanar waveguide (CPW) [Reprinted from Reimann *et al.* [101] under a Creative Commons Attribution 4.0 International license: http://creativecommons.org/licenses/by/4.0/].

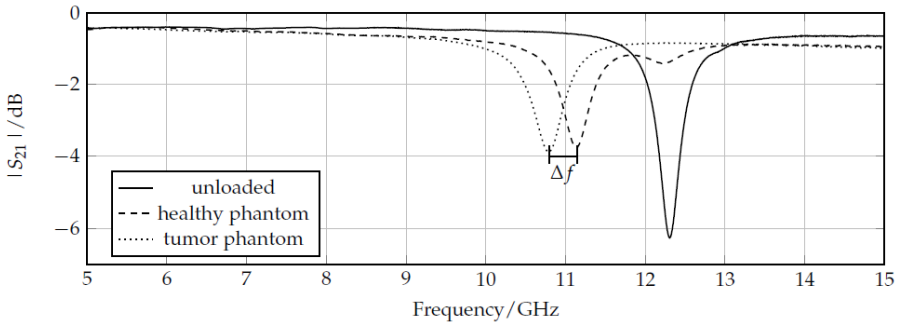

(a)

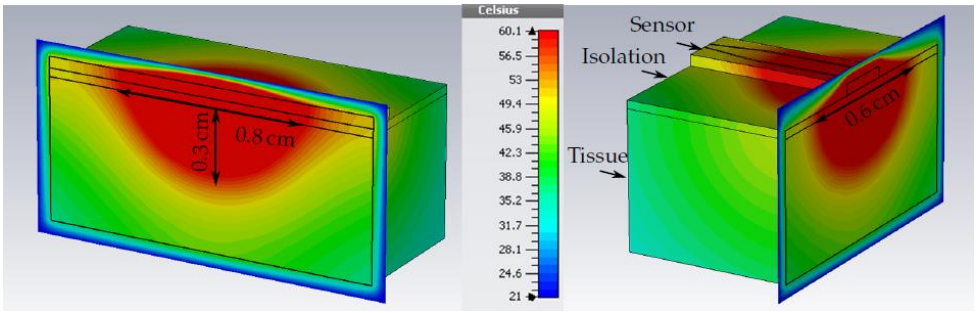

(b)

(c) (d) (e)

Figure 2-21: Performance of the dual mode SRR sensor. Frequency shift in a) assessment mode, b) simulated ablation zone, and c), d) and e) experimental ablation zone in liver tissue in treatment mode [Reprinted from Reimann *et al.* [101] under a Creative Commons Attribution 4.0 International license: http://creativecommons.org/licenses/by/4.0/.].

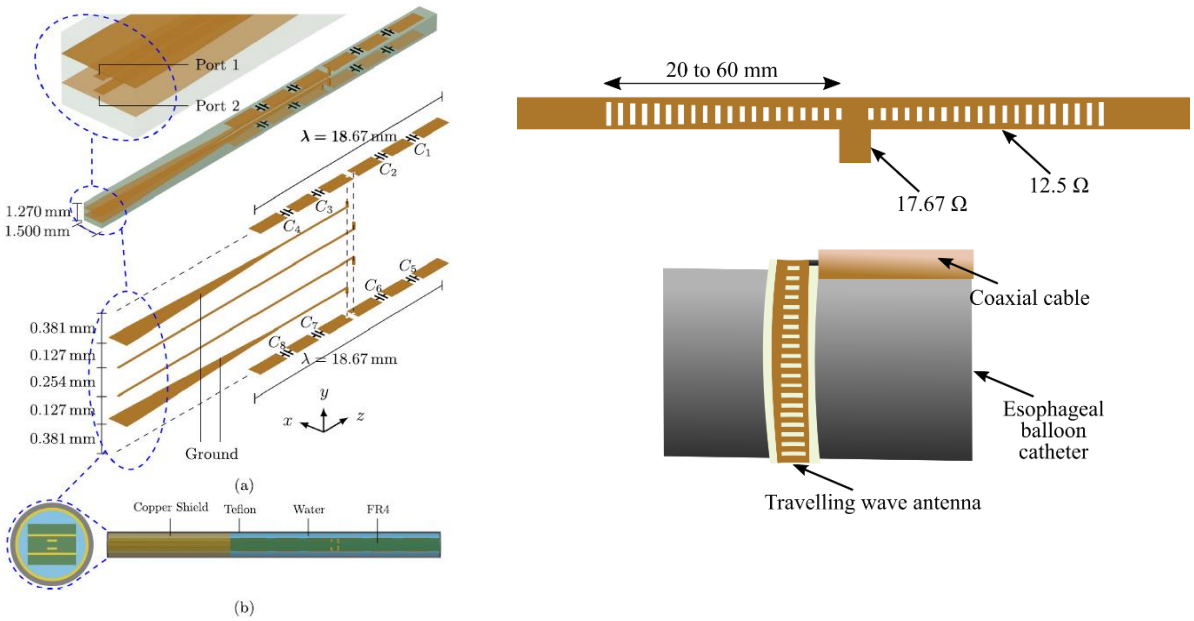

(a) **(b)**

Figure 2-22: a) array of two planar dipoles loaded with capacitors [reprinted with permission from AIP Publishing, Copyright 2017, [102]] and b) a travelling wave antenna [adapted from Hancock *et al.* [61]].

Figure 2-22(a) shows a conceptual design of an array of two planar dipoles loaded with two surface-mount capacitor on each arm [102]. The dipoles are printed back-to-back and fed by stripline. The idea is to obtain the desired ablation pattern by controlling the current distribution on each dipole through optimizing parameters such as the capacitance values, capacitor positions along the arms, and the feed point along the length of the dipole.

Applicability of a travelling wave antenna structure for Barrett's esophagus has been investigated in Hancock *et al.* [61] The goal is to create a band of controlled heating around the sphincter of esophagus to give controlled tightening. As shown in Figure 2-22(b), a series of slots are created on the ground plane of a microstrip line on a flexible substrate. By adjusting the size of each slot, uniform power coupling from the microstrip

line to slots is achieved. This leads to uniform heating along the microstrip line. Two 30-slot structures have been fed by a coaxial cable in a "T" arrangement in order to have enough length for creating a band of 270° ablation zone. An operation frequency of 14.5 GHz has been selected to have a very shallow heating, thereby preventing muscle damage or perforation. For deployment inside the esophagus, the antenna has been attached to the outer surface of a balloon. The balloon will be inserted into esophagus through the instrument channel of a gastroscope in deflated form and will be inflated by filling the balloon with air or a liquid such as saline solution.

In a pre-clinical study, efficacy of a resonant planar structure integrated to a electrosurgical device has been investigated for endoscopic procedures [103]. The device uses RF energy to cut, microwave energy to coagulate and injects fluids to raise the lesion from the wall of the body lumen. The microwave coagulator is a half wavelength microstrip line resonating at 5.8 GHz with dimensions of 2 and 8.66 mm for width and length respectively. The top and bottom plates of the microstrip also act as the bipolar RF scalpel. The selected frequency of operation provides well-controlled coagulation depth.

2.3.7 Additional designs

Although the common radiation pattern of microwave ablation applicator is omnidirectional, other designs have been developed with different radiation patterns for

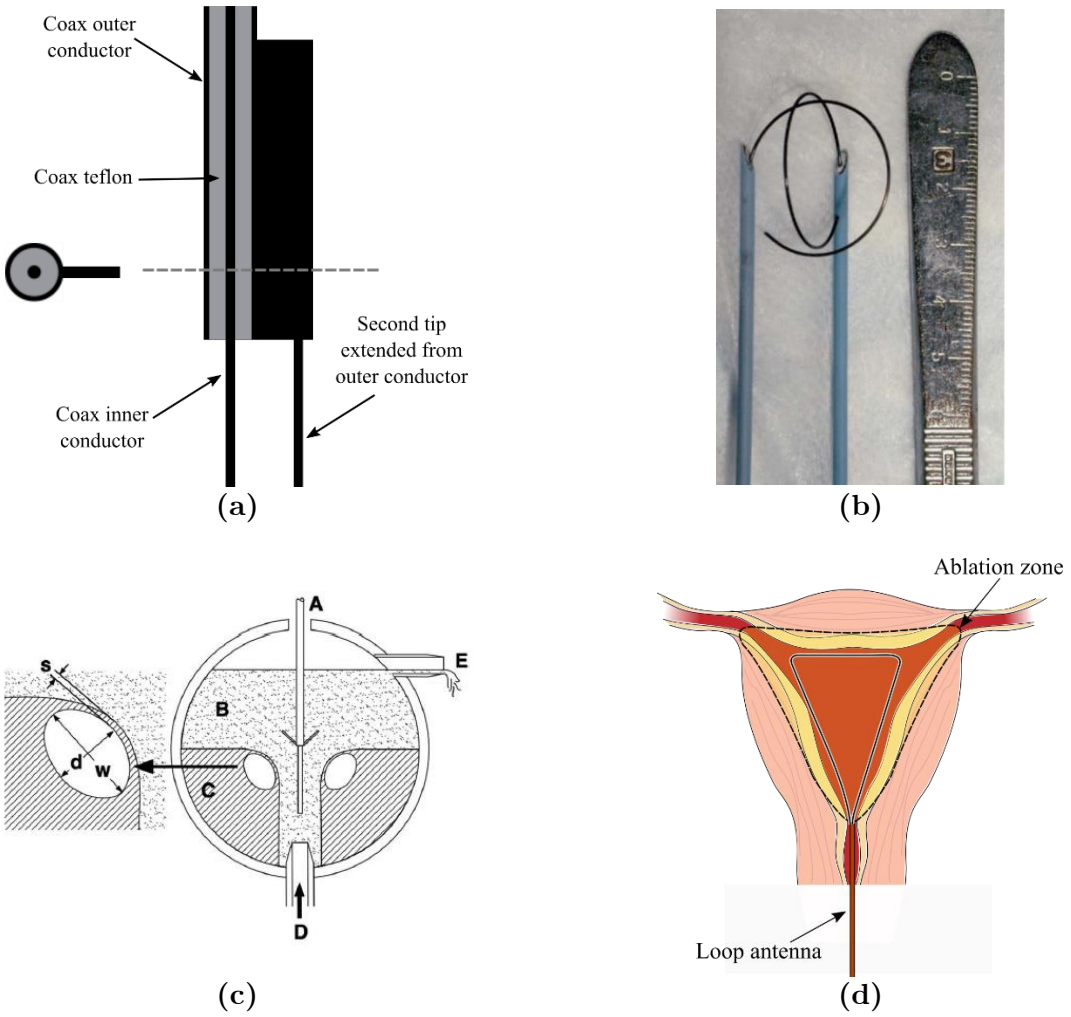

Figure 2-23: a) two prong fork device for treatment of snoring [adapted from Cresson *et al.* [104]], b) double loop applicator [reprinted with permission from Springer Nature, Copyright 2005, [105]] c) Drooped ground monopole antenna [reprinted with permission from John Wiley and Sons, Copyright 2015, [106]], and d) loop antenna for global endometrial ablation [adapted from Fallahi *et al.* [23]].

applications such as snoring treatment, tumor ablation, noncontact circumferential endocardial ablation, and global endometrial ablation (see Figure 2-23).

In Cresson *et al.* [104], a two-prong fork made of coaxial cable has been developed for snoring treatment. Figure 2-23(a) shows that one prong of the applicator is the extension of the coaxial cable inner conductor and the other one is a needle electrically

connected to the coaxial cable outer conductor. This configuration would create a hotspot at the tip of the prongs while less heat is generated on the proximal end. The treatment goal of the device is to create a deep-seated fibrous scar in the soft palate tissue while sparing its surface by constraining the temperature. Ablation would change the soft palate to fibrous scar that reduces vibratory capacity of the soft palate, thereby decreasing the snoring.

Most of the implemented applicators for microwave ablation of tumors are inserted into the center of the tumor and create an outward growing ablation zone to cover the whole tumor. In Shock *et al.* [107], a monopole antenna was suggested that takes a loop form when deployed (see Figure 2-23(b)). With this design, the tumor is encircled by the loop and is heated from the outside in. This may help in rapid truncation of the blood supply to minimize the blood heat sink effect. Further, the loop configuration would decrease tumor recurrence due to malignant cell proceeding during placement of needle form applicators since it is positioned next to the tumor. It is noted that for a complete coverage of the tumor, more than one applicator would be required due to less symmetric ablation pattern of the loop. Some disadvantages of the loop design is the more complicated targeting procedure of the tumors. Moreover, the loop is energized during deployment for easier placement that can cause complications if it hits surrounding critical organs [107].

A monopole with drooping ground radial wires has been implemented for noncontact circumferential endocardial ablation in [106]. As shown in Figure 2-23(c), the design target is to create a circumferential ablation pattern in the antrum of the pulmonary vein for isolation of the source of atrial fibrillation. Theoretically, addition of four 45° drooped radial wires electrically connected to the outer conductor provides a pure resistive 50 Ω input impedance. Radial wires usually have a length of $\lambda_{\text{effective}}/4$ and play the role of a ground plane. The radiation pattern of this antenna is above its ground plane. In other words, the radiation pattern is tilted toward the monopole arm and is slightly directional. This design takes advantage of the pulmonary vein flow for keeping the surface of the myocardial tissue.

Figure 2-23(d) shows a loop antenna inserted to the uterine cavity for globally ablating its inner lining, endometrium layer, as a treatment for heavy menstrual bleeding [23]. The loop consists of an extension of the inner conductor of a coaxial cable that is electrically connected to the coaxial cable outer conductor at its tip. The large loop antenna is resonant at a perimeter of one wavelength and changing its shape does not appreciably change the loop resonant frequency. The loop is inserted into the uterine cavity in an endocervical approach and deployed inside the cavity. Small diameter of the device does not require any dilation of cervix. The loop conforms to the anatomy of the uterine cavity and create a planar ablation pattern. Microwave energy is majorly delivered along the loop wire whereas center of the loop is ablated through thermal conduction.

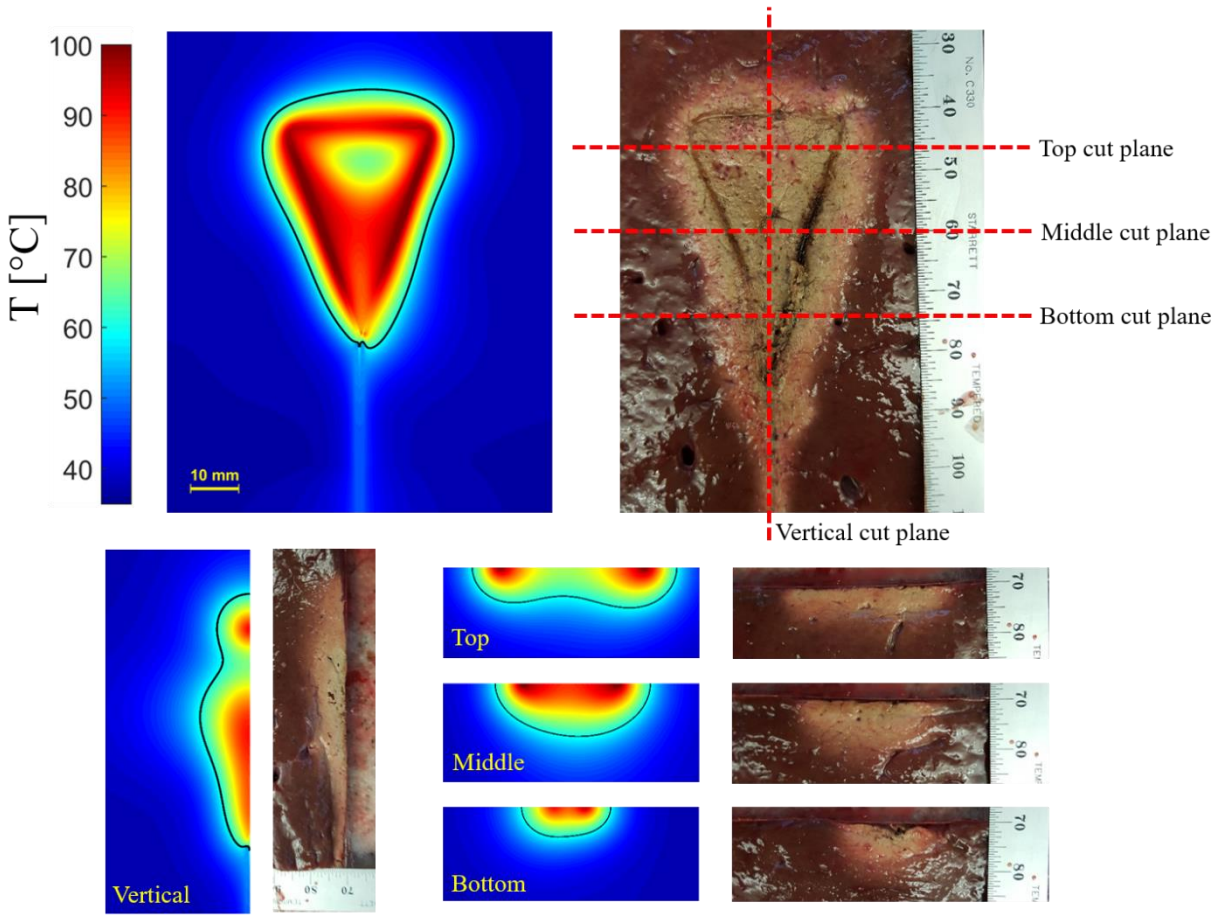

Figure 2-24: Simulated and experimental ablation pattern of a loop antenna with planar heating. Estimated extent of the ablation zone (60 °C isotherm) are overlaid on the simulated temperature profiles.

Simulated and experimental ablation patterns shown in Figure 2-24 confirms creation of planar ablation patterns in the shape of the loop. Ablation depth at different cuts are also shown in Figure 2-24.

2.3.8 Alternative ablation pattern control techniques

Ablation pattern in microwave applicators is basically defined by the antenna type. Alternative techniques to shape or tailor the antenna pattern have been incorporation of

cooling, use of balloon, shifting to higher frequencies, and employing multiple devices in an array configuration.

Use of a balloon is an effective technique in intracavitary applications such as Barrett's esophagus, renal denervation, benign prostate hyperplasia (BPH) and cardiac ablation [96], [108]–[110]. While the microwave antenna is held in the center of the balloon, the balloon is inflated and filled with a coupling material such as saline or gel. These materials provide more efficient coupling of power from the antenna to the tissue compared to air since their electrical properties are similar to body tissues. In Qian *et al.* [109], deep circumferential heating is reported while sparing transmural arterial wall in renal denervation application.

Microwave ablation has shown that it is capable of creating larger ablation zones compared to RF ablation. However, a single microwave applicator with optimal spherical ablation zone may not be large enough to cover a large tumor (3 cm in diameter) plus a healthy margin [111]. Heat sink effect of local blood flow is the main reason of this limitation that can increase the chance of incomplete ablation and risk of tumor recurrence. Thus, the use of multiple applicators has been proposed to achieve larger ablation volume. SAR pattern of arrays of four antennas in square configuration has been investigated for different antenna types in Ryan *et al.* [71]. Helical antenna in square and crescent array form has been investigated in Sherar *et al.* [112] for prostate cancer thermal therapy. Feasibility of using triple microwave antennas simultaneously in the treatment

of liver tumors intraoperatively has been shown in [113]. Array of multiple antennas may not create a spherical ablation zone but the final ablation pattern can adequately cover the tumor by precise placement of the antenna elements.

2.4 Summary

There has been considerable interest in development of microwave ablation technology for a range of clinical indications. A critical component of microwave ablation systems is the applicator, which includes an antenna for coupling applied microwave power from a generator to the targeted tissue. Here, we have reviewed microwave antennas designed for site-specific thermal ablation of tissue. The use of active cooling strategies for minimizing unintended heating along the feeding transmission line, and antenna chokes/sleeves and cooling for adjusting the length of ablation zones were discussed. Ongoing developments incorporating sensors for assessing treatment progress may yield improved control of microwave thermal ablation zones.

3 Design of a Microwave Global Endometrial Ablation Device[2]

3.1 Introduction

Menorrhagia, a condition when menstrual periods have abnormally heavy or prolonged bleeding, significantly affects quality of life, and affects ~20% of women of reproductive age [114]. Surgical interventions have been the standard treatment when medical therapy fails to mitigate the symptoms. Surgical options include hysterectomy or resectoscopic techniques such as transcervical resection of the endometrium (TCRE), roller-ball, and endometrial laser ablation [115]. The main goal of endometrial ablation is to stop or reduce the heavy menstrual bleeding by thermal coagulation of the endometrium (i.e., the inner lining of the uterus). In a thermal ablation procedure, an energy delivery applicator is

[2] This chapter has been published as: H. Fallahi and P. Prakash, "Design of a Microwave Global Endometrial Ablation Device," IEEE J. Electromagn. RF Microw. Med. Biol., 2019. (DOI: 10.1109/JERM.2019.2893280)

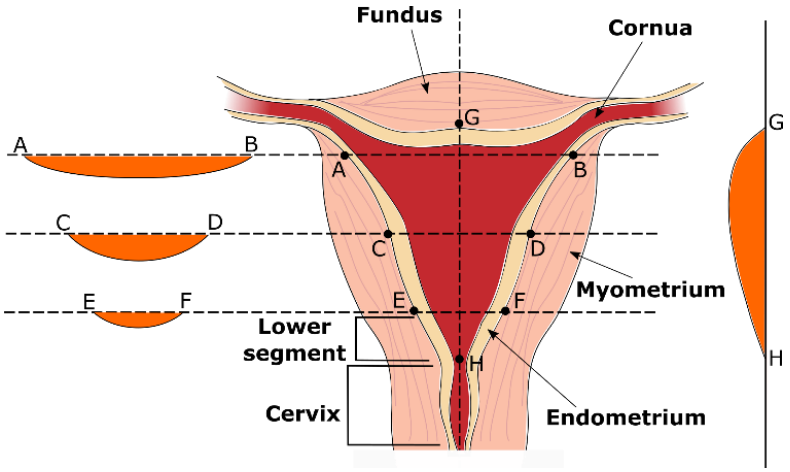

Figure 3-1: Illustration of the uterine cavity geometry and clinically relevant endometrial ablation profiles shown in orange along axial (A—B, C—D, and E—F) and sagittal sections through the uterus (G—H).

inserted into the uterine cavity via the endocervical canal to deliver therapeutic energy while sparing the cervix. Energy may be delivered in a global or local manner. Local ablation devices deposit localized energy to a small portion of the endometrial lining and thus require translation and repositioning of the applicator to cover the entire target volume for an effective treatment. Global endometrial ablation (GEA) devices afford ablation of the entire target with a single positioning of the device. Compared to local ablation approaches, GEA techniques are less dependent on operator skill and experience and offer the advantages of improved safety and efficacy, and reduced procedure time [116].

As illustrated in Figure 3-1, GEA requires the creation of a near triangular shaped ablation pattern, conformal to the anatomy of the uterus. The desired ablation depth in the uterus mid-body ranges from 3 – 9 mm for hyperthermic ablation devices [9], [117], [118] and 9 – 12 mm for cryoablation devices [119], with ablation depth tapering toward

the cornua and lower segment of the uterus where myometrial tissue is thin. GEA applicators are ideally delivered to the uterine cavity without dilation of the cervix, and should be able to treat uterine cavities of length and width ranging from 4 – 6.5 cm (along the G – H axis in Figure 3-1) and 2.5 – 4.5 cm (along the A – B axis in Figure 3-1), respectively [120]. Finally, it is desirable for GEA systems to incorporate mechanisms for automatic determination of treatment endpoint, ensuring adequate ablation of the endometrium, while precluding damage to surrounding tissue.

Previous efforts have investigated a variety of energy modalities and delivery methods for GEA, which have resulted in several systems in clinical use, including thermal balloon [121], circulated hot fluid [122], cryoablation [123], radiofrequency ablation (RFA) [65]. RFA is the most commonly used energy-modality for GEA [124]. Compared to RFA, microwaves have the ability to travel through charred tissue and vapor, do not require electrical contact between the applicator and targeted tissue, may have small applicator diameter, and are less susceptible to large blood vessel heat sinks [56]. While microwave applicator designs have been extensively investigated for local endometrial ablation and for tumor ablation, antenna designs for GEA have not received much attention.

Prior studies have explored rigid catheter-based microwave applicators for local endometrial ablation. A curved 2.45 GHz microwave applicator was developed for effective energy deposition along the endometrial lining [125]. The curved form of the device facilitates access to the cornua of the uterus. Another design employs a dielectric filled

circular waveguide which radiates microwaves at 9.2 GHz [9]. These designs have a local action, and thus require the applicator to be translated within the uterine cavity in a point-to-point manner to cover the entire target. Microwave ablation systems are also in clinical use for treatment of tumors in the liver [1], lung [2], kidney [3], and bone [126]. In these applications, the microwave ablation antenna is typically incorporated within a needle-like applicator to facilitate percutaneous insertion under image-guidance. The radiation pattern of these applicators is generally axisymmetric [21] and optimized to create large near-spherical ablation zones for treating tumors in highly vascular organs [127]. Recent research efforts have been focused on: techniques for limiting the length of ablation zones due to unsuppressed currents on the surface of unbalanced antenna designs [44], [45], [47], [79], [82], [85], [128]; antenna designs with directional radiation patterns [50], [51], [90]; and assessment of microwave ablation at high frequencies [63]. The ablation pattern of these antennas is generally not suitable for global endometrial ablation.

In [23], we presented a preliminary investigation of a microwave antenna for GEA. Although the proposed antenna illustrated preliminary feasibility of using microwaves for GEA, the study did not consider the feasibility of treating uterine cavities of varying sizes, which will be important for practical clinical application of the proposed technology. Here, we present a detailed investigation and characterization of microwave loop antennas for GEA and employ computational models and benchtop experiments to assess their suitability for treating uterine cavities ranging from 2.5 – 4.5 cm in width and 4 – 6.5 cm

in length. Our results illustrate the ability to achieve conformal thermal ablation of the endometrial lining by appropriately shaping a microwave loop antenna and the use of passive elements.

3.2 Material & Methods

We employed a simulation-based approach to optimize the design of microwave GEA applicators. The objectives in the simulation phase were to identify an antenna design with ablation profile suited to the requirements for GEA (Figure 3-1) while maximizing the antenna return loss (RL) at the operation frequency. After determining the optimal antenna dimensions from simulations, proof-of-concept devices were fabricated and experimentally evaluated in *ex vivo* tissue.

3.2.1 Microwave loop antenna design

A loop antenna consists of a length of electrical conductor that is electrically connected on each end to a transmission line. The large loop antenna is resonant at a perimeter of one wavelength and the maximal radiation is perpendicular to the plane of the loop. Loop antennas can be designed to resonate at multiples of a wavelength and changing the shape of the loop does not appreciably alter the loop resonant frequency [91].

We selected a coaxial wire fed loop antenna for GEA due to its simple structure, and its suitability for being introduced to the uterine cavity via a transcervical approach. Radiating sections of the device were loaded with dielectric (PTFE, $\epsilon_r = 2.1$) to prevent

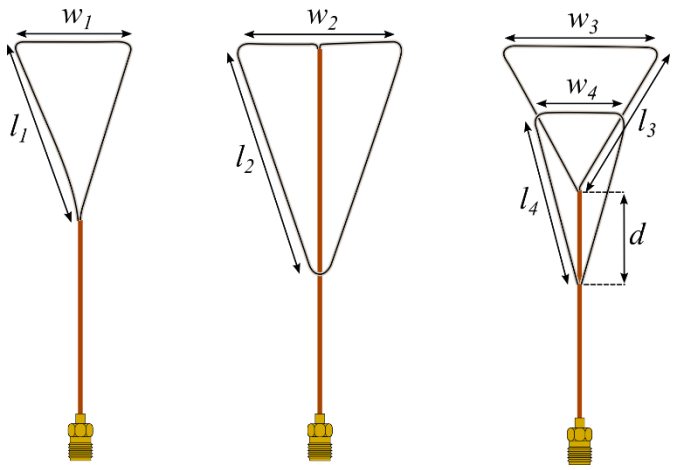

Figure 3-2: Proposed loop antennas for microwave GEA a) simple loop antenna, b) delta loop antenna, and c) loop antenna with a passive element.

direct contact of metallic elements with tissue; this choice was made since tissue desiccated after ablation may adhere to metal, and thus complicate withdrawal of the ablation device. The perimeter of the uterine cavity may range from 109 – 182.5 mm [120], [129]. We selected an operating frequency of 915 MHz since it lies within a band of frequencies allocated for industrial, scientific, and medical (ISM) use, and provides a balance between the rate of heating and wavelength relative to the size of uterine cavities.

Three types of loop antennas illustrated in Figure 3-2, were investigated in this study. The loop antenna shown in Figure 3-2(a), referred to as the simple loop, with dimensions l_1 = 47.5 mm and w_1 = 30 mm was formed by stripping a length of 125 mm of outer conductor of coaxial cable and forming a triangle similar to uterine cavity. To complete the loop, the tip of the inner conductor was electrically connected to the outer conductor. We employed electromagnetic simulations to iteratively adjust the loop antenna length to resonate at 915 MHz where the antenna RL was maximized. These

simulations yielded a loop antenna length of 125 mm at which RL (RL $>$ 10 dB) is maximum and specific absorption rate (SAR) pattern is conformal to the anatomy of the uterine cavity. The final length is also in close agreement with the effective wavelength of 122 mm for an insulated antenna in tissue [130].

We hypothesized that the simple loop antenna may not be suitable for treating large uterine cavities due to its limited length. The antenna of Figure 3-2(b), referred to as the delta loop antenna, with dimensions of $l_2 = 65$ mm and $w_2 = 45$ mm, was designed at larger multiples of a wavelength with the goal of achieving an overall loop length close to the perimeter of the largest uterine cavity (182.5 mm), while maintaining an adequate RL. Finally, the antenna in Figure 3-2(c), referred to as the loop antenna with a passive element, was designed by augmenting the simple loop antenna of Figure 3-2(a) with a passive electrically conducting element. The two ends of the passive element are electrically connected to the feed coaxial cable at a distance of $d = 25$ mm from the coax cable distal end to form a passive loop. The rationale for investigating the use of the passive element was to assess its suitability for extending the ablation zone for treating large cavities. A time-varying electromagnetic field incident on the passive conductor induces a time-varying current on the passive conductor, resulting in a radiated electromagnetic field. Interactions between the electromagnetic fields radiated from the loop antenna and the passive element provide an opportunity for adjusting the net electric field within the cavity. Passive elements have been extensively employed in antennas for

gain, directivity, and bandwidth improvement [91], [131]–[133] for applications in communications. We hypothesized that the passive element would redistribute electromagnetic power within the uterine cavity, and thus provide a means for extending the ablation profile. The length and shape of the active loop (l_3 = 40 mm and w_3 = 45 mm) and passive element (l_4 = 42 mm and w_4 = 25 mm) were selected to conform to the lower body of the uterine cavity.

3.2.2 Simulation-based antenna optimization and evaluation

We employed a coupled 3D electromagnetic-heat transfer finite element method (FEM) model, implemented with COMSOL Multiphysics, v5.3, for design optimization of the loop antenna for GEA. The device was modeled as being centrally positioned within a cylindrical block of tissue as shown in Figure 3-3(a).

The model initially solves the time-harmonic Helmholtz wave equation to determine the electric field profile in tissue:

$$\nabla^2 \mathbf{E} - k_0^2 \left(\epsilon_r - \frac{j\sigma}{\omega \epsilon_0}\right) \mathbf{E} = 0 \qquad (1)$$

where $\mathbf{E}$ [V/m] is the electric field, k_0 [m^{-1}] is the free space wavenumber, ϵ_r is the relative real permittivity, σ [S/m] is the effective electrical conductivity, ω [rads/s] is the angular frequency, and ϵ_0 [F/m] is the permittivity of free space. In (1), ϵ_r and σ of tissue are both temperature-dependent. In the second step, the solver uses the wave equation

solution, electric field **E**, to compute volumetric power deposition, Q [W/m^3], as the source term in the heat equation [134]:

$$Q = \frac{1}{2}\sigma|\mathbf{E}|^2 \tag{2}$$

$$\rho c_l \frac{\partial T}{\partial t} = \nabla \cdot (k\nabla T) - \omega_b \rho_b c_b (T - T_b) + Q \tag{3}$$

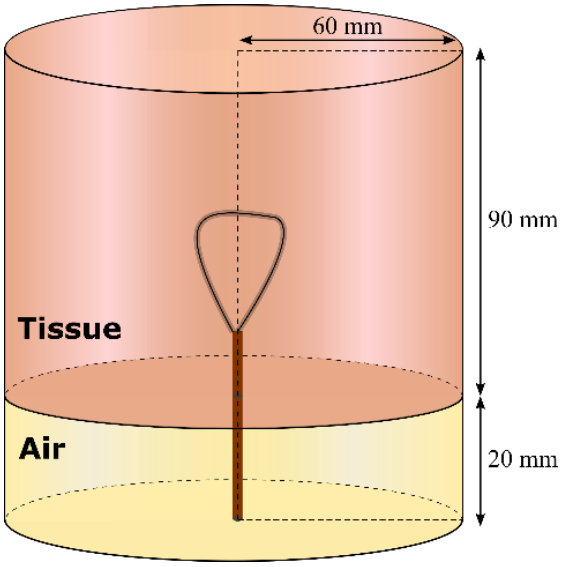

(a)

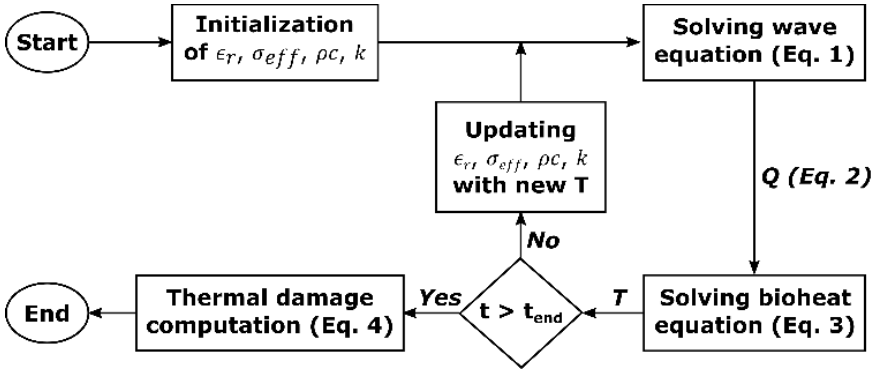

(b)

Figure 3-3: a) Illustration of the geometry employed in computational models and b) solver flow diagram.

where T [K] is temperature of the tissue, ρ is the density of tissue (1050 kg/m^3), c_l [J/(kg·K)] is the heat capacity of tissue at constant pressure, k [W/(m·K)] is the thermal conductivity of liver, ω_b is rate of blood perfusion (0.0028 $m_b^3/(m_t^3 \cdot s)$[135]), ρ_b is blood density (1080 kg/m^3 [135]), c_b is blood specific heat capacity (3500 J/(kg·K) [135]) and T_b is the physiological blood temperature (i.e. 37 °C). The heat capacity c_l and thermal conductivity k are other temperature-dependent tissue parameters. Solution of the heat equation, T, is used to update the four temperature dependent parameters of the tissue using the functions summarized in Table 3-1.

Table 3-1: Tissue physical properties used in the simulations.

Parameter	Unit	Value @ 37 °C	Temperature-dependent formula
Relative real permittivity, ϵ_r [136]	—	46	$\epsilon_r(T) = 46\left(1 - \frac{1}{1+\exp[0.0764(82.271-T)]}\right)+1$
Effective conductivity, σ_{eff} [136]	S/m	0.86	$\sigma(T) = 0.86\left(1 - \frac{1}{1+\exp[0.0697(85.375-T)]}\right)$
Volumetric heat capacity, ρc [137]	J/(m^3·K)	4,000,000	$\rho c(T) = \begin{cases} \rho c_0 & for\ T < (100 - \frac{\Delta T}{2}) \\ \frac{\rho c_0 + \rho c_v}{2} + \frac{\rho_w \cdot L \cdot C}{\Delta T} & for\ (100 - \frac{\Delta T}{2}) < T < (100 + \frac{\Delta T}{2}) \\ \rho c_v & for\ T > (100 + \frac{\Delta T}{2}) \end{cases}$
Thermal conductivity, k [137]	W/(m·K)	0.5	$k(T) = \begin{cases} k_0 + \Delta k[T - T_0] & T \le 373\ K \\ k_0 + \Delta k[373 - T_0] & T > 373\ K \end{cases}$
Uterus Blood perfusion, $\omega_b \rho_b c_b$ [135]	W/(m^3·K)	10584	$w(T) = \begin{cases} \omega_b \rho_b c_b & 0 < T < 325.15\ K \\ 0 & 325.15\ K < T < 1000\ K \end{cases}$

Since no measured temperature-dependent data is available in the literature for permittivity and conductivity at 915 MHz at ablative temperatures (i.e. 50 – 120 °C), we approximated temperature-dependent changes at 915 MHz using the sigmoid temperature dependence of dielectric properties reported at 2.45 GHz, while scaled appropriately for

915 MHz. Updated parameters are used in the next time step to compute new values for the electric field and temperature. This procedure continues for the defined simulation time. Finally, thermal damage induced by microwave radiation in tissue is calculated as a function of time and temperature by using an Arrhenius model [41] to obtain the ablation profile

$$\Omega(\tau) = \int_0^\tau A \cdot \exp\left(-\frac{E_a}{RT(t)}\right) dt \tag{4}$$

where Ω (τ) is a dimensionless damage parameter, A is frequency factor (5.51×10^{41} s^{-1}), E_a is energy barrier (2.769×10^5 J/mol), R is gas constant (8.3143 J/mol·°C), $T(t)$ stands for the time development of the spatial temperature profile, and τ is the total time for which the thermal damage in the tissue was accumulated. These values of E_a and A were selected to model tissue discoloration following heating, allowing for comparison with experimental ablation zones [138]. A value of damage parameter Ω (τ) = 1 (corresponding to 63% of the thermal damage process being complete) was chosen as a threshold for assessing the extent of the ablation zone. Figure 3-3(b) shows the simulation flow diagram.

First-order scattering boundaries were defined for all outer boundaries,

$$\mathbf{n} \times (\nabla \times \mathbf{E}) - jk\mathbf{n} \times (\mathbf{E} \times \mathbf{n}) = 0 \tag{5}$$

where $\boldsymbol{n}$ is normal vector to the boundary and k [m^{-1}] is the wavenumber. This boundary is appropriate given the lossy nature of tissue at the 915 MHz operation frequency. The

initial tissue temperature was set to 37 °C in the whole simulation domain. A thermal insulation boundary condition was set at the outer simulation boundaries. A non-uniform mesh was employed, with finest meshing at the antenna feed (maximum element edge length = 0.5 mm) and coarsest mesh in regions further away from the radiating element (maximum edge element length = 7.5 mm). The number of degrees of freedom in each model was 1.75 million on average. A direct solver (MUMPS) was utilized for these simulations.

3.2.3 Device fabrication and experimental evaluation

Proof-of-concept devices were fabricated in our lab using UT-34 coaxial cable. This cable was selected due to its small diameter (0.86 mm). We note that in clinical practice, cable cooling would likely be required to mitigate passive heating of non-targeted tissue in contact with the cable. The small size of the UT-34 cable would allow for incorporation of cooling while restricting overall applicator diameter to ~2.5 mm, as we have previously reported in [90].

In the experimental setup for evaluating the ablation profile, microwave power was provided to the devices from a solid-state amplifier (RFcore Co., RCA0527H49A). An inline power meter (Bird 7022) was used to monitor the forward and reflected power during ablation (see Figure 3-4). *Ex vivo* experiments were perIran+rouge1formed in bovine liver, which is an established experimental model for characterizing thermal ablation devices [127]. Fresh bovine liver was transported from a local slaughterhouse to

our lab in sealed plastic bags placed on ice. The liver was cut into 12 cm × 10 cm × 5 cm pieces and each piece, in sealed plastic bags, was placed in a tub with circulating water to warm the tissue to a temperature of ~37 °C prior to each experiment in order to emulate physiologic temperature. To mimic device positioning within the uterine cavity, each device was placed in between two pieces of liver. After each experiment, the top and bottom liver pieces were sectioned and ablation depths were measured at different points as shown in Figure 3-5. These points were chosen in order to characterize the extent of the ablation zone along key positions within the uterine cavity: fundus, mid-body, and lower region of the endometrium. The Extent of the ablation zones was determined based on the pattern of visibly discolored tissue. For each candidate device, experimental ablations were performed in triplicate (i.e. $n = 3$).

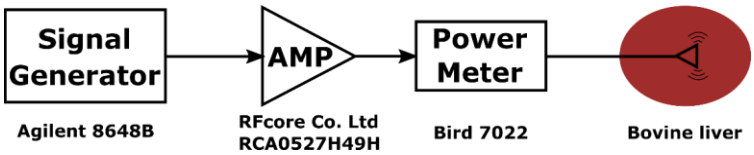

Figure 3-4: Experimental setup for evaluating the ablation profile of the proposed antennas.

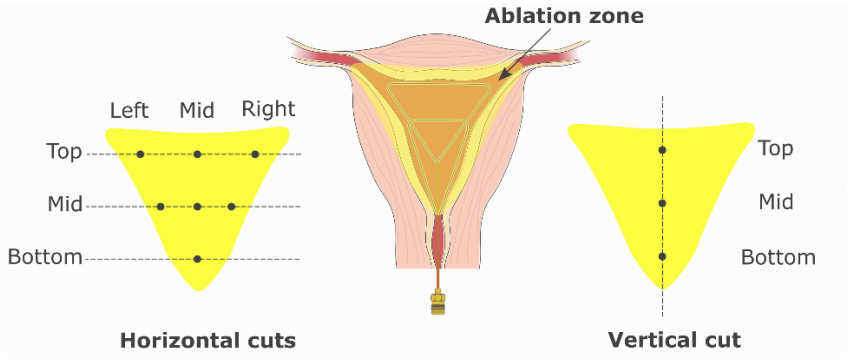

Figure 3-5: Illustration of the axes along which tissue was sectioned following ablations for measuring experimental ablation zone depths: (left) bottom piece and (right) top piece.

3.3 Results & Discussion

3.3.1 SAR and impedance matching

The normalized electromagnetic power loss density (Q_e) provides an understanding of the spatial distribution of electromagnetic power absorbed within tissue. As shown in Figure 3-6(a), the Q_e profile of the simple loop antenna indicates that the power is predominantly deposited within tissue regions along the radiating loop antenna element. Tissue regions within the center of the radiating loop receive limited electromagnetic power. However, as experimentally demonstrated in our preliminary study [23], passive heat transfer from regions along the loop with greater power density can be relied upon to achieve conformal ablation through careful selection of applied power level and heating time.

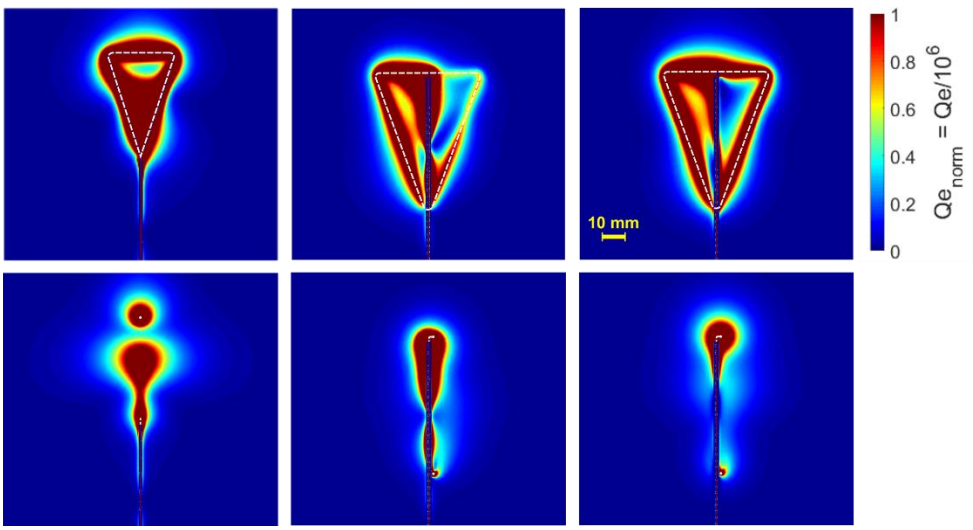

Figure 3-6: Electromagnetic power loss density (Q_e) of a) simple loop, b) delta loop at 915 MHz, and c) delta loop at 650 MHz in coronal (top row) and sagittal planes.

Figure 3-7 shows that with l_1 = 47.5 mm and w_1 = 30 mm, the antenna is well matched at 915 MHz. However, the proposed loop antenna is only effective for GEA over a limited perimeter range (109 – 125 mm) of uterine cavities due to its short perimeter. To address this problem, we designed the delta loop antenna with a length of 175 mm. The longer length has the effect of reducing the resonant frequency (see Figure 3-7). Further, the extent of the tissue region with limited power absorption can be expected to be larger, and thus may not be adequately ablated. To address this shortcoming, we investigated a delta loop antenna, folding the loop to use a section of the feeding coaxial cable as a passive element (see Figure 3-2(b)). For practical reasons, it may be preferable to operate the ablation system at 915 MHz because this frequency lies within an ISM frequency band. While the resonant frequency of the delta loop is 650 MHz, note that the measured RL is approximately 7 dB at 915 MHz. This RL would correspond to a reflected power in the range of 12 – 18 W (20%) for forward power in the range of 60 – 80 W. Although the amount of the reflected power at 915 MHz is not negligible, it may still be practical to operate the loop at 915 MHz by incorporating a circulator at the output of the power amplifier of the final ablation system for protection from high reflected power. However, Figure 3-6(b) indicates that the delta loop antenna's Q_e profile at 915 MHz is concentrated along a portion of the loop, with other regions receiving little power, likely leading to inadequate ablation depth. The Q_e profile for the delta loop antenna operating at 650 MHz, shown in Figure 3-6(c), is more evenly distributed along the length of the loop. In this case, tissue within the inner section of the loop would require a longer time

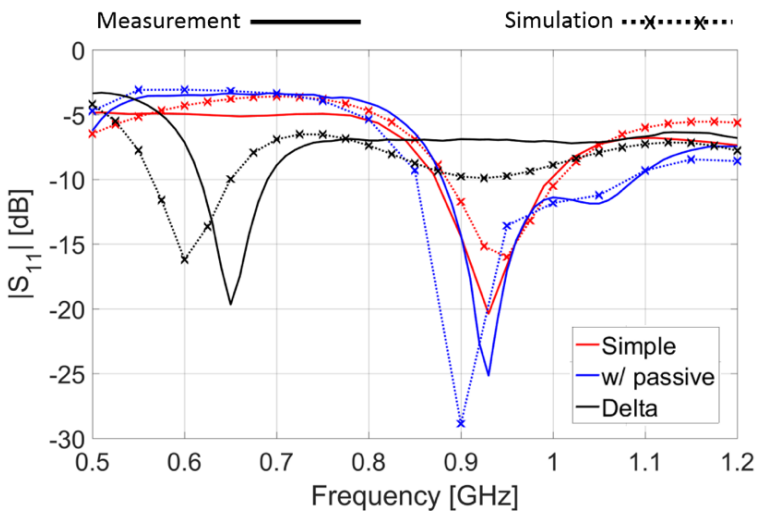

Figure 3-7: Simulated and measured return loss (RL = -|S_{11}|) of the simple loop antenna, delta loop antenna, and loop antenna with a passive element.

to be completely ablated by thermal conduction compared to Figure 3-6(a). While it may be possible to fill in the gap by extending applied power and ablation duration [139], this approach may also lead to over-ablation in other tissue regions, such as those in proximity to the radiating loop. A further limitation of this design is that the 650 MHz operating frequency does not lie within an ISM frequency band, thus there may be hurdles in practical implementation of such a system.

We next investigated a 125 mm loop antenna augmented with an independent passive electrically conductive element, illustrated in Figure 3-2(c). Addition of the passive element does not have a significant effect on RL of the loop antenna as shown in Figure 3-7. Figure 3-8(a) illustrates the simulated electromagnetic power loss density in tissue for the input power of 60 W at 915 MHz for the device with a passive element. This profile indicates that power is mostly deposited along the active and passive wires. Power

deposition inside the loop is similar to that of the simple loop (See Figure 3-6(a)). However, incorporating a passive element extends power deposition to the lower regions of the uterine cavity. Figure 3-8(b) shows the corresponding temperature profile for an ablation duration of 180 s. The thermal damage induced in tissue following ablation was estimated as a function of time and temperature with and without blood perfusion using the Arrhenius model overlaid on the temperature profile. Simulation showed that the heat-sink effect of blood perfusion can be compensated by increasing the input power from 60 W to 66 W. Further simulations showed that there were no significant changes in the simulated ablation profiles when using dielectric properties of liver tissue and uterine tissue (simulated ablation volume = 22814 mm^3 when using dielectric properties of liver tissue and 24081 mm^3 when using dielectric properties of uterine tissue).

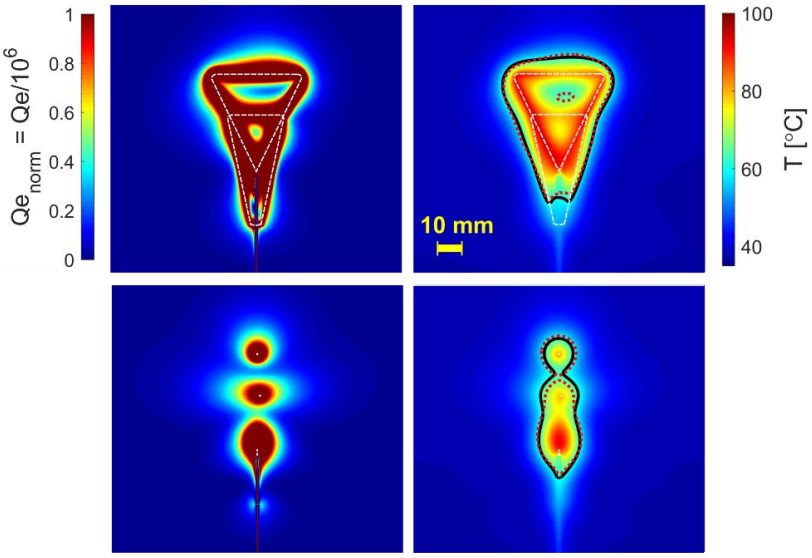

(a) (b)

Figure 3-8: Simulated a) Q_e and b) temperature profile in coronal (top row) and sagittal planes overlaid by thermal damage contour ($\Omega = 1$, black solid line: without perfusion, red dotted line: with perfusion) of the loop antenna with passive element for input power of 60 W and ablation duration of 180 s.

3.3.2 Experimental verification of thermal ablation patterns

Figure 3-9 shows example ablation profiles for the loop antenna, delta loop antenna (operating at both 915 MHz and 650 MHz), and the loop antenna with a passive element. Figure 3-9(b) and (c) show incomplete ablation in the same regions identified from simulation (see Figure 3-6). Although Figure 3-8(a) and (d) illustrate that the simple loop antenna and the loop antenna with passive element yield complete ablation profiles, it should be noted that the width and length of the ablation zone for the simple loop antenna are limited to 33.2 and 55.5 mm, respectively, compared to width and length of 40.5 and 65.1 mm, respectively, for the loop antenna with a passive element. Thus, the simple loop antenna would not be suitable for treating the largest uterine cavities. Similar ablation patterns were observed over $n = 3$ experimental ablations for each antenna.

To evaluate the ablation depth in different regions of the uterine cavity, the top and bottom liver pieces were sliced according to the guidelines defined in Figure 3-5. Example images of vertical and horizontal sections of the ablation zone created by the loop antenna with a passive element are shown in Figure 3-10. Deeper ablation occurs in the mid-body, whereas shallower ablation is observed on the lateral and lower regions, similar to the desired ablation profiles illustrated in Figure 3-1. Table 3-2 compares the ablation depth measured at different points as defined in Figure 3-5 for the simple loop antenna, delta loop antenna at 650 MHz and the loop antenna with a passive element. The ablation depth obtained with the simple loop antenna and the loop antenna with a

passive element is in the range of 3 – 12 mm achievable with clinically available endometrial ablation technology and follows the ablation depth pattern at different planes shown in Figure 3-1.

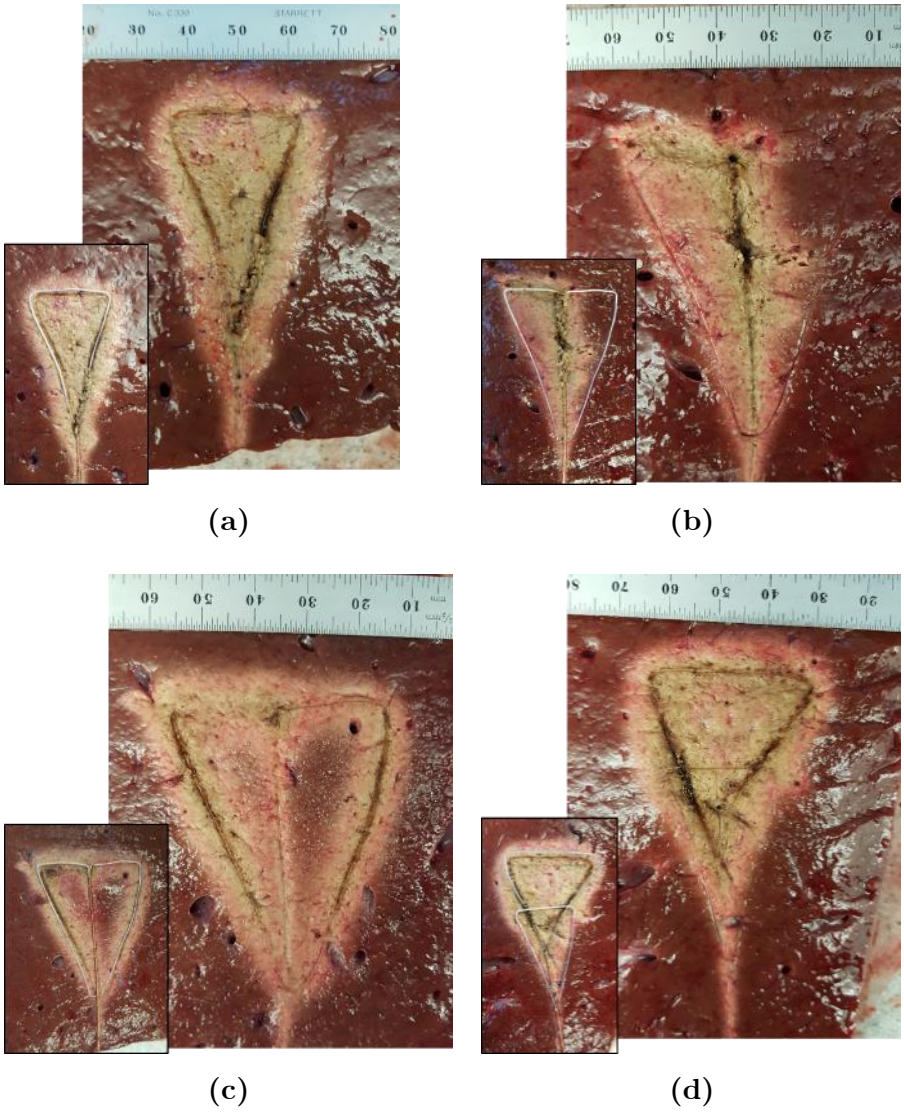

Figure 3-9: Ablation profile of a) simple loop antenna, b) delta loop antenna at 915 MHz, c) delta loop antenna at 650 MHz, and d) loop antenna with a passive element (The inset images show the position of each antenna relative to the ablation profile).

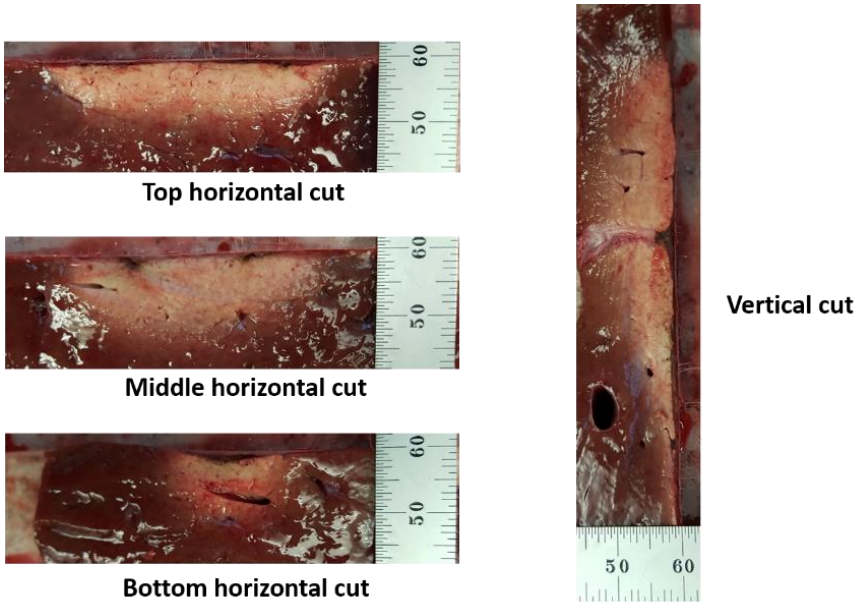

Figure 3-10: Experimental ablation zones created by the loop antenna with passive element in the horizontal and vertical planes illustrated in Figure 3-5.

Table 3-2: Ablation depth measured (n = 3) for the proposed loop antennas at points defined in Figure 3-5.

		Ablation depth [mm]									
		Vertical cut			Horizontal cut						
		Bottom	Mid	Top	Bottom	Mid			Top		
					Mid	Left	Mid	Right	Left	Mid	Right
Simple loop*	Test 1	5.3	7.2	5.9	6.6	6.9	9.5	6.9	5.4	6.5	5.3
	Test 2	4.7	8.6	6.3	6.2	4.8	7.7	6.2	4.1	5.3	5
	Test 3	4.5	8	5.5	7	6.2	9	6.5	5.5	6	5.5
	Mean ± SD	4.8±0.34	7.9±0.57	5.9±0.33	6.6±0.33	5.7±0.87	8.7±0.76	6.5±0.27	5.0±0.64	5.9±0.49	5.3±0.21
Delta loop	Test 1	3.3	3.8	6.4	3.6	5.3	3.9	6.5	5.7	6.1	6.0
	Test 2	7.7	1.0	8.2	4.1	4.9	3.6	4.7	4.9	5.4	6.9
	Test 3	6.2	3.8	8.6	7.5	6.9	3.4	5.9	6.7	7.9	8.1
	Mean ± SD	5.7±1.84	2.8±1.31	7.8±0.95	5.0±1.74	5.7±0.86	3.6±0.19	5.7±0.72	5.8±0.73	6.5±1.05	7.0±0.85
Loop with passive	Test 1	7.1	8.8	7.0	6.7	5.2	8.0	5.4	5.0	7.5	6.6
	Test 2	7.2	9.3	7.7	7.5	6.1	10.3	6.0	6.4	8.7	6.3
	Test 3	7.1	10.9	7.4	8.1	6.0	10.5	6.9	5.6	8.8	5.0
	Mean ± SD	7.1±0.04	9.6±0.89	7.3±0.30	7.5±0.59	5.8±0.41	9.6±1.10	6.1±0.60	5.7±0.61	8.3±0.60	5.9±0.68

* Data from [23].

3.3.3 Radiating and passive loop profiles for ablating cavities of varying size

Combination of the proposed radiating loop antenna with a passive element provides a degree of freedom to shape the ablation zone for varying cavity sizes by appropriately sizing, shaping, and positioning the passive element and radiating loop. Figure 3-8 illustrates the suitability of using the loop antenna coupled with a passive element for ablating large uterine cavities. In order to assess the versatility of the proposed loop antenna coupled with a passive element for global ablation of cavities of small cavity sizes, we investigated applicators with the geometries shown in Figure 3-11(a) and (b).

For a small cavity (perimeter = 109 mm), we investigated a loop antenna with shape modified to fit within the cavity, and without a passive element (see Figure 3-11(a)). For an intermediate-sized cavity (perimeter = 155 mm), we investigated a simple loop antenna with a passive element shaped as in Figure 3-11(b). Simulated temperature profiles for both applicators indicate conformal ablation over the corresponding uterine cavity. These simulations suggest that the combination of the radiating loop antenna with the passive element will enable adequate ablation of uterine targets of perimeter 109 – 182.5 mm. In [140], a passive loop element was employed to shape the electric field pattern radiated by a monopole antenna. Compared to the approach in [140], the use of a passive element with a loop antenna presented in this study offers the advantage of the loop antenna's return loss being minimally affected by the presence and positioning of the

passive element. For example, Figure 3-7 shows that the broadband RL profile of the loop antenna is not considerably affected by the inclusion of the passive loop element. This may be important for applications within the uterine cavity where deployment of the active antenna and passive elements may not be precisely controlled.

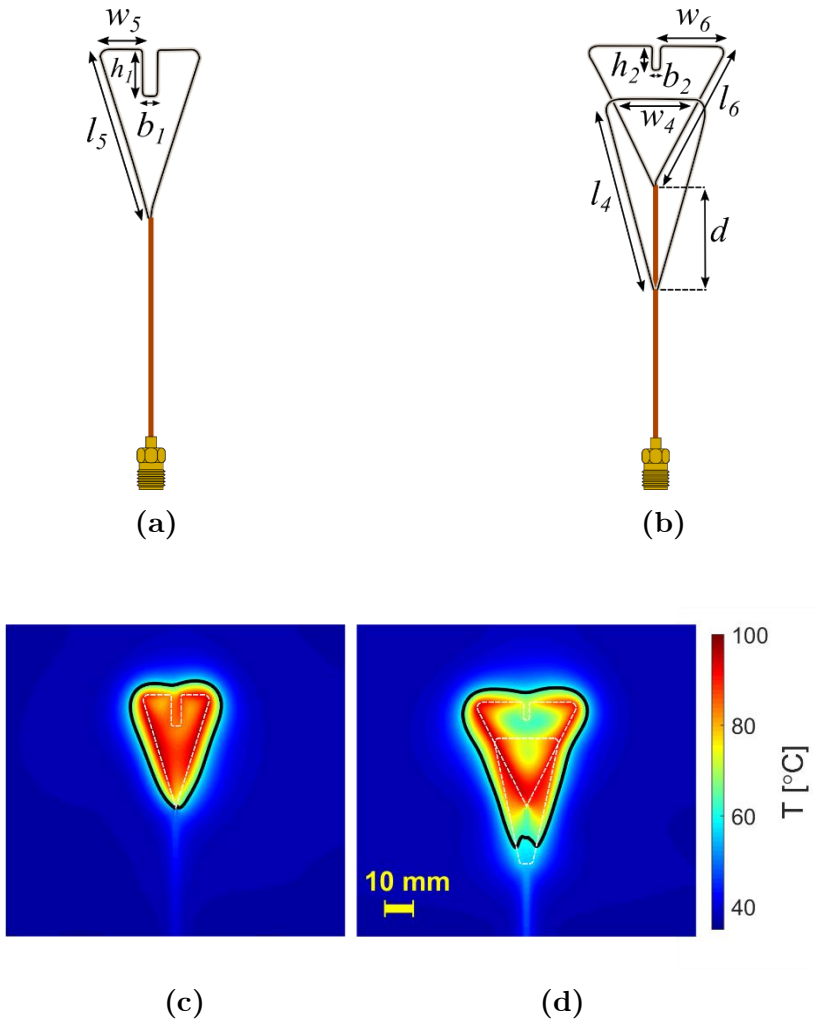

Figure 3-11: a) Reshaped simple loop antenna (l_5 = 40 mm, w_5 = 10 mm, h_1 = 10 mm, b_1 = 5 mm) conformal to the smallest cavity size, b) reshaped loop antenna with passive element (l_4 = 42 mm, w_4 = 25 mm, l_6 = 39 mm, w_6 = 17 mm, h_2 = 5 mm, b_2 = 3 mm, d = 25) conformal to the medium size cavity. Simulated temperature profiles and overlaid thermal damage contour without blood perfusion (black solid line, Ω = 1) of the (c) reshaped simple loop antenna, and d) reshaped loop antenna with passive element, for input power of 60 W and ablation duration of 150 s.

A limitation of this study is that experiments considered *ex vivo* tissue and did not account for the impact of blood perfusion. We note that heat sink due to blood flow may be compensated by adjusting applied power levels and duration of ablation. The proposed design is capable of creating shallow depth ablation zone in which the depth is tapered and not uniform in the sagittal plane, as is desired for the endometrial ablation application. However, for applications requiring uniform ablation depth, the shape of the loop may need to be modified. Furthermore, clinical use of the proposed design in practice will require a deployable device inserted to the uterine cavity in a retracted state with minimal dilation of the cervix. In this study, we employed coaxial cables formed into the desired loop shapes. Nitinol, a shape memory alloy that has been widely used in medical devices [141], including RF ablation technology [142], may be suitable for implementing deployable designs. Other studies have also demonstrated the suitability of using Nitinol for creating deployable/configurable antennas [107]. Other approaches to realize a deployable applicator include the use of compression spring properties. Further studies investigating practical approaches for realizing deployable antenna designs are warranted.

This study illustrates the technical feasibility of performing microwave global endometrial ablation, similar to other energy modalities such as thermal balloon, circulated hot water and RF ablation. The microwave applicator's overall diameter, which includes components for circulating cooling water along the feeding coaxial line, is 2.5 mm while the reported range for cervical dilation used for other endometrial techniques is 5-8

mm. Thus, using smaller microwave GEA devices may reduce the burden for cervical dilation, thereby technically simplifying the procedure, and potentially reduce intra-procedural pain. The microwave GEA applicators presented here may be used to treat uterine cavity sizes ranging from 6 to 10 cm (from external os to fundus) in less than 3 minutes while the reported uterine cavity sizes and treatment time for other global modalities are 10.5 cm or less and 1.5-10 minutes, respectively [115]. Compared to other modalities, microwave GEA does not need direct contact between the antenna and the uterine tissue in order to achieve effective ablation and existence of small air pockets in the uterine cavity does not change the energy transfer from the antenna to the tissue significantly.

3.4 Conclusion

In this paper, a microwave loop antenna-based applicator was investigated for treatment of heavy menstrual bleeding. Simulated and experimentally measured RL and ablation profiles were in good agreement. The proposed loop antennas created tapered ablation depths required for GEA application. Furthermore, experimental measurements showed that addition of a passive loop element provides a means for increasing the range of uterine cavity sizes a loop antenna can adequately ablate. Simulations demonstrated the ability to create conformal endometrial ablation zones in $4 - 6.5$ cm uterine cavities through appropriate shaping of the loop antenna and passive element. The modeling and

design procedures described in this paper can be utilized to design microwave ablation antennas for targets with a wide planar profile but requiring limited ablation depth.

4 Monitoring Transient Evolution of Planar Ablation Zones Using the Broadband Antenna Reflection Coefficient

4.1 Introduction

The most common approach for characterization of MWA applicators is to determine the ablation size as a function of input power and ablation duration in *ex vivo* bovine liver tissue. The tissue sample is sectioned after the ablation and the ablation zone dimensions are measured from the visible extent of discolored tissue. The measured dimensions would be tabulated as part of regulatory submissions and in the applicator guide manual for physicians' reference. During a clinical procedure, the physician has to choose the applied input power and ablation duration based on the anatomy of the patient being treated. However, the ablation size charts provided by the applicator manufacturers have some limitations. The target tissue being treated may have considerably different biophysical properties when compared to bovine liver, may have heterogeneous texture and blood perfusion is present *in vivo*. Consequently, selection of applied energy delivery parameters that result in complete destruction of the target is challenging. Imaging

techniques such as X-ray CT, US and MRI are the tools physicians employ for placement of the applicator in the target and monitoring the ablation procedure [143]. In the ablation procedure, an initial image is acquired for guiding the applicator to the target, after which ablative power is applied. After the ablation, contrast-enhanced imaging with X–ray CT or ultrasound [144], [145] are utilized for verifying the ablation profile. By developing MR-compatible instruments, it is also viable to perform MR-guided ablations [146]. However, there are currently no non-imaging-based technique available for real-time monitoring of microwave ablation zone growth in the clinical setting. This means there is limited information available to the physician during the procedure in order to apply corrective measures during the ablation procedure.

Studies have shown that dielectric properties of tissue relative permittivity and effective conductivity, experience drastic changes at ablative temperatures due to water loss and protein denaturation [136]. Temperature-dependent dielectric properties changes of tissue can be captured by the antenna reflection coefficient during the ablation. Reflection coefficient is a performance parameter of an antenna that determines the amount of electromagnetic power reflected back to the generator due to the impedance mismatch between the antenna embedded within tissue and the feeding transmission line. This parameter is dependent on the antenna structure and dielectric properties of the surrounding tissue media. In an ablation procedure, the antenna structure is fixed. Consequently, the changes in the antenna parameters corresponds only to changes of the

tissue dielectric properties, as it is heated and desiccated. We exploited these changes in dielectric properties of tissue at ablative temperatures as a means of determining the ablation endpoint during MW global endometrial ablation.

4.2 Methods

A water-cooled simple loop antenna, designed for global endometrial ablation as described in chapter 3 [23], was utilized to investigate the feasibility of using antenna reflection coefficient (S_{11}) as a real-time ablation monitoring feedback in an ablation procedure. Figure 4-1 illustrates a photo of the loop antenna. Basic components of an ablation system are the microwave generator and the antenna. In order to measure the antenna S_{11} before and after the ablations, a high power cold switch (Teledyne CCR-33S_CR-33S) was incorporated to the setup. The switch toggles the antenna input between the microwave generator and a vector network analyzer (VNA) while protecting the VNA front-end. Figure 4-2 illustrates the setup.

The microwave generator was set to operate at 1 GHz. Water flow was at 165 mL/min. The antenna was sandwiched between two pieces of porcine muscle. Temperature of the *ex vivo* porcine muscle tissue was raised to ~35 °C before each experiment. Experiments were performed for ablation durations of 70, 150 and 240 s with a fixed input power of 60 W. Each combination was repeated two times.

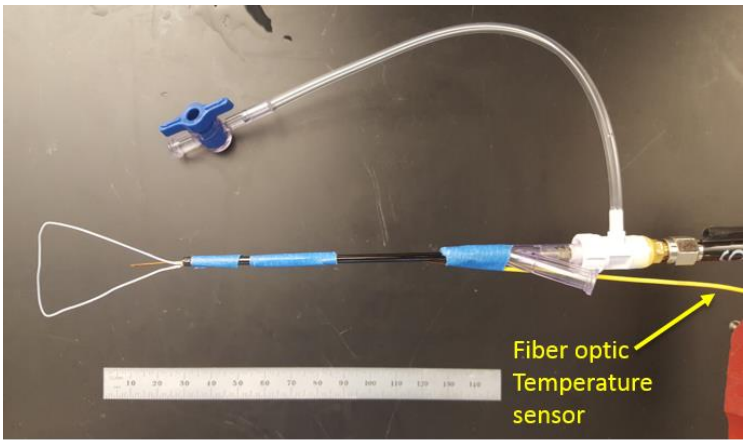

Figure 4-1: Water-cooled antenna with a fiber optic temperature sensor for global endometrial ablation.

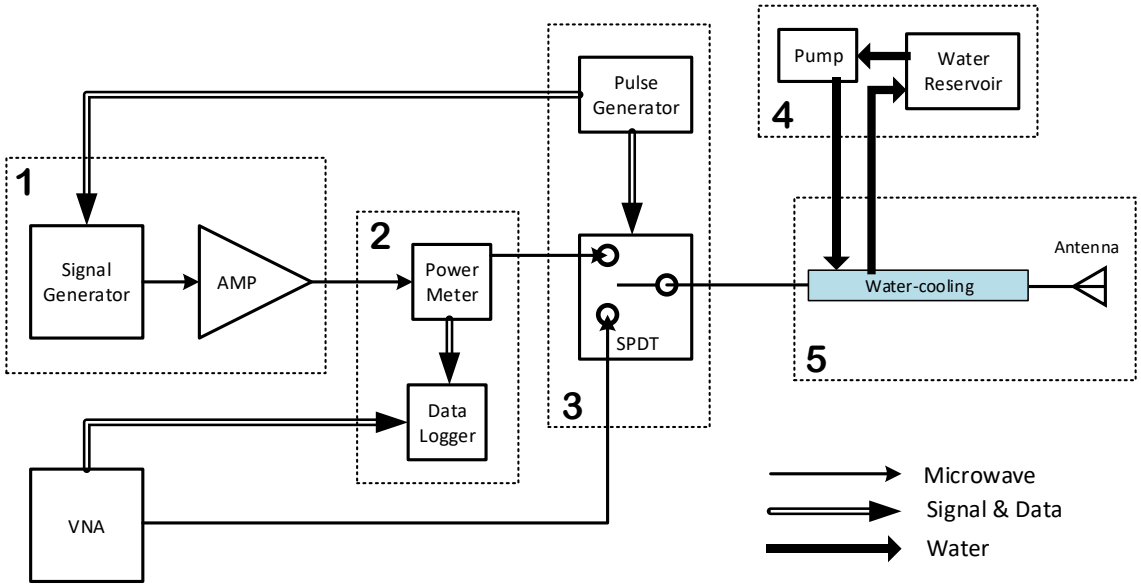

Figure 4-2: Block diagram of the setup for S_{11} measurement during the ablation.

4.3 Results

Measured temperature inside the loop for each experiment is shown in Figure 4-3. The temperature profiles include both heating and cooling intervals. Example photos of the ablation pattern of the antenna for durations of 70, 150 and 240 seconds are shown in Figure 4-4. Measured S_{11} of the loop antenna in the frequency range of 850 to 1050 MHz

before and after each ablation is plotted in Figure 4-5. Shift of the loop antenna resonant frequency before and after each ablation is summarized in Table 4-1.

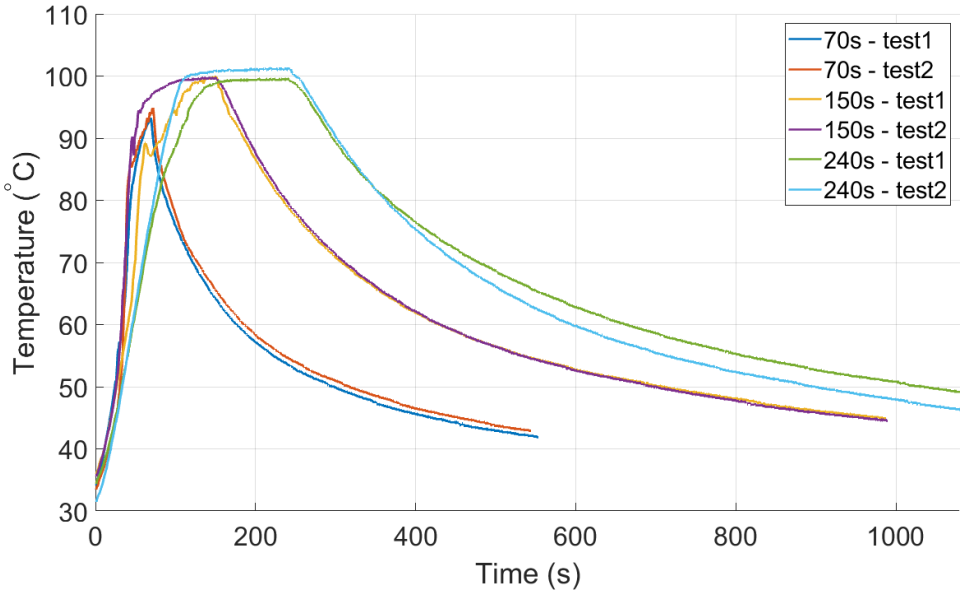

Figure 4-3: Tissue temperature change during the ablation experiment.

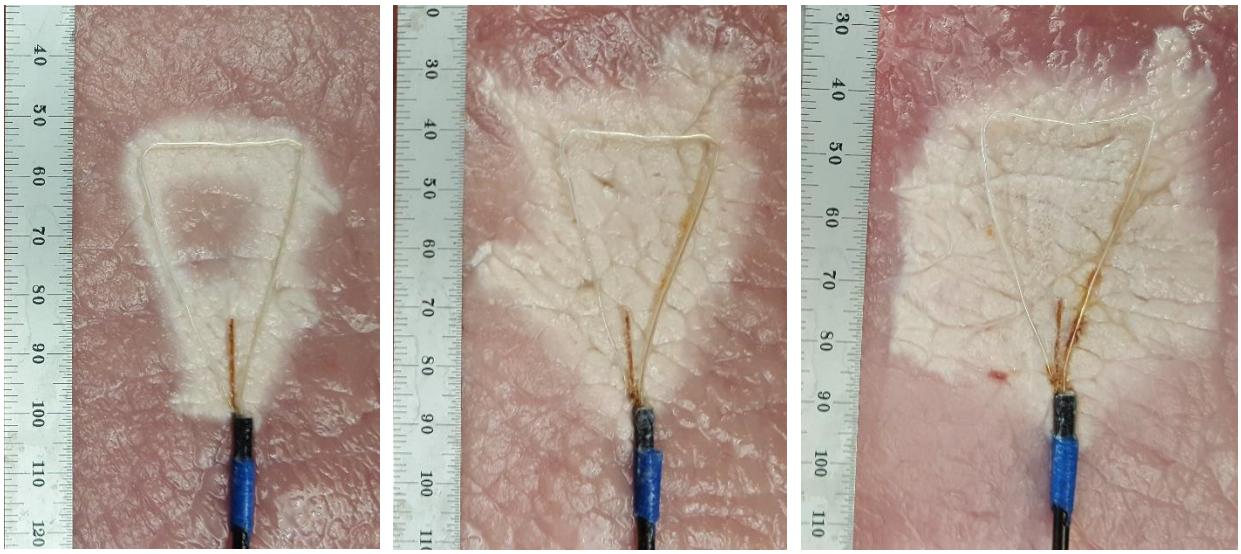

(a) (b) (c)

Figure 4-4: Example photos of the ablations for fixed input power of 60 s and duration of a) 70 s, b) 150 s, and c) 240 s.

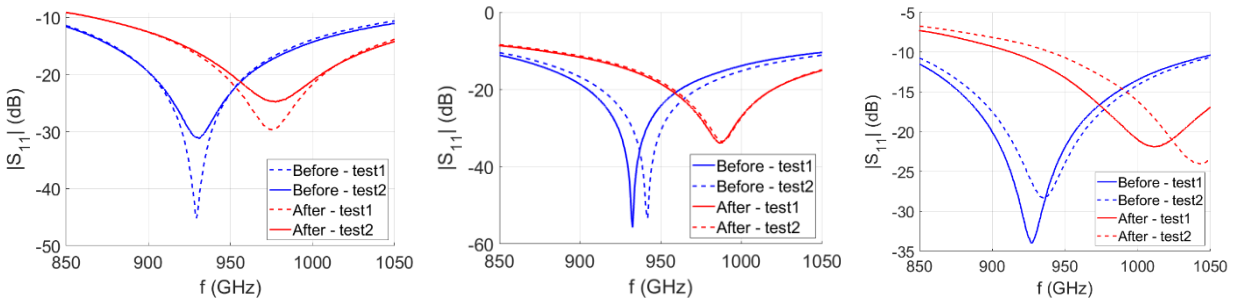

(a) 70 s **(b) 150 s** **(c) 240 s**

Figure 4-5: Comparison of the antenna S11 before and after ablation for fixed power of 60 W and different durations.

Table 4-1: Resonant frequency of the antenna before and after ablation

	f_1 (MHz) = Resonant freq. before ablation	f_2 (MHz) = Resonant freq. after ablation	$\Delta f = f_2 - f_1$
70 s – Test 1	930	977	47
70 s – Test 2	930	975	45
150 s – Test 1	932	987	55
150 s – Test 2	938	989	51
240 s – Test 1	927	1011	84
240 s – Test 2	935	1043	108

4.4 Discussion

We selected the fixed input power of 60 W and ablation durations of 70, 150 and 240 s in order to emulate cases of under-ablation, adequate ablation and over-ablation, respectively. Ablation photos in Figure 4-4 indicate that for the case of 70 s ablation, the tissue is under-ablated while it is over-ablated for the case of 240 s. In order to relate the ablation progress to the measured broadband S_{11} of the antenna, we investigated how the antenna resonant frequency changes. Figure 4-5 shows how much the resonant frequency shifts to higher frequencies in the course of ablation. As summarized in Table 4-1, for

longer ablations the difference between the antenna resonant frequency before ablation and that of after ablation is larger.

In order to make use of the resonant frequency shift as an ablation-monitoring signal, two modes are defined for the ablation setup shown in Figure 4-2: treatment and assessment modes. In the treatment mode, the switch connects the antenna to the microwave generator. The generator energizes the antenna at the operation frequency to deliver power to the tissue and heat it to lethal temperatures. In the assessment mode, the switch connects the antenna to the VNA. The VNA transmits a range of frequencies at low power and measures the reflected power in order to calculate the antenna S_{11}. The measurement interval (as short as 5 seconds) is not comparable to treatment intervals and does not compromise the ablation.

In an ablation procedure, when the antenna is positioned in the target site, the switch puts the antenna in assessment mode to measure the antenna S_{11} and finds the resonant frequency. This would be used as a reference for the subsequent measurements. During the course of the ablation, the antenna is set to assessment mode to measure S_{11}. The measured signal is compared to the reference signal and determines when to stop the ablation.

One of the limitations of this feedback signal is that it may only provide a complementary means for monitoring the ablation progress. The physician may not be able to definitely determine when to stop the ablation solely based this signal since there

are many other variables involved that may impact the antenna reflection coefficient and the ablation zone extent, such as tissue variability.

4.5 Conclusion

This study investigated the feasibility of using broadband reflection coefficient of ablation antennas as a feedback signal for monitoring the ablation progress over the ablation procedure. As heat changes the tissue state from unablated to mildly ablated and completely ablated, the tissue dielectric properties change. Experimental ablations using a loop antenna indicated that dielectric properties change translate to change of resonant frequency of the antenna. This parameter may provide physicians with an extra layer of information in addition to post-procedural imaging.

5 Microwave Antennas for Thermal Ablation of Benign Adrenal Adenomas[3]

5.1 Introduction

Primary aldosteronism involves the excessive secretion of aldosterone from the adrenal gland, and is responsible for up to 11.2% of all cases of hypertension [147]. When this excess of aldosterone is attributable to an adenoma (a benign adrenal gland tumor), the condition is referred to as Conn's syndrome. The negative effects of chronic hypertension are widely known and include coronary artery disease, congestive heart failure and cardiac arrhythmias [148], [149]. Currently, a patient with Conn's syndrome must undergo adrenalectomy or receive intensive medical management with significant side-effects [149]. While adrenalectomy is an effective means of definitive therapy, it is only indicated for unilateral disease. Bilateral cases are typically treated with

[3] This chapter has been published as: H. Fallahi, D. Clausing, A. Shahzad, M. O'Halloran, M. C. Dennedy, and P. Prakash, "Microwave antennas for thermal ablation of benign adrenal adenomas," Biomed. Phys. Eng. Express, vol. 5, no. 2, p. 025044, 2019. (DOI: 10.1088/2057-1976/ab068b)

mineralcorticoid receptor antagonists (MRA), which are associated with side effects like gynaccomastia and sexual dysfunction in men, while causing menstrual irregularities and conferring risks for teratogenicity in women of reproductive age [150].

Recently, there has been growing interest in the potential of image-guided thermal blation for minimally-invasive treatment of adrenal adenomas. Thermal ablation is an established treatment modality that uses high temperatures ($> \tilde{}55$ °C) to destroy malignant tumors in the liver, kidney, prostate, and the lungs. Systems employing a variety of energy modalities have been developed for thermal ablation, including radiofrequency current, laser, microwave, and ultrasound [151], [152]. As a result, ablation research and clinical applications have been primarily focused on achieving large ablation zones that destroy the tumor, as well as a healthy margin around the tumor to reduce the risk of recurrence. The difference between using ablation for cancerous lesions and a Conn's adenoma is twofold: Firstly, in Conn's syndrome, a primary goal is to preserve as much healthy functional tissue as possible rather than continuing ablation until marginal ablation of healthy tissue is established. While, complete ablation of the adenoma is necessary for clinical success, large volume marginal ablation is unnecessary because these tumors are benign. Secondly, several studies indicate that the average adrenal adenoma causing Conn's syndrome is around $5 - 20$ mm wide, which is much smaller than the majority of the malignant tumors in the liver, kidney, and lungs [153]. These two major

distinctions made it clear that the technical requirements for an adrenal ablation device was very different from those used routinely for treating tumors in other organs.

We propose the use of microwave ablation (MWA) for minimally-invasive treatment of adrenal adenomas. Thermal ablation systems for treatment of the adrenal gland require antenna designs optimized for the creation of small, spherical ablation zones. Since it is technically challenging to accurately position the ablation device in adenomas with diameter < 10 mm, we anticipate candidate patients for this technology will be those with adenomas with diameter ranging between $10 - 20$ mm. Thus, we restricted our MWA antenna design to adenomas with diameter ranging between 10 to 20 mm. Devices affording control of the axial and radial extents of heating will ensure conformal ablation of the targeted adenoma, while maximally preserving the adjacent adrenal tissue to maintain adrenal function. The majority of MWA systems in clinical use have been optimized for creation of large, spherical ablation zones in vascular organs such as the liver, and operate at 915 MHz or 2.45 GHz, both of which are frequencies allocated for industrial, scientific, and medical (ISM) use [154]–[156]. Compared to MWA systems operating at 915 MHz, systems operating at 2.45 GHz afford more rapid heating to higher tissue temperatures, as well as shorter antenna lengths, which enable creation of short ablation zones [154]. Systems operating at higher frequencies have also been investigated, with studies indicating that ablation zones of comparable volume to ~2 GHz systems are achievable with ablation systems operating at frequencies >10 GHz [55], [60], [157].

The radial depth, and thus the width, of the ablation zone may be controlled by adjusting applied power levels and duration of ablation. However, controlling length of the ablation zone created by microwave devices is more challenging, as detailed below. A number of studies have investigated methods to restrict the axial length of large volume ablation zones, which is typically not collimated to the length of the radiating element due to the use of unbalanced antennas, resulting in currents flowing along the outer surface of the feedline cable [46]. A frequently used technique is the use of antenna sleeves or chokes to restrict currents on the outer surface of the feedline cable [45], [83], [158]. Luyen *et al.* presented a balun-free helical antenna design that operates at the second resonant frequency of the antenna and employs impedance matching elements [47]. Due to the attenuation within thin, coaxial cables, active cooling strategies are often employed to limit passive heating of tissue adjacent to the feedline cable [67]. While the above approaches restrict undesirable heating beyond the active length of the antenna, the minimal length of the ablation zone is limited by the active length of the radiating antenna, which in turn is determined by the wavelength at the system operating frequency. Approaches for reducing minimum length of the ablation zone include: dielectric loading of the antenna element to reduce the effective wavelength [84]; use of helical or other coiled antenna elements rather than linear monopoles/dipoles [47]; and designing MWA systems to operate at higher frequencies [63]. Existing microwave ablation devices have been clinically applied for treating malignant tumors in the adrenal gland; however, the targeted tumors have typically been large (2.1 – 6.1 cm) [159]–[162].

Technological requirements and feasibility of microwave ablation of adrenal masses were investigated in [27], [163]. For actively cooled applicators, adjustment of coolant flow parameters as well as coolant temperature may provide an additional means for adjusting ablation zone length. There is a lack of studies investigating practical techniques for reducing the length of MWA zones to the range of ~10 – 20 mm.

Some prior studies have parametrically studied the efficacy of radiofrequency ablation (RFA) for clinical practice [164], [165]. Furthermore, it has been shown that RFA leads to lower post-procedural pain and shorter operative times than laparoscopic adrenalectomy [153], [166]. While these studies demonstrated the technical feasibility of using thermal ablation for targeting adrenal tissue, they employed RFA devices suitable for large-volume tumor ablation. Consequently, these approaches were not well suited restricting thermal damage to the targeted adenomas, resulted in ablation of the entire adrenal gland, and thus would not be suited for treating patients with bilateral disease.

The objective of this study was to investigate methods for creating short, spherical ablation zones, 0.5 – 4 cm^3 (diameter: 10 – 20 mm) using linear MWA antennas to treat benign adrenal adenomas. We hypothesized that water-cooled monopole antenna designs operating at 2.45 GHz and 5.8 GHz would afford the creation of short, spherical ablation zones ranging in diameter from 10 – 20 mm. Here, we investigated the ability to control ablation zone dimensions through adjustments of antenna operating frequency, applied power, ablation duration, and coolant temperature. Multiphysics computational models

and experiments in *ex vivo* liver and adrenal gland tissues were employed to assess the impact of these parameters on ablation outcome. The key contribution of this work is demonstration of feasibility of using microwave ablation for creating localized ablation zones of diameter 10 – 20 mm with application to treatment of unilateral and bilateral adrenal adenomas.

5.2 Methods

Two approaches for creating ablation zones of length in the range 10 – 20 mm were investigated. The first approach employs water-cooled antenna designs operating at 2.45 GHz. Since water is a good microwave absorber (effective conductivity, $\sigma = 1.36$ S/m and attenuation coefficient, $\alpha = 28.95$ Npm^{-1} at 2.45 GHz), many MWA antennas employ water-cooling that terminates water flow proximal to the antenna radiating element [66], [84]. Thus, the water serves to remove heat dissipated within the lossy cables, without being exposed to microwaves radiating from the antenna element, thereby limiting microwave absorption within the applicator. Here, we exploit the high dielectric constant of water at 2.45 GHz (ϵ_r ~78) that serves to reduce the electromagnetic wavelength and thus the physical length of the antenna, compared to low permittivity materials such as plastics and ceramics commonly used in ablation devices. The second approach employs a water-cooled antenna designed to operate at 5.8 GHz. The higher frequency yields a shorter electromagnetic wavelength, and thus reduces the physical length of the antenna;

for example, the wavelength in adrenal tissue at 5.8 GHz is 6.8 mm compared to 16 mm at 2.45 GHz. 5.8 GHz is selected because it is the center of the next frequency band above 2.45 GHz approved for ISM use [167]. To illustrate these concepts for controlling ablation zone size and shape, we designed water-loaded coaxial monopole antennas at 2.45 GHz and 5.8 GHz; these antennas can be readily fabricated and provide a practical means for tissue ablation.

5.2.1 Water-cooled antenna designs

We consider water-cooled coaxial monopole antennas tuned to 2.45 GHz and 5.8 GHz. The antennas consist of UT-34 coaxial cable with a length l_{m} at the distal end of the outer conductor and dielectric stripped off. The cable and radiating tip are inserted within a concentric set of tubes through which water is circulated in a closed flow circuit. Water, which has a high dielectric constant (ϵ_{r} ~78 at 2.45 GHz; ϵ_{r} ~72 at 5.8 GHz), shrinks the effective wavelength, thereby reducing the physical length of the resonant antenna, as well as providing a means to maintain low temperatures within the applicator shaft.

5.2.2 Computational models – SAR and thermal ablation zone analysis (impact of water cooling)

We employed finite element method (FEM) simulations, implemented using COMSOL Multiphysics v5.3, to model electromagnetic power absorption and heat transfer

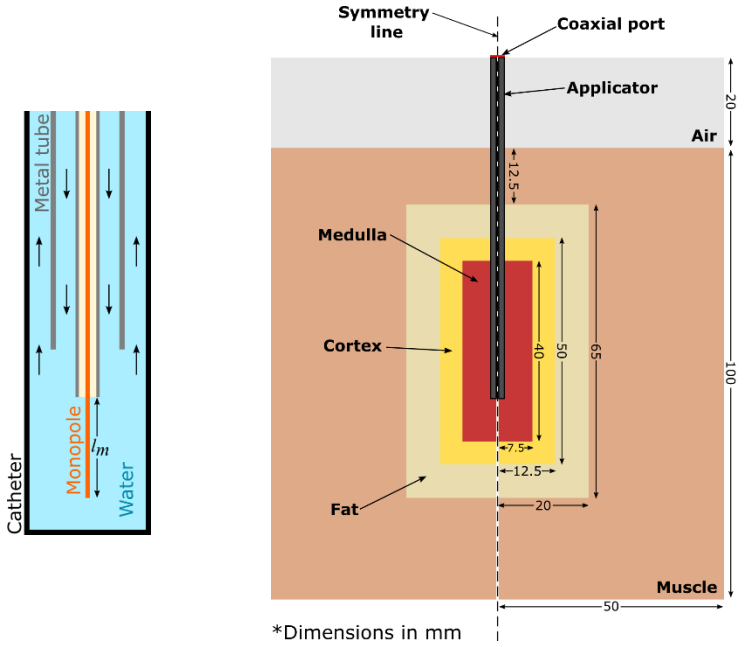

(a) (b)

Figure 5-1: Illustration of the a) water-loaded monopole antenna and b) geometry of the multi-layered tissue model used in simulations.

during microwave ablation with the candidate antenna designs. Due to the cylindrically symmetric geometry of the applicator, the 3D geometry can be modeled with a 2D axially symmetric model. The model geometry illustrated in Figure 5-1 consists of the applicator inserted within the adrenal gland, consisting of four layers of tissue (medulla, cortex, fat, and muscle), as described in [168].

We approximated the surrounding tissues as a layer of muscle. The solver computes the electric fields in the model by solving the Helmholtz wave equation:

$$\nabla^2 \mathbf{E} - k_0^2 \left(\epsilon_r - \frac{j\sigma}{\omega \epsilon_0}\right) \mathbf{E} = 0 \qquad (1)$$

where $\mathbf{E}\,[\mathrm{V} \cdot \mathrm{m}^{-1}]$ is the electric field, k_0 is the free space wave-number, ϵ_r is the relative permittivity, $\sigma\,[\mathrm{S} \cdot \mathrm{m}^{-1}]$ is the effective electrical conductivity, $\omega\,[\mathrm{rads} \cdot \mathrm{s}^{-1}]$ is the angular

frequency, and ϵ_0 $[\mathrm{F} \cdot \mathrm{m}^{-1}]$ is the permittivity of free space. Microwave power was applied to the port defined on the proximal end of the applicator as illustrated in Figure 5-1. A first order scattering boundary condition was used on the external surfaces of the model as:

$$\mathbf{n} \times (\nabla \times \mathbf{E}) - jk\mathbf{n} \times (\mathbf{E} \times \mathbf{n}) = 0 \tag{2}$$

where $\mathbf{n}$ is normal vector to the boundary. Time-averaged electromagnetic power losses are calculated from the computed electric field using

$$Q_{em} = \frac{1}{2}\sigma|\mathbf{E}|^2 \tag{3}$$

Electromagnetic power loss is coupled to the heat equation in order to compute the temperature profile inside the tissue:

$$\rho c_l \frac{\partial T}{\partial t} = \nabla \cdot (k \cdot \nabla T) + Q_{em} \tag{4}$$

where T $[K]$ is temperature, ρ $[\mathrm{kg} \cdot \mathrm{m}^{-3}]$ is the density of the tissue, c_l $[J \cdot kg^{-1} \cdot K^{-1}]$ is the heat capacity at constant pressure, and k $[W \cdot m^{-1} \cdot K^{-1}]$ is the thermal conductivity. The initial temperature of the tissues was set to $37\ ^{\circ}\mathrm{C}$ and heat flux boundary conditions were defined on the applicator and tissue boundaries as:

$$Q_0 = h(T_{ext} - T) \tag{5}$$

where Q_0 is the transferred heat, T_{ext} is the external temperature, and h is the convective heat transfer coefficient. A value of $h = 10\ W \cdot m^{-2} \cdot K^{-1}$ is employed on the external tissue surfaces. A value of $h = 1000\ W \cdot m^{-2} \cdot K^{-1}$ is employed on the outer surface of the

applicator to model convective heat transfer due to circulating water in the applicator similar to [169]. Table 5-1 and Table 5-2 summarize the nominal thermal properties of adrenal gland, fat, muscle and liver tissue from [170], and measured cortex and medulla electrical permittivity and conductivity values [171] incorporated in the simulations. In this study, we modeled tissue dielectric properties as being constant across all temperatures. Although it is recognized that dielectric properties of liver tissue are temperature dependent [136], [172], [173], in this study, we used static dielectric properties in our simulations since the temperature dependency of liver tissue dielectric properties at ablative temperatures (i.e. T $>$ 80 °C) has only been reported at 2.45 GHz; liver temperature-dependent dielectric property data are not available at 5.8 GHz. Further, there are no published studies reporting the temperature dependency of dielectric properties of adrenal tissue. Despite these limitations, simulations still provide a qualitative understanding of the effects of changing system operating frequency, applied power, ablation duration, and coolant temperature on ablation zone size and shape, to guide device design and experimental evaluation [60], [63], [101]. Temperature-dependent changes in heat capacity and thermal conductivity, as described in [137], were used in the simulations.

Table 5-1: Nominal thermal properties of tissue.

Tissue	c_l [J·kg^{-1}·K^{-1}]	k [W·m^{-1}·K^{-1}]	ρ [kg·m^{-3}]
Adrenal cortex	3513	0.44	1028
Adrenal medulla	3513	0.44	1028
Fat	2348	0.21	911
Muscle	3421	0.49	1090
Liver	3540	0.52	1079

Table 5-2: Dielectric properties of tissue at 2.45 GHz and 5.8 GHz employed in simulations.

	2.45 [GHz]		5.8 [GHz]	
	ε_r	σ [S·m^{-1}]	ε_r	σ [S·m^{-1}]
Cortex	48.8	1.8	42.88	5.28
Medulla	54.7	1.9	48.96	5.78
Fat	10.8	0.27	9.86	0.83
Muscle	52.7	1.74	48.50	4.96
Liver	43.0	1.69	38.10	4.64

In each simulation, thermal damage induced by microwave radiation in tissue was computed as a function of time and temperature by using an Arrhenius model [41] to obtain the ablation profile

$$\Omega(\tau) = \int_0^\tau A \exp\left(-\frac{E_a}{RT(t)}\right) dt \qquad (6)$$

where $\Omega(\tau)$ is a dimensionless damage parameter, A is frequency factor (5.51×10^{41} s^{-1}), E_a is energy barrier (2.769×10^5 J·mol^{-1}), R is gas constant (8.3143 $J \cdot mol^{-1} \cdot {}^\circ C^{-1}$), $T(t)$ stands for the time development of the spatial temperature profile, and τ is the total time for which the thermal damage in the tissue was accumulated. These values of E_a and A were selected to model tissue discoloration following heating, allowing for comparison with experimental ablation zones [138]. A damage contour with a value of $\Omega = 1$ (corresponding to 63% of the thermal damage process being complete) was also overlaid on the temperature profile as a threshold for assessing the extent of the ablation zone. A non-uniform mesh was employed, with finest meshing at the antenna feed (maximum element size = 0.015 mm) and coarsest mesh in regions further away from the radiating

element (maximum element size = 4.45 mm). The number of degrees of freedom in each model was 212,000 on average.

The computational models were used to determine the monopole length, l_m, that yielded the lowest antenna reflection coefficient at the desired operating frequency. Nominally, the length is expected to be $l_{\mathrm{m}} = \tilde{\lambda}/4$ at the operating frequency for a monopole antenna. At each frequency of interest, we iteratively adjusted l_m in simulations to identify the frequency at which reflected power is minimized, indicating the best impedance match to the feeding transmission line.

5.2.3 Experimental platform – hardware for evaluating ablation zones

Antennas were fabricated from UT-34 semi-rigid coaxial cable inserted within a stainless-steel tube (1.82 mm O.D. and 1.37 mm I.D.), and the entire assembly subsequently inserted within a thin-walled PEEK tube (2.46 mm O.D.). The broadband reflection coefficients of the fabricated antennas were measured with a vector network analyzer (HP 8753D) to confirm adequate impedance matching at the desired operating frequency.

Following confirmation of impedance match ($S_{11} <$ -10 dB), ablation experiments were then performed in freshly excised *ex vivo* bovine liver and adrenal gland tissues. We selected fresh *ex vivo* bovine liver tissue for experimental evaluations since it is a well-established tissue model for benchtop evaluation of novel thermal ablation technologies [127]; unlike the adrenal gland, it would not require embedding within a larger lossy

medium to simulate the body [27]; and the contrast in color of ablated tissue vs. unablated tissue is readily observed in liver, but not clear in adrenal gland tissue.

Freshly excised bovine liver and adrenal gland tissues were obtained from a local meat locker and transported to the lab within sealed plastic bags placed on ice. At the lab, the liver was sectioned into ~8 cm × 8 cm × 6 cm blocks, placed within thin-walled plastic bags that were sealed and immersed within a ~35-37 °C water bath. Once samples were warmed to ~37 °C, they were removed from the bath. The applicator was introduced into the liver and positioned such that the applicator tip was 60 mm below the liver surface. For adrenal gland ablations, the glands were similarly warmed up and they were sandwiched between porcine muscle with temperature of ~35-37 °C during ablation. Insertion depth of the microwave applicator in the adrenal gland case was from 20 to 25 mm. An HP 83752B signal generator provided a continuous wave sinusoidal signal at the frequency of interest. Solid-state microwave amplifiers were then used to amplify the signal to 30 and 50 W. During ablations, a microwave power meter (Bird 7022, statistical power sensor) was connected in line with the applicator to monitor forward and reflected power for all applications. Chilled water (~10 °C) was circulated through the applicator via a peristaltic pump (Cole Parmer 7554–90, Vernon Hills, IL, USA) at a rate of 80 ml/min.

5.2.4 Experimental protocol

We employed experiments to assess ablation zone size/shape when delivering ablation with the following parameters:

- Input power: 30 and 40 W
- Frequency: 2.45 GHz and 5.8 GHz
- Ablation duration: 30, 60 and 90 s
- Coolant water temperature: 10 °C

Each (power, frequency, duration) combination was repeated five times ($n = 5$). In a second set of experiments, the effect of coolant water temperatures was investigated ($T_{coolant}$ = 20 and 30 °C) when frequency = 5.8 GHz considering P_{in} = 30 W, and ablation duration of 90 s ($n = 3$). Following each experimental ablation, the tissue sample was sliced along the applicator axis, and the ablation zone length and width were measured using a ruler. The sphericity of the ablation zone shape was assessed using the axial ratio, defined as the ratio of the ablation zone width to the ablation zone length. Finally, we analyzed the measured length and width of ablations by using multi-way ANOVA. In a 3-way ANOVA, the main effects (frequency, power, time) and interaction terms (frequency*power, power*time, time*frequency) were studied.

After ensuring that it is feasible to use microwave ablation for creation of small ablation zones, two sets of ablation experiments (f = 2.45 GHz, P_{in} = 50 W, t = 180 s, $T_{coolant}$ = 10°C) and (f = 5.8 GHz, Pin = 40 W, t = 90 s, Tcoolant = 30 °C) were performed three times (n = 3) for each combination in bovine adrenal gland.

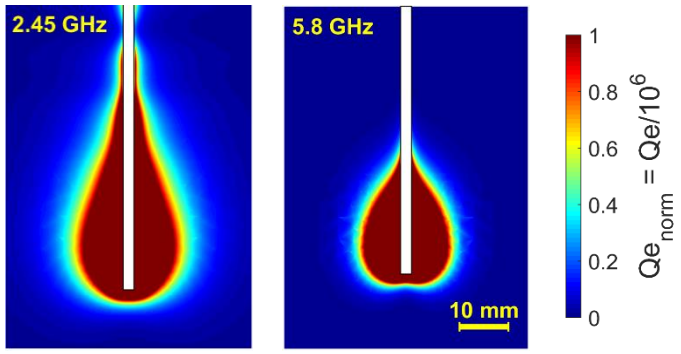

(a) (b)

Figure 5-2: Comparison of simulated electromagnetic power absorption profiles in liver tissue for monopole antennas operating at a) 2.45 GHz and b) 5.8 GHz.

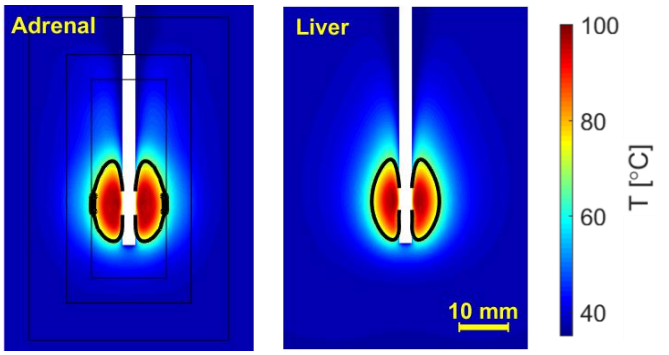

(a) (b)

Figure 5-3: Comparison of simulated temperature profiles in adrenal and liver tissue following 40 W, 60 s microwave heating at 2.45 GHz with coolant water temperature of 10 °C. The $\Omega = 1$ thermal damage contours estimating extent of the ablation zone are overlaid (black solid line).

5.3 Results

The optimal antenna tip length, l_m, was determined to be 6 and 2.5 mm for monopole antennas operating at 2.45 GHz and 5.8 GHz, respectively. Simulated normalized electromagnetic power absorption profiles in liver tissue for both frequencies are shown in Figure 5-2. These simulations illustrate the reduced electromagnetic power absorption along the applicator length at 5.8 GHz.

Figure 5-3 illustrates temperatures profiles in the multi-layer adrenal and liver tissue models following 40 W, 60 s microwave ablation with a 2.45 GHz monopole antenna. The black solid lines represent the $\Omega = 1$ thermal damage contour, and serve as an estimate of the ablation zone boundary (i.e. the $\Omega = 1$ contour represents the thermal damage process as being 63% complete). The ablation zone in the multi-layered adrenal model has an axial ratio of 0.99 (width/length) compared to 0.86 of the liver tissue. Although the size and the shape of the ablation zones are not identical, the ablation zone dimensions are similar (within 11.8 %) in both tissue models, suggesting that liver serves as a suitable surrogate tissue model for design and experimental evaluation of devices for adrenal ablation. Liver tissue was used for all subsequent modeling experimental studies.

Figure 5-4 illustrates simulated temperature profiles following 40 W ablations at 2.45 and 5.8 GHz for durations of 30, 60 and 90 s. As suggested by the electromagnetic power absoprtion profiles shown in Figure 5-2, the ablation zone length is shorter at 5.8 GHz compared to 2.45 GHz, due to the shorter wavelength, and thus shorter antenna length at the higher frequency. For both frequencies, the overall ablation size becomes larger for longer durations. It is observed that axial ratio, a measure of the sphericity of the ablation zone, increases with frequency, and remains steady for all treatment durations for each power and frequency combinations, with the exception of 30 W, 30 s at 2.45 GHz. Table 5-3 summarizes the ablation zone dimensions predicted by simulations.

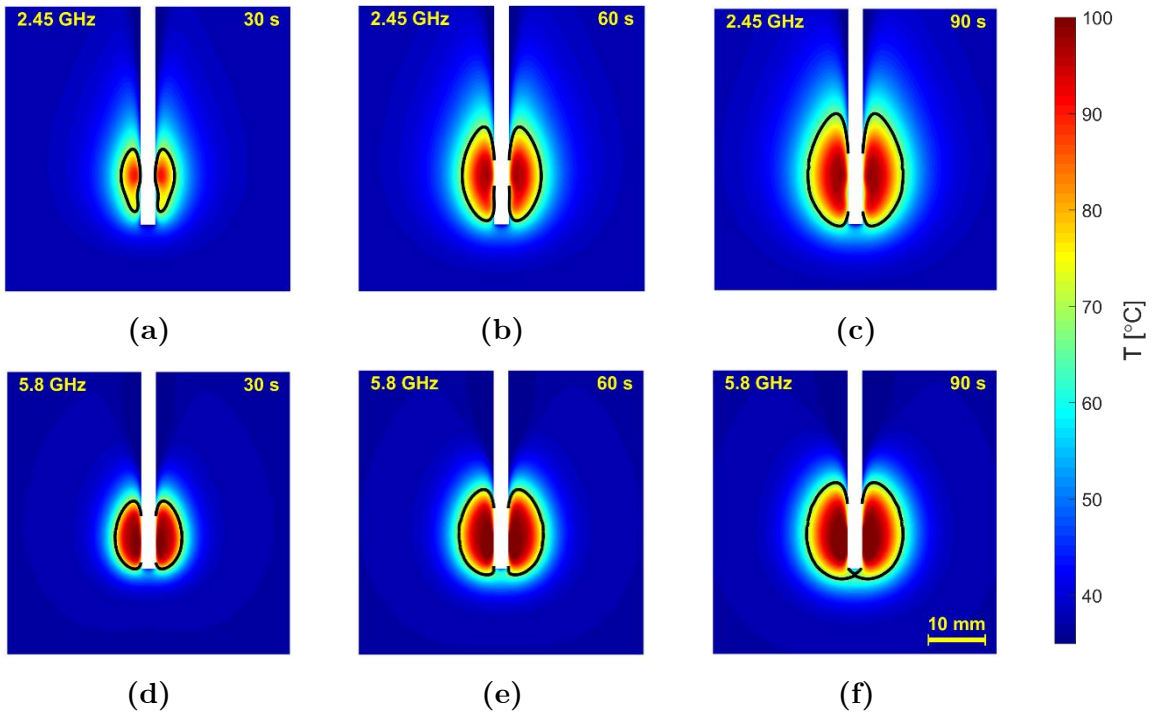

Figure 5-4: Comparison of the simulated temperature profile in liver tissue at frequencies of 2.45 and 5.8 GHz for different ablation time of 30, 60, and 90 s and input power of 40 W, with overlaid $\Omega = 1$ thermal damage contour (black solid line).

Table 5-3: Simulated ablation zone dimensions for different power and time combinations in liver tissue.

	2.45 GHz			5.8 GHz		
P_{in}, duration	Length [mm]	Width [mm]	Axial ratio	Length [mm]	Width [mm]	Axial ratio
30 W, 30 s	4.01	7.00	1.75	10.49	11.43	1.09
30 W, 60 s	12.60	11.81	0.94	13.33	14.52	1.09
30 W, 90 s	15.92	14.78	0.93	15.39	16.76	1.09
40 W, 30 s	10.99	9.52	0.87	12.04	12.12	1.01
40 W, 60 s	16.72	14.33	0.86	15.22	15.21	1.00
40 W, 90 s	20.04	17.30	0.86	17.97	17.96	1.00

Figure 5-5 shows example experimental ablation zones when using 30 W and 40 W input power, for 60 s at both frequencies. When increasing applied power level from 30 W to 40 W, we observe that the ablation volume increases 125.5% for the 2.45 GHz antenna, compared to 203.4% for 5.8 GHz. As anticipated, the length of the ablation zone (14.4

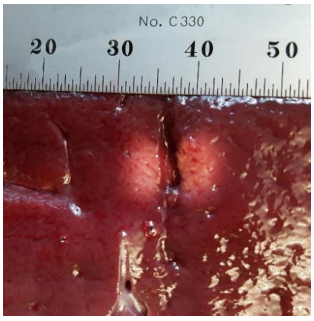

(a) 2.45 GHz, 30 W

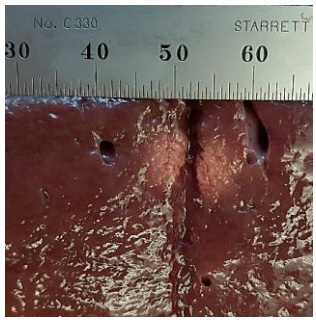

(b) 5.8 GHz, 30 W

(c) 2.45 GHz, 40 W

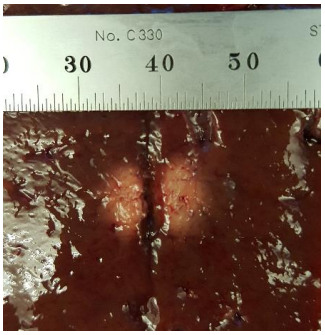

(d) 5.8 GHz, 40 W

Figure 5-5: Example ablation patterns following 60 s microwave ablation in *ex vivo* liver tissue: (a) 30 W, 2.45 GHz; (b) 30 W, 5.8 GHz; (c) 40 W, 2.45 GHz; and (d) 40 W, 5.8 GHz.

mm) created by the 2.45 GHz antenna was shorter than the ablation zone (8.8 mm) created by the 5.8 GHz antenna , attributed to the shorter antenna length at 5.8 GHz.

Figure 5-6 shows example experimental ablation zones following 30, 60, and 90 s for 40 W power applied at 2.45 GHz and 5.8 GHz. Higher frequency gives rise to higher axial ratio and longer ablation time creates larger ablation zones. Table 5-4 lists the experimentally observed ablation zone dimensions in *ex vivo* liver tissue.

As shown in Table 5-4, the ablation zone width is larger than the ablation zone length at 5.8 GHz, yielding an axial ratio greater than 1, in contrast to the observations at 2.45 GHz, for which the ratio is close to 1. We performed a second set of experiments at 5.8 GHz with different water temperatures to investigate the utility of adjusting

ablation zone length by adjusting coolant temperature. Figure 5-7 shows ablation zones at 5.8 GHz for input power of 30 W and 90 s duration with coolant temperatures of 10, 20 and 30 °C.

(a) 2.45 GHz, 30 s **(b) 2.45 GHz, 60 s** **(c) 2.45 GHz, 90 s**

(d) 5.8 GHz, 30 s **(e) 5.8 GHz, 60 s** **(f) 5.8 GHz, 90 s**

Figure 5-6: Example ablation patterns following 40 W microwave ablation in *ex vivo* liver tissue for 30, 60 and 90 s at 2.45 and 5.8 GHz.

Table 5-4: Experimentally measured ablation zone dimensions *ex vivo* in liver tissue with water-cooled 2.45 GHz and 5.8 GHz antennas. Data are presented as mean ± standard deviation (n = 5 for each combination).

	2.45 GHz			5.8 GHz		
P_{in}, duration	Length [mm]	Width [mm]	Axial ratio	Length [mm]	Width [mm]	Axial ratio
30 W, 30 s	9.2 ± 0.4	6.6 ± 0.5	0.72	5.9 ± 0.5	7.4 ± 0.4	1.25
30 W, 60 s	11 ± 0.63	11.2 ± 0.7	1.02	6.0 ± 1.0	8.9 ± 1.1	1.49
30 W, 90 s	11.6 ± 1.0	12.7 ± 1.0	1.09	9.0 ± 0.0	12.9 ± 0.5	1.43
40 W, 30 s	8.2 ± 1.9	7.3 ± 1.4	0.89	6.7 ± 0.8	9.2 ± 1.2	1.38
40 W, 60 s	14.4 ± 1.1	14.7 ± 1.4	1.02	8.8 ± 1.0	12.8 ± 0.7	1.47
40 W, 90 s	17.1 ± 1.6	17.6 ± 1.5	1.03	10.2 ± 1.2	13.6 ± 0.7	1.33

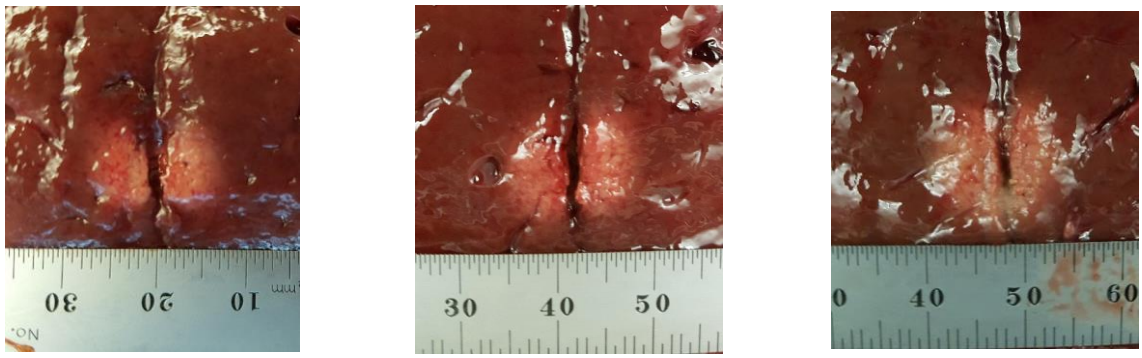

(a) (b) (c)

Figure 5-7: Experimentally observed ablation zone in *ex vivo* liver tissue following 30 W, 90 s microwave ablation at 5.8 GHz with coolant temperature of a) 10, b) 20 and c) 30 °C.

Table 5-5 summarizes the measured ablation dimensions. These results suggest that increasing the temperature of the cooling water from 10 – 30 °C has the primary of effect of increasing the ablation zone length, with minimal change in the ablation zone width (average change of 0.27 mm in ablation zone width across all coolant temperatures).

Multi-way ANOVA using a 5% significance level was used to identify the main factors determining the ablation zone length and width. Table 5-6 shows the p-values for ablation zone length and width, respectively. These results indicate that operating frequency was the primary factor that affected the ablation zone length. Ablation time was the primary factor that affected the ablation zone width. According to the interaction p-values, the interactive effects were not statistically significant.

Table 5-5: Ablation zone dimensions in *ex vivo* liver tissue at 5.8 GHz for power of 30 W and 90 s duration with coolant temperatures of 10, 20 and 30 °C (n = 3).

Coolant Temp. [°C]	Length [mm]	Width [mm]	Axial ratio
10	9.00 ± 0.00	12.90 ± 0.49	1.43
20	9.17 ± 0.62	12.00 ± 0.82	1.31
30	12.50 ± 0.71	13.17 ± 0.62	1.05

Table 5-6: p-values of main effects and their interaction for length and width of ablation zone in *ex vivo* liver tissue following 3-way ANOVA analysis.

Effect/interaction	Ablation zone length	Ablation zone width
Frequency	0.0426†	0.4091
Power	0.1417	0.0917
Time	0.1042	0.0446†
Frequency*Power	0.6140	0.6497
Frequency*Time	0.4943	0.3600
Power*Time	0.3859	0.5709

† *p*-values with statistical significance

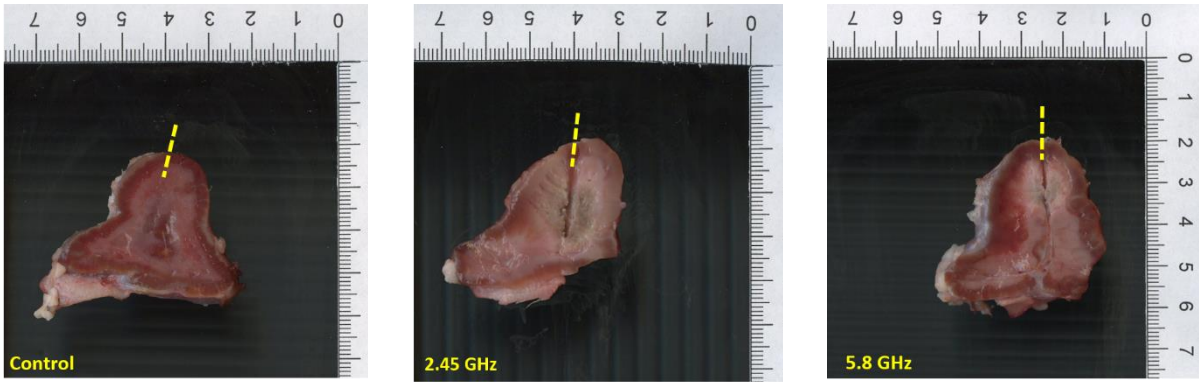

(a) (b) (c)

Figure 5-8: Comparison of the observed ablation zones in bovine adrenal gland at different frequencies with a non-ablated gland: a) control sample f = 2.45 GHz, P_{in} = 0 W, t = 180 s, $T_{coolant}$ = 10 °C, b) ablated sample at f = 2.45 GHz, P_{in} = 50 W, t = 180 s, $T_{coolant}$ = 10 °C and c) ablated sample at f = 5.8 GHz, P_{in} = 40 W, t = 90 s, $T_{coolant}$ = 30 °C. The dashed line illustrates the antenna insertion track into the adrenal tissue sample.

Ablations were performed on bovine adrenal glands in order to verify the ability to create ~10-20 mm spherical ablation zones with the antennas investigated in this study. Figure 5-8 compares example ablation zones created by the water-cooled 2.45 and 5.8 GHz antennas. As evident in Figure 5-8(a), which ilustrates a section adrenal gland where no ablation was performed, it is challenging to assess the extent of ablation using the zone of visibly discolored tissue due to the distinct coloration of the adrenal medulla and cortex. Ablation length and width at 2.45 GHz were L = 16.0 ± 0.5 and W = 15.2 ± 0.3 for input power of 50 W and ablation time of 180 s. For the 5.8 GHz ablation, length and

width were L = 10.2 ± 0.4 and W = 11.8 ± 0.6 for input power of 40 W, ablation time of 90 s and water temperature of 30 °C.

5.4 Discussion

This study was conducted to assess methods for creating short, spherical MWA zones in the range of 0.5 – 4 cm^3 using water-cooled coaxial monopole antennas, with application to treatment of benign adrenal adenomas. We hypothesized that using water-loaded antennas operating at 2.45 and 5.8 GHz would enable the creation of ablation zone lengths in the range of 10 – 20 mm. The simulated electromagnetic power absorption profiles illustrated in Figure 2, indicate that the shorter antenna length at 5.8 GHz (l_m = 2.5 mm) provides improved control of microwave heating along the length of the applicator, compared to the 2.45 GHz antenna (l_m = 6 mm). We found that 5.8 GHz MWA antennas yielded power deposition more localized to the applicator, compared to 2.45 GHz, similar to other studies [63]. In previous studies with uncooled dipole antennas, it was shown that this more localized power deposition led to higher temperatures in proximity to the antenna. This led to a more prominent role of thermal conduction in growth of the ablation zone over ~5-10 mins, yielding ablation zone of similar size to ~2 GHz devices. However, in our study, which considered ~30-90 s ablations with cooled devices, operating at 5.8 GHz yielded ablation zones of smaller diameter. This can be

attributed to the shorter ablation duration, where thermal conductivity plays a limited role.

The primary findings from the simulation results presented in Figure 5-4 and Table 5-3 are: (1) water-cooled monopole antennas designed to operate at 5.8 GHz yield smaller ablation zone lengths compared to those designed to operate at 2.45 GHz, (2) the ablation zone width grows with increased ablation duration, and (3) increased applied power yields increase in both ablation zone width and length. The simulations further suggested that for a given applied power level and operating frequency, the ablation zone shape generally remained steady (within 1%) for heating durations ranging from 30 – 90 s. An exception to this trend was the 30 W, 30 s ablation zone at 2.45 GHz, for which simulations predicted an axial ratio of 1.75, compared to 0.94 and 0.93 for 60 s and 90 s ablations, respectively. This unusually large axial ratio at 30 W, 30 s is primarily due to the short simulated ablation zone length (4 mm), which could be attributed to the convective cooling boundary condition employed for simulating cooling along the applicator shaft, the effects of which may be more pronounced for low power, short duration ablations.

Experimentally observed ablation zones in *ex vivo* liver tissue for fixed durations indicated that both ablation zone width and length grow with increased applied input power (Figure 5-5 and Table 5-4). Thus, applied power alone does not allow for independent control of ablation zone length or width. Figure 5-6 shows example ablation zone images following experimental ablations in *ex vivo* liver tissue using the same applied

energy levels as in the simulations shown in Figure 5-4. The ablation profiles and dimensions summarized in Table 5-4 demonstrate trends similar to the simulations in terms of adjustment of ablation length and width by choice of frequency and ablation time, respectively. These observations were also statistically confirmed by 3-way ANOVA tests (summarized in Table 5-6) at 5% significance level. A p-value of 0.0426 indicated frequency as the main factor for controlling the ablation zone length, and a p-value of 0.0446 indicated ablation duration as the main factor for controlling the ablation zone width.

The experimentally observed ablation zones reported in Table 5-4 show that spherical ablation zones (axial ratio ≈ 1) can be created in the diameter range of 10 – 20 mm with the following combinations: (2.45 GHz, 30 W, 60 s, diameter $\approx$ 11 mm), (2.45 GHz, 40 W, 60 s, diameter $\approx$ 14.5 mm), and (2.45 GHz, 40 W, 90 s, diameter $\approx$ 17.3 mm). However, all the axial ratios were greater than 1 for the 5.8 GHz antenna. In other words, the ablation zone width is larger than the ablation zone length at 5.8 GHz. To assess the feasibility of creating spherical ablation zones (axial ratio = 1) at 5.8 GHz, we experimentally investigated the impact of adjusting temperature of the cooling water on the ablation zone length. The experimental results shown in Figure 5-7 and Table 5-5 illustrate how using cooling water at a temperature of 30 °C, compared to 10 °C in the earlier experiments, allowed for increased heating along the applicator length. The experimentally measured axial ratio decreased from 1.43 to 1.05 by changing cooling water

temperature from 10 to 30 °C for ablation combination of (5.8 GHz, 30 W, 90 s, diameter ≈ 12.8 mm). It is noted that if ablative temperatures are not achieved along the antenna insertion path when coolant temperature is low (10 °C), track ablation techniques can be utilized which is common in clinical practice during RF and MWA. During track ablation, low power levels without coolant flow is applied while slowly retracting the ablation applicator, thereby allowing tissue immediately adjacent to the applicator to be ablated [174], [175].

Ablations performed in bovine adrenal glands showed that the 5.8 GHz antenna could create spherical ablation zones in the lower range of the targets with diameter 10 – 20 mm whereas the 2.45 GHz antenna could be used in the higher range. Input power and time combination were obtained empirically for both frequencies. We found that we had to use different power and time combinations compared to those in liver tissue. This may be because the discoloration of adrenal tissue at elevated temperatures was less clear than in liver, and the thermal dose required to observe this discoloration may be different in liver and adrenal tissue. Additionally, the color of the adrenal medulla, which is similar to that of ablated cortex, makes it challenging to accurately assess the zone of tissue ablation by observing extent of tissue discoloration.

A prior clinical study employed a monopolar radiofrequency electrode for thermal ablation of the adrenal gland [166]. While successful in destroying the targeted adenoma, the approach also thermally ablated surrounding adrenocortical and medullary tissue.

While RFA was both minimally invasive and clinically efficacious procedure for PA, it is useful only in the context of unilateral disease, given the collateral destruction of normal tissue. This therefore leaves a considerable clinical need to develop selective ablation, which can be used for unilateral and bilateral disease. Currently available microwave ablation devices have primarily been designed to create large volume ablation zones [84], [158], and do not provide a means for scaling thermal ablation zone size to the range of 10 – 20 mm in diameter, while maintaining the ablation zone sphericity. The results presented here demonstrate the feasibility of creating 10 – 20 mm diameter spherical ablation zones using water-cooled monopole antennas, by appropriate selection of operating frequency, cooling water temperature, applied power level, and ablation duration. While we investigated MWA for selective adrenal ablation, we note that other minimally-invasive thermal therapy modalities such as RFA [176] and lasers [177], as well as non-thermal approaches such as irreversible electroporation [178], may also have potential for treatment of benign adrenal adenomas, if optimized to deliver small treatment zones and maximally spare normal adrenocortical cells.

A limitation of this study is the use of static values for dielectric properties in the simulations, since there are no reported temperature-dependent dielectric property data available for adrenal tissue. Similarly, temperature dependent dielectric properties of liver were unavailable at 5.8 GHz. The discrepancy in dimensions of ablation zones predicted by simulations compared to experiment may be due to the use of static tissue dielectric

properties in the simulations. Ongoing efforts in our lab are geared towards assessing the relationship between residual adrenal function following selective thermal ablation of targeted regions within the adrenal medulla and cortex. Similar to other reports on design of devices for microwave ablation employing computational models and experiments in *ex vivo* tissue [45], [137], [165], perfusion effects were not considered in our simulations and experiments. Compared to longer treatment durations used for creation of large ablation zones (e.g. in the liver), it is likely that perfusion will have a reduced impact for short duration ablations and can be compensated by increasing the applied input power.

5.5 Conclusion

We evaluated water-cooled monopole antennas, designed to operated 2.45 GHz and 5.8 GHz, for creating short spherical ablation zones with application to thermal ablation of benign adrenal adenomas. Computational models and experiments in *ex vivo* tissue were used to analyze the effect of frequency, applied power, ablation duration, and coolant temperature on the ablation length and width. Both simulation and measured results demonstrated the ability to create spherical ablation zones with a diameter in the range of 10 – 20 mm through appropriate selection of applied power, ablation duration, and coolant temperature. Statistical analysis of the experimentally measured ablation zones showed that ablation length is primarily controlled by the operating frequency, while

ablation width is primarily controlled by the ablation duration and temperature of the cooling water.

6 Broadband Dielectric Properties of *Ex Vivo* Bovine Liver Tissue Characterized at Ablative Temperatures[4]

6.1 Introduction

Microwave ablation (MWA) is a minimally invasive treatment for destruction of tissue by localized heating to cytotoxic temperatures. MWA has been clinically applied for treatment of tumors in the liver, kidney, lung, and bone [56], as well as benign targets, such as the endometrial lining of the uterine cavity for treating menorrhagia [24] and cardiac arrhythmias [179]. The majority of MWA systems in current clinical use deliver

[4] This chapter has been published as: H. Fallahi, J. Sebek, and P. Prakash, "Broadband Dielectric Properties of *Ex Vivo* Bovine Liver Tissue Characterized at Ablative Temperatures," *IEEE Trans. Biomed. Eng.*, 2020.

microwave power at a frequency of 915 MHz or 2.45 GHz; systems operating at other frequencies are under investigation [63]. Microwave propagation and absorption within tissue is a function of the dielectric properties – relative permittivity and effective conductivity – which are known to vary widely across tissue type, and as a function of frequency, water content, and temperature. The dielectric properties of target tissue are key inputs for computational models of MWA, which are widely used for device design and optimization, device characterization and as part of regulatory studies, and are under development for planning, guiding delivery, and assessing clinical ablation procedures [180].

Gabriel *et al.* [58] reported the dielectric properties of different tissues across a broad range of frequencies, at temperatures close to the physiologic temperature range (~37 °C). These data have been invaluable for driving simulation-based design of microwave thermal therapy systems. During MWA, tissue temperatures may rise from baseline to ~150 °C [1]. At these elevated temperatures, tissue structural changes and water loss [181], [182] lead to reversible and irreversible changes in tissue dielectric properties [183], [184]. Therefore, models employing static tissue dielectric properties at elevated temperatures may not accurately capture the ablation outcome [136]. Furthermore, some recent studies have proposed exploiting changes in tissue dielectric properties at ablative temperatures to monitor transient growth of the ablation zone [185].

Further development of these techniques will require characterization of broadband tissue dielectric properties at ablative temperatures.

While several studies have investigated the dielectric properties of tissue as a function of temperature, few have extended these measurements to temperatures exceeding 90 °C, which are commonly observed during tissue ablation [69], [186]. In recent years, some studies have reported temperature-dependent dielectric properties of liver tissue [136], [172], [187], which include the dynamic change of properties at temperatures as high as 100 °C. However, these data have predominantly been limited to the single frequency of 2.45 GHz; the lack of knowledge of dielectric properties at ablative temperatures at other microwave frequencies has hampered the development of ablative technologies operating at frequencies other than 2.45 GHz [24], [28], [63]. As researchers investigate ablation systems at other operating frequencies, and wideband approaches for monitoring treatment progress, characterization of tissue dielectric properties across a broad range of frequencies in the ablative temperature range will be critical. Furthermore, the bulk of prior studies of temperature-dependent tissue dielectric properties at 2.45 GHz have not investigated the impact of the rate of heating on the measured dielectric properties [188]. This is of importance since the heating rate during MWA varies considerably within tissue as a function of spatial position relative to the radiating antenna. Broadband temperature-dependent measurement of dielectric properties of bovine liver will provide the foundation for further model-based design and development

of next-generation minimally invasive MWA systems as well as wideband techniques for real-time monitoring of MWA [189], [190].

In this work, we experimentally measured the changes in broadband dielectric properties of fresh *ex vivo* bovine liver tissue (frequencies between 0.5 to 6 GHz) over the temperature range of 20 to 130 °C. The measurements were performed at slow heating (SH) rate, medium heating (MH) and fast heating (FH) rate, of approximately 6.4 °C/min, 11.3 °C/min and 16.9 °C/min, respectively. Then, the measured data were fitted to a parametric model describing tissue dielectric properties as function of frequency and temperature or thermal dose, suitable for application in computational models of MWA. Finally, the parametric models were evaluated by comparing simulated return loss of MWA antennas operating at 2.45 and 5.8 GHz with experimentally measured return loss during MWA experiments.

6.2 Methods

6.2.1 Dielectric property measurements

Among the different methods for dielectric measurement [191]–[194], the open-ended coaxial probe technique has been widely used for dielectric characterization of tissue. This method utilizes a coaxial probe connected to a vector network analyzer (VNA). The VNA measures the signals reflected at the tip of the coaxial probe, at the interface with the tissue sample. Tissue relative permittivity, ϵ_r, and effective

conductivity, σ_{eff}, are computed from the measured complex reflection coefficients. We used an HP 8753D VNA with the frequency range of 0.5 to 6 GHz and the slim form open-ended dielectric probe kit (Keysight 85070E). Dielectric properties of the samples were recorded at 401 points logarithmically distributed across the frequency range [195]. The standard calibration (air, short, distilled water) procedure was performed before each test. The performance of the probe was validated by measuring the dielectric properties of ethanol at 25 °C. The maximum difference between our measurement and published data [196] was approximately 0.88 unit for relative permittivity and 0.16 S/m for effective conductivity, similar to [186].

A fiber optic temperature sensor (Qualitrol OptiLinkTM, T1C-02-PP10 with Neoptix Reflex signal conditioner) was positioned flush with the dielectric probe in order to co-register the tissue sample temperature at all times when dielectric properties were recorded. A piece of polyimide tube was employed to keep the temperature sensor in place. The sensor measured the temperature with an acquisition rate of 1 sample/s.

The tissue sample was placed in a custom-made copper box on top of a hot plate (ThermoScientific), similar to the approach we previously reported for measuring dielectric properties of lung tissue [197]. Briefly, the tissue sample within the copper sample holder is heated by thermal conduction from the hot plate. A set of thin copper fins affixed to the top of the copper sample holder provided a heat transfer path from the hot plate surface to the upper edges of the sample holder, with a goal of minimizing the

temperature gradient over the sample. We found this approach of heating the tissue sample to be more repeatable than previous efforts using a microwave antenna to heat the tissue [30]. The coaxial probe was positioned approximately above the center of the sample using a lab jack. We pushed the tip of the probe at least 5 mm onto the sample. The values of dielectric properties were automatically captured every 5 s during the course of heating. Figure 6-1 shows the experimental setup.

The tissue samples were excised from fresh bovine liver purchased from a local slaughterhouse, and transported to our lab in a plastic bag placed on ice. Tissue was cut into 2×2×2 cm^3 samples and kept on ice in a cooler. Dielectric data were measured within ~12-24 hours post-mortem. Measurements were performed on 15 samples obtained from two bovine livers (6 samples from liver I and 9 from liver II). Slow, medium and fast heating rates were achieved by setting the hot plate temperature to 200 °C, 300 °C and 400 °C, respectively (n = 3 measurements at each heating rate). When the sample temperature reached ~90 °C, the hot plate temperature was set to max (540 °C) in order to provide adequate heat to overcome the latent heat of water vaporization and raise the tissue temperature above 100 °C. Dielectric properties of samples from liver I were measured using the slow heating rate while those of samples from liver II were measured using different heating rates. When changes of dielectric properties due to different heating rates were compared with each other, only the data from liver II were used in order to exclude the data variability due to the tissue itself.

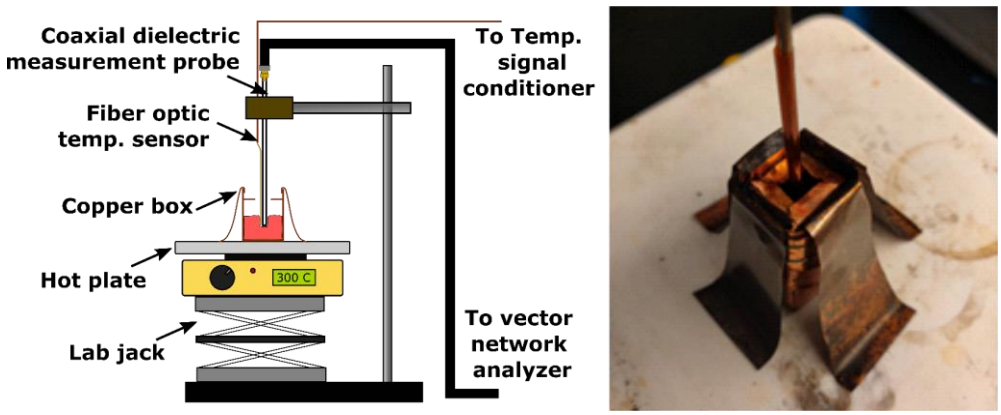

Figure 6-1: a) Experimental setup for measurement of dielectric properties of liver tissue during heating and b) photo of the custom copper box.

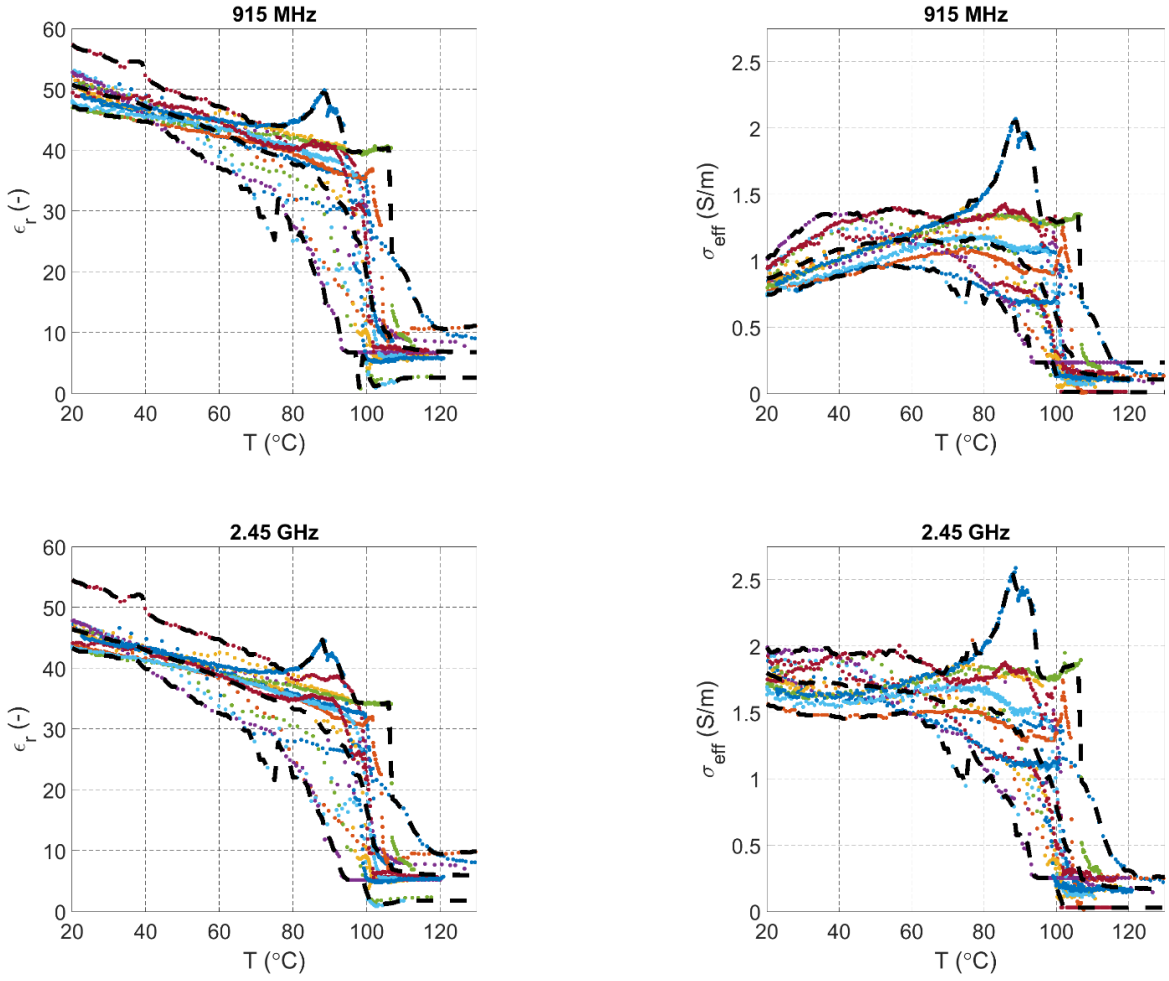

Figure 6-2: Measured temperature-dependent dielectric properties of bovine liver (n = 15 samples) at 915 MHz and 2.45 GHz. Estimated non-parametric mean, upper and lower envelopes of the measured data are shown in black dashed lines.

6.2.2 Parametric model for temperature and thermal isoeffective dose dependent broadband dielectric properties

The measured dielectric data were interpolated to a linearly spaced grid of 110 temperature points at each of the measured 401 frequencies for each of the 15 samples. Examples of the resulting interpolated data and estimated non-parametric envelopes are illustrated in Figure 6-2. The lower, mean and upper envelopes were synthesized by taking the minimum, mean, and maximum value of dielectric properties at each interpolated temperature.

For the dielectric properties shown in Figure 6-2, it is apparent that the data can be well represented by a piecewise linear model with three temperature intervals: the interval between 20 °C and a temperature near the point of water vaporization, followed by a shorter interval around 100 °C where the dielectric properties drop, and the interval above 100 °C. We utilized a piecewise linear function to represent the measured datasets similar to the procedure described in [197]. Detailed description of the mathematical model together with the derived fitting parameters is presented in Appendix A:.

The measured sample temperature data were also used to compute the thermal isoeffective dose, which provides a means for relating a non-isothermal exposure to cumulative equivalent minutes of isothermal heating at 43 °C (CEM43), [138]

$$CEM43 = \sum_{i=1}^{N} R_{CEM}{}^{(43-T_i)}\ t_i, \qquad (1)$$

where R_{CEM} is the constant for proportionality for the process modeled, T_i is the temperature of time interval i (°C), and t_i is the time at T_i (minutes). The values used for R_{CEM} at temperatures below and above the breakpoint, 43 °C, were 0.25 and 0.5, respectively [198]. Presenting dielectric properties as a function of thermal dose provides a means for capturing changes in dielectric properties based on the time-temperature history during heating, rather than temperature alone. A similar parametric model and optimization approach was employed to find the best parametrized piecewise fits for dielectric properties as a function of the logarithm of CEM43.

6.2.3 Experimental assessment of temperature and thermal isoeffective dose dependent dielectric property models

We conducted experiments to assess the ability of the temperature and thermal dose dependent dielectric property parameterizations to capture dielectric property changes in liver tissue during MWA. The return loss of an antenna is a parameter that captures the impedance mismatch between the ablation antenna and the feeding transmission line. The antenna impedance is primarily a function of the dielectric properties of the tissue within which the antenna is inserted, as well as the antenna dimensions. As tissue dielectric properties change at elevated temperatures during the course of an ablation, return loss also changes. Thus, we sought to compare experimentally measured changes in antenna return loss against simulated return loss during the course of an ablation, when using simulations employing the temperature or thermal dose

dependent dielectric properties described in Section 6.2.2. Ablations were performed with interstitial dipole antennas tuned to operate at 2.45 and 5.8 GHz, following the method described in [199]. Briefly, finite element method computational models were used to solve the steady-state Helmholtz equation to determine the electric field and power loss density profiles in tissue, which served as the heat source for a transient heat transfer model. A coupled model in COMSOL Multiphysics v5.3 was implemented such that the tissue physical properties were updated, and the electromagnetic model solved again, after each time step taken by the transient solver (more details are provided in Appendix A:). The antenna gap length was 1 for both frequencies and the dipole arm length was 10.9 and 5 mm respectively. Ablations were performed at 2.45 GHz and 5.8 GHz in fresh bovine liver (sample dimensions: $L = 80$ mm, $W = 70$ mm, $H = 70$ mm), using the following applied energy levels: ($f = 2.45$ GHz, $P_{in} = 25$ W, $t = 10$ min), ($f = 2.45$ GHz, $P_{in} = 40$ W, $t = 4$ min), ($f = 5.8$ GHz, $P_{in} = 25$ W, $t = 10$ min), and ($f = 5.8$ GHz, $P_{in} = 40$ W, $t = 4$ min). At each experimental group, ablation experiments were performed in triplicate (i.e., $n = 3$). During the course of ablation, return loss was measured with a statistical RF power meter (Bird 7022). We applied the temperature-dependent and thermal dose-dependent functions into computational models of MWA, previously described in [199]. Antenna return loss was simulated when using dielectric property parameterizations capturing the lower, mean and upper envelopes of each dielectric property.

6.3 Results

The measured temperature profiles adjacent to the dielectric probe recorded for SH, MH and FH rates are plotted in Figure 6-3(a). At each heating rate, dielectric measurements were performed on three samples. The recorded transient temperature data from each of the three experiments at each heating rate were fitted to a linear function over the temperature range 30 – 85 °C, where there was approximately linear rise in temperature. The slope of the fitted function is the heating rate. The observed mean and standard deviation were calculated from the three slopes computed for experiments at each experimental heating rate. The mean ± standard deviation of the experimental heating rates were 6.4±0.3 °C/min, 11.3±2.2 °C/min and 16.9±2.0 °C/min for SH, MH and FH rates, respectively. These data indicate our experimental setup is capable of

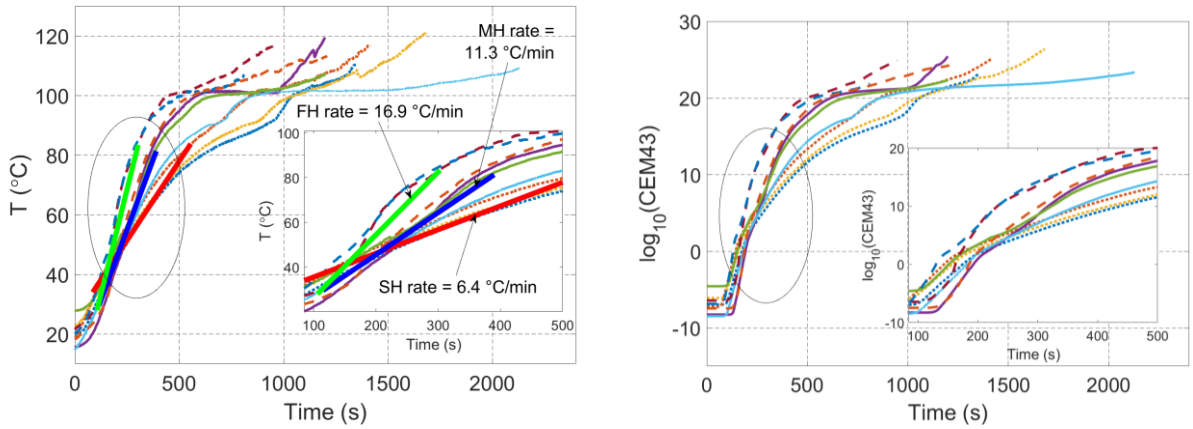

(a) (b)

Figure 6-3: (a) Measured transient temperature adjacent to the dielectric probe during heating with slow (SH), medium (MH) and fast (FH) heating rates. (b) Corresponding thermal isoeffective dose for the temperature profiles shown in (a) (SH→Dotted lines, MH→Solid lines, FH→Dashed lines).

heating the tissue at different rates in a consistent manner. Figure 6-3(b) demonstrates changes in thermal isoeffective dose delivered to the tissue adjacent to the dielectric probe, computed from the temperature profiles in Figure 6-3(a).

Figure 6-4 illustrates the fitted piecewise functions for mean, upper and lower envelopes of the measured relative permittivity and effective conductivity across all 15 tissue samples at three example frequencies: 915 MHz, 2.45 GHz and 5.8 GHz. It is noted that when we compared the maximum/minimum envelopes with those of mean $\pm$ two standard deviations, we obtained similar fit functions for upper and lower envelopes (see Figure A-5 and Table A-1 in Appendix A:). At all frequencies, a sharp drop is observed at temperatures over 90 °C. This may be attributed to tissue desiccation and water vaporization at elevated temperatures.

Figure 6-5 compares the mean envelope of the data from liver I ($n = 6$) with the mean envelopes of different heating rates from liver II ($n = 3$ for each heating rate). Heating rate does not appear to play a major role on dielectric properties since data variability caused by heating rate (standard deviations of 2.25 and 0.14 S/m for ϵ_r and σ) is on the same order (76% and 155%) as the data variability caused by different liver samples (standard deviations of 3.02 and 0.09 S/m for ϵ_r and σ). This is illustrated in Figure 6-5, where one can see well-overlaid confidence intervals of datasets for different heating rates as well as liver samples.

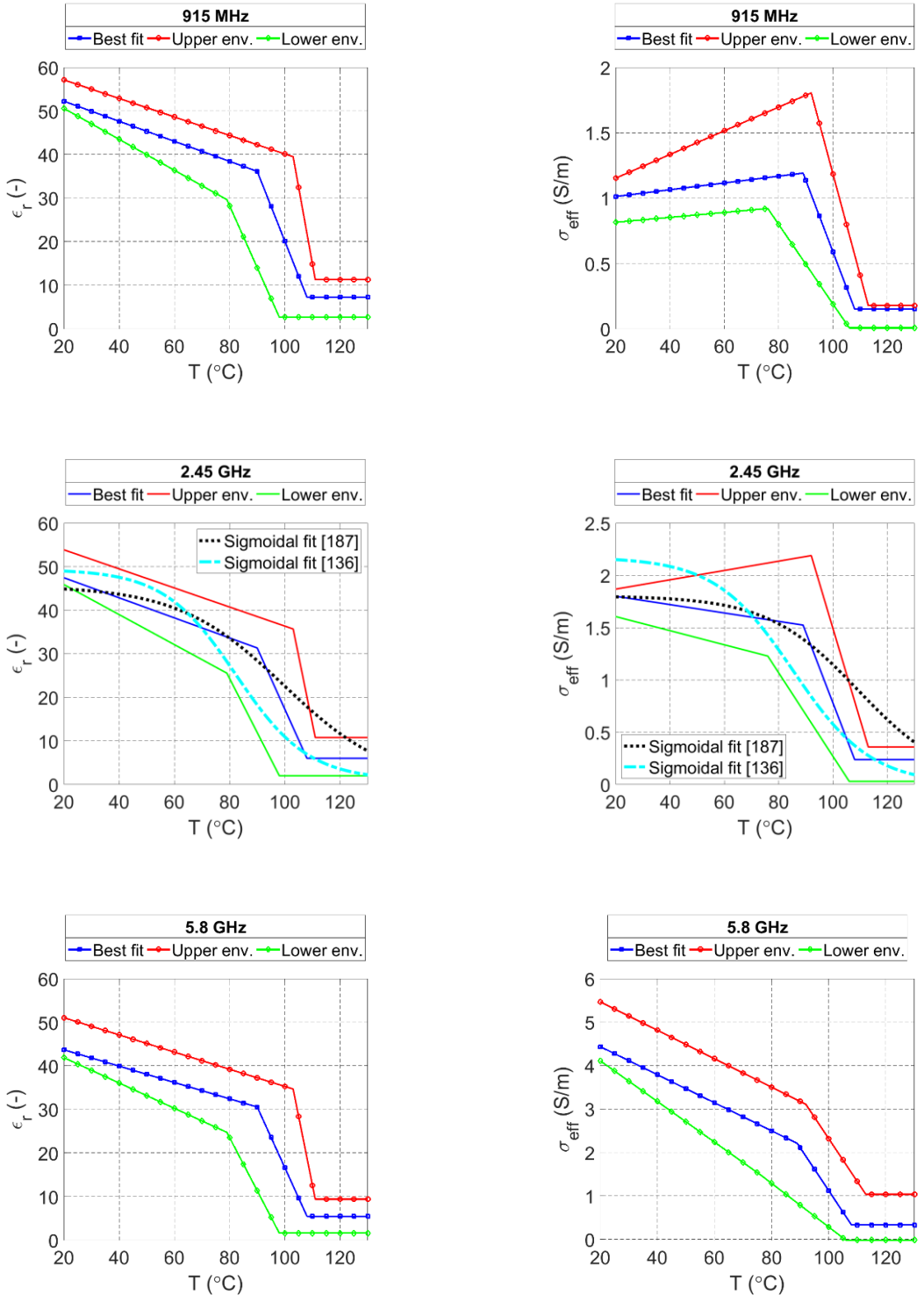

Figure 6-4: Illustration of the parametric fits for the mean, upper and lower envelopes of the overall measured temperature-dependent dielectric property data at three example frequencies. The middle plots compare our fitted functions at 2.45 GHz with the sigmoidal fits from literature [136], [187].

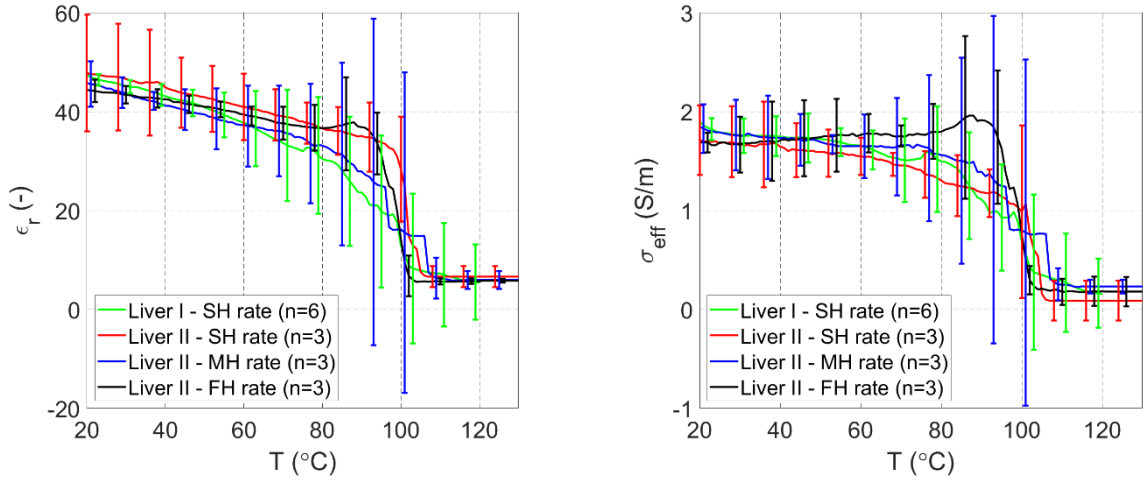

Figure 6-5: Comparison of mean envelope of the data from liver I with the mean envelopes of different heating rates from liver II measured at the frequency of 2.45 GHz. The error bars indicate two standard deviations.

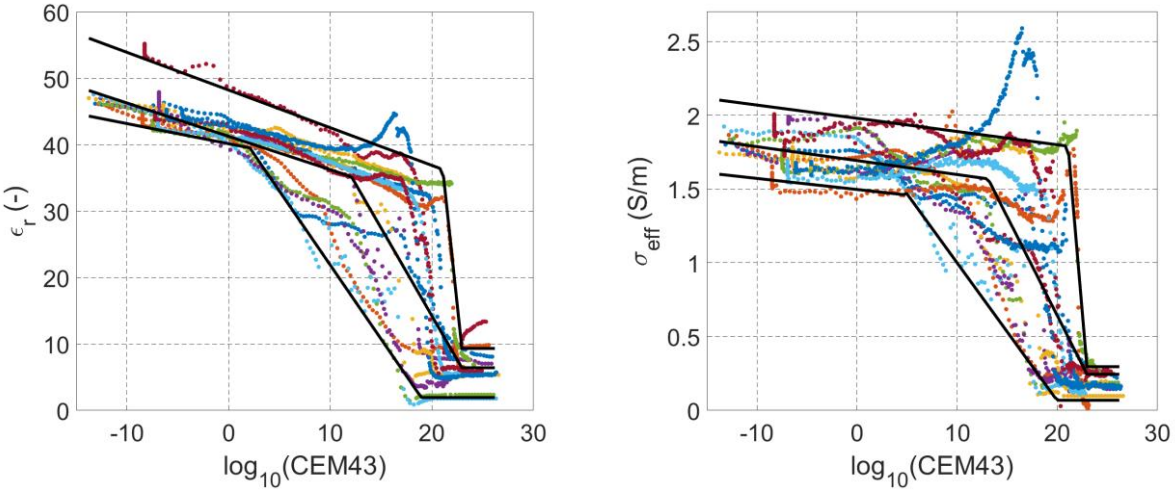

Figure 6-6: Measured dielectric data as a function of thermal isoeffective dose at 2.45 GHz overlaid with the fitted functions for mean, upper and lower envelopes.

Figure 6-6 shows the measured dielectric properties of liver tissue at 2.45 GHz as a function of the logarithm of thermal dose. The fitted piecewise functions of relative permittivity and effective conductivity as a function of thermal dose are overlaid on the measured data in Figure 6-6.

Figure 6-7 compares the transient changes in measured and simulated return loss (S_{11}) as during ablations at 2.45 GHz and 5.8 GHz. The effect of using dielectric property parameterizations corresponding to the lower, mean and upper envelopes in simulations is illustrated.

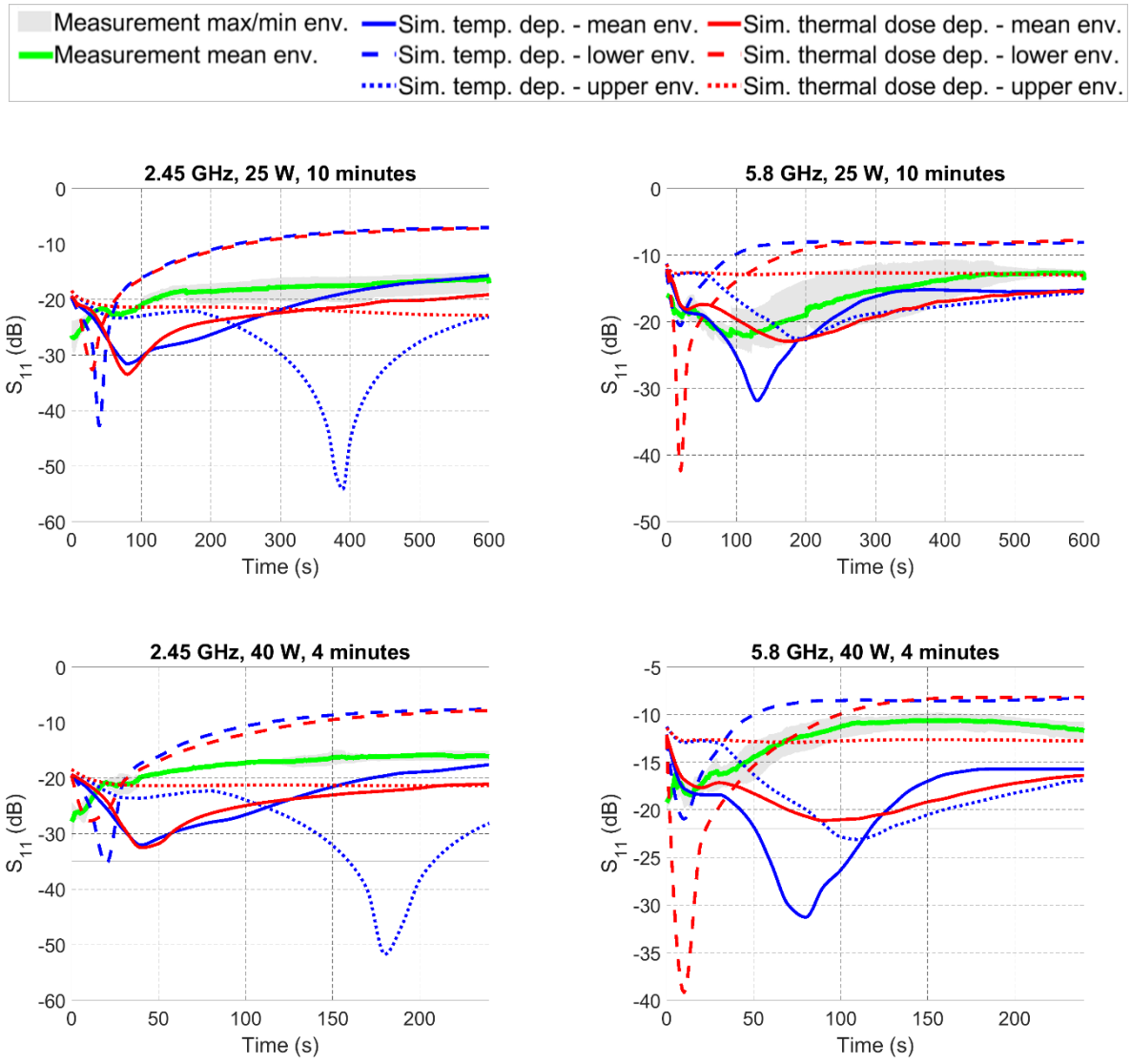

Figure 6-7: Comparison of experimentally measured and simulated S_{11} as a function of time during ablation with dipole antennas operating at 2.45 GHz and 5.8 GHz. Simulations considered lower, mean and upper envelopes of the temperature and thermal isoeffective dose dependent dielectric properties.

6.4 Discussion

The goal of this study was to measure the broadband dielectric properties of *ex vivo* bovine liver tissue starting at room temperature and continuing over the ablative temperature range. These data have application to the development of computational models for microwave ablation applicator and system design, as well as validation of computational models used for simulating clinical procedures. Moreover, we derived a piecewise linear function characterizing frequency and temperature dependence of tissue dielectric properties, suitable for use with computational models.

Among the prior studies on temperature-dependent dielectric properties of tissue, there are only a few with data reported at ablative temperatures (i.e. T $>$ 90 °C) [136], [187]. The measured dielectric properties reported in these studies have been limited to a single frequency (2.45 GHz), and only a single heating rate was used. The broadband dielectric properties and parametric models presented in this study may contribute to the continued development of ablation technology operating at frequencies other than 2.45 GHz, as well as broadband techniques for monitoring growth of the ablation zone, the presented dielectric properties.

The dielectric property parameterizations plotted in Figure 6-4 illustrate dielectric property changes can be grouped over three temperature intervals: gradual changes in dielectric properties at temperatures in the range 20 to ~90 °C; a sharp drop in dielectric properties over the temperature range ~90 to ~110 °C; and relatively constant dielectric

properties beyond ~110 °C. The average error for the piecewise linear parametrization was low (e. g. 1.06 and 0.0051 in case of mean ϵ_r and σ_{eff} envelopes), indicating they are a suitable parametrization for these data (see Appendix A:). While relative permittivity at different frequencies changes similarly as a function of temperature, effective conductivity changes during heating vary across frequency ranges. An important observation is the change of the effective conductivity slope in the first temperature region from positive values at lower frequencies (0.5–1.64 GHz) to negative values at higher frequencies (1.64–6 GHz). The positive slope of effective conductivity at low temperatures is in agreement with the measurements in [186], where broadband dielectric properties were presented up to temperatures of ~65 °C (see Figure A-4 in Appendix A:).

The recommended settings for use of the open-ended coaxial dielectric measurement probe employed in the presented study suggest a homogeneous material within 5 mm radially from the probe surface. For this reason, we selected the sample size for tissue to be 2×2×2 cm^3, exceeding the minimal recommend sample size. However, given the relatively large sample size, and the source of heating, undoubtedly there existed a temperature gradient within the sample. It is noteworthy that several studies have identified that the open-ended dielectric probe measurement method is most sensitive to tissue within 0.3 mm of the probe surface, for the ~2.2 mm dielectric probe used in the present study [200], [201]. While there may be some thermal heterogeneity within this

small volume, it is likely to be considerably small, and may have a relatively small impact on the dielectric measurements, compared to probes that have greater sensing depths.

The presented fitted piecewise function for dielectric properties at 2.45 GHz follows a trend similar to the sigmoidal models reported in the literature (see Figure 6-4). Changing the heating rate did not yield appreciable changes in the measured relative permittivity. However, varying the heating rate did give rise to different temperature dependencies for the effective conductivity in the range of 40 to 100 °C. When heating the sample using a lower heating rate (6.4 °C/min), a more rapid drop in effective conductivity was observed as a function of temperature, compared to higher heating rates. Overall, the dielectric data sensitivity due to different heating rates is within the same range as that of the tissue variability. The dielectric property parameterizations as a function of thermal dose provide a means for capturing changes in dielectric properties of tissue at varying heating rates.

During a MWA procedure, the antenna's return loss (S_{11}) may provide an indication of the changes in tissue dielectric properties. We used the temperature and thermal dose dependent dielectric property parameterizations presented in this paper in computational models of microwave ablation with dipole antennas operating at 2.45 GHz and 5.8 GHz and compared the simulated changes in S_{11} with measured changes in return loss during experimental ablations. The correlation coefficients listed in Table 6-1 provide a means for assessing the similarity between the measured and simulated S_{11} during

ablation. For 25 W, 10 min ablations at 5.8 GHz, the simulated S_{11} using the mean envelope yielded closer prediction to the measured S_{11} ($R = 0.87$). At other applied power levels and heating durations for both frequencies, the simulated S_{11} computed when using the lower envelope parameterization of the dielectric properties yielded better comparison to experimental measurements (R ranging between 0.83–0.92). The considerable differences in simulated transient temperature profiles as a function of the parameterization envelope (lower, mean, or upper), illustrates the impact of uncertainty in tissue dielectric properties on return loss. Accounting for the effects of this uncertainty in tissue dielectric properties may be of particular importance for the development of techniques for monitoring ablation zone growth. It is noted that the tissue samples used for the 5.8 GHz, 25 W, 10 min ablation were from one liver, while all the samples for the other ablations were from another liver. When using the mean envelope, models employing temperature dependent dielectric property variation yielded similar S_{11} profiles, as those employing thermal dose dependent dielectric properties (Figure 6-7).

Table 6-1: Correlation between the experimentally measured S_{11} and those simulated by the temperature and thermal isoeffective dose dependent dielectric properties of bovine liver at 2.45 and 5.8 GHz (shown in Figure 6-7).

Test	Temperature dependent			Thermal dose dependent		
	Lower env.	Mean env.	Upper env.	Lower env.	Mean env.	Upper env.
2.45 GHz, 25 W, 10 min	0.83	0.60	-0.43	0.90	0.56	-0.88
2.45 GHz, 40 W, 4 min	0.83	0.37	-0.62	0.92	0.22	-0.83
5.8 GHz, 25 W, 10 min	0.36	0.87	0.13	0.51	0.68	-0.09
5.8 GHz, 40 W, 4 min	0.89	0.01	-0.85	0.91	-0.45	-0.25

A limitation of this study is that the dielectric property measurements were conducted on *ex vivo* tissue. While it is ideal to characterize tissue properties *in vivo*, measuring tissue dielectric properties *in vivo* with invasive probes is a challenging task [202], [203], due to the additional uncertainties associated with blood in proximity to the dielectric probe. In our experiments, we pushed the probe ~5 mm onto the tissue. Recent studies demonstrate that the pressure applied by dielectric measurement probes on the tissue surface may alter the tissue water content, potentially contributing to variability of measured dielectric properties [204]. Further investigation of the probe-to-tissue contact pressure on dielectric properties of tissue during heating to ablative temperatures is warranted. Our *ex vivo* data is a step toward better understanding the broadband tissue dielectric properties over the ablative temperature range. Our study was further limited to measurements on normal liver tissue, which is a widely used benchtop experimental model for evaluating microwave ablation devices. Future studies investigating the dielectric properties of normal and malignant human liver would provide enhanced understanding of microwave energy interactions with tissue during clinical ablation procedures.

6.5 Conclusion

We have reported measurements of the broadband dielectric properties of *ex vivo* bovine liver over the frequency range 500 MHz to 6 GHz and temperature range 20 to 130

°C. We observed a sharp drop in both relative permittivity and effective conductivity in the temperature range of 89 to 107 °C similar to prior reports of dielectric properties at 2.45 GHz reported in the literature. The observed temperature-dependence of dielectric properties varied a function of temperature for each frequency. Dielectric properties did not vary appreciably when experiments were conducted at different heating rates (6.4 – 16.9 °C/min). Finally, piecewise functions modeling the measured dielectric properties of liver tissue were provided, and may serve as a foundation for more accurate modeling of microwave ablation applicators and systems.

7 Conclusion and Future Work

In this chapter, concluding remarks of this dissertation are provided as well as a summary of the results and suggestion for future research directions.

There has been considerable interest in the development of MW ablation technology for a range of clinical indications. In chapter 2, it was demonstrated that a critical component of MW ablation systems is the applicator, which includes an antenna for coupling applied MW power from a generator to the targeted tissue. We reviewed MW antennas designed for site-specific thermal ablation of tissue. Then, the use of active cooling strategies for minimizing unintended heating along the feeding transmission line and antenna chokes/sleeves and cooling for adjusting the length of ablation zones were discussed.

In chapter 3, we presented an applicator for treatment of menstrual heavy bleeding. The applicator employs a microwave loop antenna for global endometrial ablation enabling conformal ablation of uterine cavities of varying size in the range 4–6.5 cm in length and 2.5–4.5 cm in width, with a single positioning of the device. For treating large cavities, conformal microwave radiation was achieved by coupling the loop antenna with a passive element. A 3-D-coupled finite element method electromagnetic and heat transfer

simulator was employed to optimize the antenna geometry with the goal of maximizing return loss at the 915 MHz operating frequency, and achieving adequate ablation depths for a range of uterine cavity sizes. Proof-of-concept devices were fabricated and experimentally evaluated in *ex vivo* tissue. The simulated and measured return loss of the optimized design was 20 dB at 915 MHz. Experiments in *ex vivo* tissue demonstrated the ability of the presented device to achieve mean ablation depths of 7.3 mm. We demonstrated a technique for creating planar ablation patterns suitable for global endometrial ablation of different uterine cavity sizes by employing a loop antenna with a passive element. Our design provides a planar ablation pattern by using a loop antenna with a passive element that will allow for ablation applications not realizable with conventional coaxial monopole, dipole, and slot antennas.

A possible future research direction is to investigate employing the loop antenna for ablating pathologic tissue on the surface of body lumens, for example for treatment of Barrett's esophagus [205]. The loop antenna offers a planar ablation pattern, a wide heating pattern with shallow ablation depth. In the endometrial ablation application, the loop antenna is made of wire and formed into a triangle conformal to the anatomy of the uterine cavity. For treating targets on the surfaces of cylindrical body lumens, the loop antenna could be implemented on flexible substrate such as polyimide film with an optimized shape for creation of very shallow ablation depth.

In chapter 4, reflection coefficient was studied as a parameter for monitoring the ablation zone progress during the course of ablation. When using multiple antennas for thermal ablation, this method could be extended to incorporate electromagnetic assessment of several antennas within the system.

In chapter 5, Microwave thermal ablation was considered as a minimally invasive modality to treat 10–20 mm benign adrenal adenomas, while preserving normally functioning adjacent adrenal tissue, and returning the gland to a normally functioning status that is under normal regulation. In contrast to applications for tumor ablation, where devices have been developed with the objective of maximizing the size of the ablation zone for treating large tumors, a challenge for adrenal ablation was to minimize thermal damage to non-targeted adrenal tissue and thereby preserving adrenal function. We investigated methods for creating small spherical ablation zones of volumes in the range 0.5–4 cm^3 for the treatment of benign adrenal adenomas using water-loaded microwave monopole antennas operating at 2.45 GHz and 5.8 GHz. Coupled electromagnetic and bioheat transfer simulations and experiments in *ex vivo* tissue were employed to investigate the effect of frequency, applied power, ablation duration, and coolant temperature on the length and width of the ablation zone. Experimental results showed that small spherical ablation zones with diameters in the range of 7.4–17.6 mm could be obtained by adjusting the applied power and ablation duration. Multi-way ANOVA analysis of the experimentally-measured ablation zone dimensions demonstrated

that frequency of operation and ablation duration are the primary parameters for controlling the ablation zone length and width, respectively. Additionally, it was demonstrated that the coolant temperature provides another effective parameter for controlling the ablation zone length without affecting the ablation zone width. Our study demonstrated the feasibility of creating small spherical microwave ablation zones suitable for targeting benign adrenal adenomas.

In chapter 6, the goal was investigation of the thermal and frequency dependence of dielectric properties of *ex vivo* liver tissue – relative permittivity and effective conductivity – over the frequency range of 500 MHz to 6 GHz and temperatures ranging from 20 to 130 °C. We measured the dielectric properties of fresh *ex vivo* bovine liver tissue using the open-ended coaxial probe method (n = 15 samples). Numerical optimization techniques were utilized to obtain parametric models for characterizing changes in broadband dielectric properties as a function of temperature and thermal isoeffective dose. The effect of heating tissue at rates over the range 6.4–16.9 °C/min was studied. The measured dielectric properties were used in simulations of microwave ablation to assess changes in simulated antenna return loss compared to experimental measurements. Across all frequencies, both relative permittivity and effective conductivity dropped sharply over the temperature range 89 – 107 °C. Below 91 °C, the slope of the effective conductivity changed from positive values at lower frequencies (0.5–1.45 GHz) to negative values at higher frequencies (1.45–6 GHz). Comparison of simulated return

loss with measured results showed that temperature and thermal dose dependent dielectric properties functions lead to comparable results ($0.83<R<0.92$). The presented dielectric property models will contribute to the development of ablation systems operating at frequencies other than 2.45 GHz, as well as broadband techniques for monitoring growth of microwave ablation zones.

Here we presented the broadband temperature-dependent dielectric properties of *ex vivo* liver tissue. Although this dataset is beneficial for MW applicator and system development, there is still the need to repeat the same measurement on the tumor tissue as it usually has a different tissue structure and texture. Another follow-on effort would be to have a more realistic model to measure the broadband temperature-dependent dielectric properties of *in vivo* tissue in order to capture the effect of blood perfusion.

References

[1] C. L. Brace, "Radiofrequency and microwave ablation of the liver, lung, kidney, and bone: what are the differences?," *Curr. Probl. Diagn. Radiol.*, vol. 38, no. 3, pp. 135–143, 2009.

[2] E. S. Alexander and D. E. Dupuy, "Lung cancer ablation: technologies and techniques," in *Seminars in interventional radiology*, 2013, vol. 30, pp. 141–150.

[3] Y. Lin *et al.*, "Percutaneous microwave ablation of renal cell carcinoma is safe in patients with a solitary kidney," *Urology*, vol. 83, no. 2, pp. 357–363, 2014.

[4] A. Kelekis, F. H. Cornelis, S. Tutton, and D. Filippiadis, "Metastatic osseous pain control: bone ablation and cementoplasty," in *Seminars in interventional radiology*, 2017, vol. 34, pp. 328–336.

[5] O. Lodeizen *et al.*, "Ablation energies for focal treatment of prostate cancer," *World J. Urol.*, vol. 37, no. 3, pp. 409–418, 2019.

[6] A. H. Kim *et al.*, "Laser Ablation of Abnormal Neurological Tissue Using Robotic NeuroBlate System (LAANTERN): 12-Month Outcomes and Quality of Life After Brain Tumor Ablation," *Neurosurgery*, 2020.

[7] Z. Gu, C. M. Rappaport, P. J. Wang, and B. A. VanderBrink, "A 2 1/4-turn spiral antenna for catheter cardiac ablation," *IEEE Trans. Biomed. Eng.*, vol. 46, no. 12, pp. 1480–1482, 1999.

[8] J. Reeves, M. Birch, K. Munro, and R. Collier, "Investigation into the thermal distribution of microwave helical antennas designed for the treatment of Barrett's oesophagus," *Phys. Med. Biol.*, vol. 47, no. 19, p. 3557, 2002.

[9] D. A. Hodgson, I. B. Feldberg, N. Sharp, N. Cronin, M. Evans, and L. Hirschowitz, "Microwave endometrial ablation: development, clinical trials and outcomes at three years," *BJOG Int. J. Obstet. Gynaecol.*, vol. 106, no. 7, pp. 684–694, 1999.

[10] A. Andreano and C. L. Brace, "A comparison of direct heating during radiofrequency and microwave ablation in ex vivo liver," *Cardiovasc. Intervent. Radiol.*, vol. 36, no. 2, pp. 505–511, 2013.

[11] > Gail ter Haar and C. Coussios, "High intensity focused ultrasound: physical principles and devices," *Int. J. Hyperthermia*, vol. 23, no. 2, pp. 89–104, 2007.

[12] J. E. Kennedy, "High-intensity focused ultrasound in the treatment of solid tumours," *Nat. Rev. Cancer*, vol. 5, no. 4, p. 321, 2005.

[13] T. Lee, N. Mendhiratta, D. Sperling, and H. Lepor, "Focal laser ablation for localized prostate cancer: principles, clinical trials, and our initial experience," *Rev. Urol.*, vol. 16, no. 2, p. 55, 2014.

[14] U. Lindner, N. Lawrentschuk, and J. Trachtenberg, "Focal laser ablation for localized prostate cancer," *J. Endourol.*, vol. 24, no. 5, pp. 791–797, 2010.

[15] S. Tatli, M. Acar, K. Tuncali, P. R. Morrison, and S. Silverman, "Percutaneous cryoablation techniques and clinical applications," *Diagn. Interv. Radiol.*, vol. 16, no. 1, pp. 90–95, Mar. 2010, doi: http://dx.doi.org/10.4261/1305-3825.DIR.1922-08.0.

[16] J. G. Baust, A. A. Gage, and J. M. Baust, "Principles of cryoablation," in *Dermatological Cryosurgery and Cryotherapy*, Springer, 2016, pp. 9–16.

[17] P. G. Wagstaff *et al.*, "Irreversible electroporation: state of the art," *OncoTargets Ther.*, vol. 9, p. 2437, 2016.

[18] K. R. Thomson, H. Kavnoudias, and R. E. Neal II, "Introduction to irreversible electroporation—principles and techniques," *Tech. Vasc. Interv. Radiol.*, vol. 18, no. 3, pp. 128–134, 2015.

[19] J. Rehman, J. Landman, C. Sundaram, and R. V. Clayman, "Tissue chemoablation," *J. Endourol.*, vol. 17, no. 8, pp. 647–657, 2003.

[20] E. N. Cressman *et al.*, "Concentration and volume effects in thermochemical ablation in vivo: Results in a porcine model," *Int. J. Hyperthermia*, vol. 28, no. 2, pp. 113–121, 2012.

[21] J. M. Bertram, D. Yang, M. C. Converse, J. G. Webster, and D. M. Mahvi, "A review of coaxial-based interstitial antennas for hepatic microwave ablation," *Crit. Rev. Biomed. Eng.*, vol. 34, no. 3, 2006.

[22] H. Fallahi and P. Prakash, "Antenna designs for microwave tissue ablation," *Crit. Rev. Biomed. Eng.*, vol. 46, no. 6, 2018.

[23] H. Fallahi, J. Šebek, E. Frattura, J. Schenck, and P. Prakash, "Global microwave endometrial ablation for menorrhagia treatment," in *Proc. of SPIE Vol*, 2017, vol. 10066, pp. 100660K–1.

[24] H. Fallahi and P. Prakash, "Design of a Microwave Global Endometrial Ablation Device," *IEEE J. Electromagn. RF Microw. Med. Biol.*, 2019.

[25] P. Faridi, H. Fallahi, and P. Prakash, "Evaluation of the effect of uterine fibroids on microwave endometrial ablation profiles," in *2018 40th Annual International Conference of the IEEE Engineering in Medicine and Biology Society (EMBC)*, 2018, pp. 3236–3239.

[26] P. Prakash, "Microwave system for global endometrial ablation," WO2019241439A1, Dec. 19, 2019.

[27] H. Fallahi, A. Shahzad, D. Clausing, M. O'Halloran, M. C. Dennedy, and P. Prakash, "Technological requirements for microwave ablation of adrenal masses," in *Antennas and Propagation (EUCAP), 2017 11th European Conference on*, 2017, pp.

3713–3716, Accessed: Aug. 30, 2017. [Online]. Available: http://ieeexplore.ieee.org/abstract/document/7928268/.

[28] H. Fallahi, D. Clausing, A. Shahzad, M. O'Halloran, M. C. Dennedy, and P. Prakash, "Microwave antennas for thermal ablation of benign adrenal adenomas," *Biomed. Phys. Eng. Express*, vol. 5, no. 2, p. 025044, 2019.

[29] P. T. Donlon *et al.*, "Using microwave thermal ablation to develop a subtotal, cortical-sparing approach to the management of primary aldosteronism," *Int. J. Hyperthermia*, vol. 36, no. 1, pp. 905–914, 2019.

[30] H. Fallahi and P. Prakash, "Measurement of Broadband Temperature-Dependent Dielectric Properties of Liver Tissue," in *2018 IEEE International Microwave Biomedical Conference (IMBioC)*, 2018, pp. 91–93.

[31] H. Fallahi, J. Sebek, and P. Prakash, "Broadband Dielectric Properties of Ex Vivo Bovine Liver Tissue Characterized at Ablative Temperatures," *IEEE Trans. Biomed. Eng.*, Under review.

[32] K. F. Chu and D. E. Dupuy, "Thermal ablation of tumours: biological mechanisms and advances in therapy," *Nat. Rev. Cancer*, vol. 14, no. 3, p. 199, 2014.

[33] S. Rey and S. Levine, "An Overview of Cardiac Ablation," *J. Clin. Exerc. Physiol.*, vol. 6, no. 2, pp. 29–35, 2017.

[34] W. Verloop, M. Voskuil, and P. Doevendans, "Renal denervation: a new treatment option in resistant arterial hypertension," *Neth. Heart J.*, vol. 21, no. 2, pp. 95–98, 2013.

[35] G. W. Choby and P. H. Hwang, "Emerging roles of coblation in rhinology and skull base surgery," *Otolaryngol. Clin. North Am.*, vol. 50, no. 3, pp. 599–606, 2017.

[36] M. Ahmed, C. L. Brace, F. T. Lee Jr, and S. N. Goldberg, "Principles of and advances in percutaneous ablation," *Radiology*, vol. 258, no. 2, pp. 351–369, 2011.

[37] C. Jiang, R. V. Davalos, and J. C. Bischof, "A review of basic to clinical studies of irreversible electroporation therapy," *IEEE Trans. Biomed. Eng.*, vol. 62, no. 1, pp. 4–20, 2015.

[38] M. Burtnyk, T. Hill, H. Cadieux-Pitre, and I. Welch, "Magnetic resonance image guided transurethral ultrasound prostate ablation: a preclinical safety and feasibility study with 28-day followup," *J. Urol.*, vol. 193, no. 5, pp. 1669–1675, 2015.

[39] I. Fernández-Ruiz, "Renewed hopes for renal denervation in hypertension," *Nat. Rev. Cardiol.*, p. 1, 2018.

[40] J. Sebek *et al.*, "Feasibility Assessment of Microwave Ablation for Treating Esophageal Varices," *J. Med. Devices*, vol. 11, no. 3, p. 031013, 2017.

[41] J. A. Pearce, "Models for thermal damage in tissues: processes and applications," *Crit. Rev. Biomed. Eng.*, vol. 38, no. 1, 2010.

[42] A. Osaka, "Use of microwave radiation in surgery and cancer therapy," *J. Microw. Power*, vol. 13, no. 2, pp. 155–161, 1978.

[43] A. P. O'Rourke, D. Haemmerich, P. Prakash, M. C. Converse, D. M. Mahvi, and J. G. Webster, "Current status of liver tumor ablation devices," *Expert Rev. Med. Devices*, vol. 4, no. 4, pp. 523–537, 2007.

[44] K. Saito, S. Hosaka, S. Okabe, H. Yoshimura, and K. Ito, "A proposition on improvement of a heating pattern of an antenna for microwave coagulation therapy: Introduction of a coaxial-dipole antenna," *Electron. Commun. Jpn. Part Commun.*, vol. 86, no. 1, pp. 16–23, 2003.

[45] D. Yang *et al.*, "A floating sleeve antenna yields localized hepatic microwave ablation," *IEEE Trans. Biomed. Eng.*, vol. 53, no. 3, pp. 533–537, 2006.

[46] R. D. Nevels, G. D. Arndt, G. W. Raffoul, J. R. Carl, and A. Pacifico, "Microwave catheter design," *IEEE Trans. Biomed. Eng.*, vol. 45, no. 7, pp. 885–890, 1998.

[47] H. Luyen, S. C. Hagness, and N. Behdad, "A balun-free helical antenna for minimally invasive microwave ablation," *IEEE Trans. Antennas Propag.*, vol. 63, no. 3, pp. 959–965, 2015.

[48] H. Luyen, S. C. Hagness, and N. Behdad, "Reduced-Diameter Designs of Coax-Fed Microwave Ablation Antennas Equipped With Baluns," *IEEE Antennas Wirel. Propag. Lett.*, vol. 16, pp. 1385–1388, 2017.

[49] H. Luyen, S. C. Hagness, and N. Behdad, "A Minimally Invasive Coax-Fed Microwave Ablation Antenna With a Tapered Balun," *IEEE Trans. Antennas Propag.*, vol. 65, no. 12, pp. 7280–7287, 2017.

[50] B. T. McWilliams, E. E. Schnell, S. Curto, T. M. Fahrbach, and P. Prakash, "A directional interstitial antenna for microwave tissue ablation: Theoretical and experimental investigation," *IEEE Trans. Biomed. Eng.*, vol. 62, no. 9, pp. 2144–2150, 2015.

[51] Y. Mohtashami, S. C. Hagness, and N. Behdad, "A Hybrid Slot/Monopole Antenna With Directional Heating Patterns for Microwave Ablation," *IEEE Trans. Antennas Propag.*, vol. 65, no. 8, pp. 3889–3896, 2017.

[52] B. S. Trembly and R. H. Keates, "Combined microwave heating and surface cooling of the cornea," *IEEE Trans. Biomed. Eng.*, vol. 38, no. 1, pp. 85–91, 1991.

[53] E. Jerby, V. Dikhtyar, O. Aktushev, and U. Grosglick, "The microwave drill," *Science*, vol. 298, no. 5593, pp. 587–589, 2002.

[54] K. Kwon *et al.*, "Planar type probe with multiple-polarization response for in-vivo permittivity measurements of heterogeneous biological tissues," *IEEE Microw. Wirel. Compon. Lett.*, vol. 16, no. 1, pp. 1–3, 2006.

[55] J. Yoon *et al.*, "High-frequency microwave ablation method for enhanced cancer treatment with minimized collateral damage," *Int. J. Cancer*, vol. 129, no. 8, pp. 1970–1978, 2011.

[56] C. L. Brace, "Microwave tissue ablation: biophysics, technology, and applications," *Crit. Rev. Biomed. Eng.*, vol. 38, no. 1, 2010, Accessed: Dec. 18, 2016. [Online]. Available: http://www.dl.begellhouse.com/journals/4b27cbfc562e21b8,41996af914259394,6941e0586b165112.html.

[57] P. Prakash, "Theoretical modeling for hepatic microwave ablation," *Open Biomed. Eng. J.*, vol. 4, p. 27, 2010.

[58] S. Gabriel, R. W. Lau, and C. Gabriel, "The dielectric properties of biological tissues: II. Measurements in the frequency range 10 Hz to 20 GHz," *Phys. Med. Biol.*, vol. 41, no. 11, p. 2251, 1996.

[59] G. Deshazer, M. Hagmann, D. Merck, J. Sebek, K. B. Moore, and P. Prakash, "Computational modeling of 915 MHz microwave ablation: comparative assessment of temperature-dependent tissue dielectric models," *Med. Phys.*, 2017.

[60] H. Luyen, F. Gao, S. C. Hagness, and N. Behdad, "Microwave ablation at 10.0 GHz achieves comparable ablation zones to 1.9 GHz in ex vivo bovine liver," *IEEE Trans. Biomed. Eng.*, vol. 61, no. 6, pp. 1702–1710, 2014.

[61] C. Hancock, N. Dharmasiri, C. I. Duff, and M. White, "New microwave antenna structures for treating gastro-oesophageal reflux disease (GERD)," *IEEE Trans. Microw. Theory Tech.*, vol. 61, no. 5, pp. 2242–2252, 2013.

[62] C. P. Hancock, N. Dharmasiri, M. White, and A. M. Goodman, "The design and development of an integrated multi-functional microwave antenna structure for biological applications," *IEEE Trans. Microw. Theory Tech.*, vol. 61, no. 5, pp. 2230–2241, 2013.

[63] J. F. Sawicki, J. D. Shea, N. Behdad, and S. C. Hagness, "The impact of frequency on the performance of microwave ablation," *Int. J. Hyperthermia*, vol. 33, no. 1, pp. 61–68, 2017.

[64] V. V. Komarov, "Numerical study and optimization of interstitial antennas for microwave ablation therapy," *Eur. Phys. J.-Appl. Phys.*, vol. 68, no. 1, 2014.

[65] M. Y. Bongers, "Second-generation endometrial ablation treatment: Novasure," *Best Pract. Res. Clin. Obstet. Gynaecol.*, vol. 21, no. 6, pp. 989–994, 2007.

[66] M. Kuang *et al.*, "Liver cancer: increased microwave delivery to ablation zone with cooled-shaft antenna--experimental and clinical studies," *Radiology*, vol. 242, no. 3, pp. 914–924, Mar. 2007, doi: 10.1148/radiol.2423052028.

[67] E. M. Knavel *et al.*, "High-powered gas-cooled microwave ablation: shaft cooling creates an effective stick function without altering the ablation zone," *Am. J. Roentgenol.*, vol. 198, no. 3, pp. W260–W265, 2012.

[68] P. Prakash, G. Deng, M. C. Converse, J. G. Webster, D. M. Mahvi, and M. C. Ferris, "Design optimization of a robust sleeve antenna for hepatic microwave ablation," *Phys. Med. Biol.*, vol. 53, no. 4, p. 1057, 2008.

[69] P. R. Stauffer, F. Rossetto, M. Prakash, D. G. Neuman, and T. Lee, "Phantom and animal tissues for modelling the electrical properties of human liver," *Int. J. Hyperthermia*, vol. 19, no. 1, pp. 89–101, 2003.

[70] A. Dabbagh, B. J. J. Abdullah, C. Ramasindarum, and N. H. Abu Kasim, "Tissue-mimicking gel phantoms for thermal therapy studies," *Ultrason. Imaging*, vol. 36, no. 4, pp. 291–316, 2014.

[71] T. P. Ryan, "Comparison of six microwave antennas for hyperthermia treatment of cancer: SAR results for single antennas and arrays," *Int. J. Radiat. Oncol. Biol. Phys.*, vol. 21, no. 2, pp. 403–413, 1991.

[72] G. Deshazer, P. Prakash, D. Merck, and D. Haemmerich, "Experimental measurement of microwave ablation heating pattern and comparison to computer simulations," *Int. J. Hyperthermia*, vol. 33, no. 1, pp. 74–82, 2017.

[73] C. L. Brace, P. F. Laeseke, D. W. van der Weide, and F. T. Lee, "Microwave ablation with a triaxial antenna: results in ex vivo bovine liver," *IEEE Trans. Microw. Theory Tech.*, vol. 53, no. 1, pp. 215–220, 2005.

[74] J. F. Sawicki, H. Luyen, Y. Mohtashami, J. D. Shea, N. Behdad, and S. C. Hagness, "The Performance of Higher-Frequency Microwave Ablation in the Presence of Perfusion," *IEEE Trans. Biomed. Eng.*, 2018.

[75] W. Hurter, F. Reinbold, and W. J. Lorenz, "A dipole antenna for interstitial microwave hyperthermia," *IEEE Trans. Microw. Theory Tech.*, vol. 39, no. 6, pp. 1048–1054, 1991.

[76] S. Labonte, A. Blais, S. R. Legault, H. O. Ali, and L. Roy, "Monopole antennas for microwave catheter ablation," *IEEE Trans. Microw. Theory Tech.*, vol. 44, no. 10, pp. 1832–1840, 1996.

[77] L. Hamada, K. Saito, H. Yoshimura, and K. Ito, "Dielectric-loaded coaxial-slot antenna for interstitial microwave hyperthermia: longitudinal control of heating patterns," *Int. J. Hyperthermia*, vol. 16, no. 3, pp. 219–229, 2000.

[78] R. W. King, B. Trembly, and J. Strohbehn, "The electromagnetic field of an insulated antenna in a conducting or dielectric medium," *IEEE Trans. Microw. Theory Tech.*, vol. 31, no. 7, pp. 574–583, 1983.

[79] J. C. Lin and Y.-J. Wang, "The cap-choke catheter antenna for microwave ablation treatment," *IEEE Trans. Biomed. Eng.*, vol. 43, no. 6, pp. 657–660, 1996.

[80] S. Pisa, M. Cavagnaro, P. Bernardi, and J. C. Lin, "A 915-MHz antenna for microwave thermal ablation treatment: physical design, computer modeling and experimental measurement," *IEEE Trans. Biomed. Eng.*, vol. 48, no. 5, pp. 599–601, 2001.

[81] H.-M. Chiu, A. S. Mohan, A. R. Weily, D. J. Guy, and D. L. Ross, "Analysis of a novel expanded tip wire (ETW) antenna for microwave ablation of cardiac arrhythmias," *IEEE Trans. Biomed. Eng.*, vol. 50, no. 7, pp. 890–899, 2003.

[82] P. Prakash, M. C. Converse, J. G. Webster, and D. M. Mahvi, "An optimal sliding choke antenna for hepatic microwave ablation," *IEEE Trans. Biomed. Eng.*, vol. 56, no. 10, pp. 2470–2476, 2009.

[83] I. Longo, G. B. Gentili, M. Cerretelli, and N. Tosoratti, "A coaxial antenna with miniaturized choke for minimally invasive interstitial heating," *IEEE Trans. Biomed. Eng.*, vol. 50, no. 1, pp. 82–88, 2003.

[84] M. Cavagnaro, C. Amabile, P. Bernardi, S. Pisa, and N. Tosoratti, "A minimally invasive antenna for microwave ablation therapies: design, performances, and experimental assessment," *IEEE Trans. Biomed. Eng.*, vol. 58, no. 4, pp. 949–959, 2011.

[85] K. Ito, M. Hyodo, M. Shimura, and H. Kasai, "Thin applicator having coaxial ring slots for interstitial microwave hyperthermia," in *Antennas and Propagation Society International Symposium, 1990. AP-S. Merging Technologies for the 90's. Digest.*, 1990, pp. 1233–1236.

[86] K. Saito, H. Yoshimura, K. Ito, Y. Aoyagi, and H. Horita, "Clinical trials of interstitial microwave hyperthermia by use of coaxial-slot antenna with two slots," *IEEE Trans. Microw. Theory Tech.*, vol. 52, no. 8, pp. 1987–1991, 2004.

[87] C. L. Brace, "Dual-slot antennas for microwave tissue heating: Parametric design analysis and experimental validation," *Med. Phys.*, vol. 38, no. 7, pp. 4232–4240, 2011.

[88] J. Chiang, K. A. Hynes, M. Bedoya, and C. L. Brace, "A dual-slot microwave antenna for more spherical ablation zones: ex vivo and in vivo validation," *Radiology*, vol. 268, no. 2, pp. 382–389, 2013.

[89] D. Kitchin *et al.*, "Microwave ablation of malignant hepatic tumours: intraperitoneal fluid instillation prevents collateral damage and allows more aggressive case selection," *Int. J. Hyperthermia*, vol. 30, no. 5, pp. 299–305, 2014.

[90] J. Sebek, S. Curto, R. Bortel, and P. Prakash, "Analysis of minimally invasive directional antennas for microwave tissue ablation," *Int. J. Hyperthermia*, vol. 33, no. 1, pp. 51–60, 2017.

[91] C. A. Balanis, "Antenna theory: A review," *Proc. IEEE*, vol. 80, no. 1, pp. 7–23, 1992.

[92] T. Satoh and P. R. Stauffer, "Implantable helical coil microwave antenna for interstitial hyperthermia," *Int. J. Hyperthermia*, vol. 4, no. 5, pp. 497–512, 1988.

[93] M. S. Mirotznik, N. Engheta, and K. R. Foster, "Heating characteristics of thin helical antennas with conducting cores in a lossy medium. I. Noninsulated antennas," *IEEE Trans. Microw. Theory Tech.*, vol. 41, no. 11, pp. 1878–1886, 1993.

[94] R. L. Liu, E. Y. Zhang, E. J. Gross, and T. C. Cetas, "Heating pattern of helical microwave intracavitary oesophageal applicator," *Int. J. Hyperthermia*, vol. 7, no. 4, pp. 577–586, 1991.

[95] J. J. LANGBERG, T. WONNELL, M. C. CHIN, W. FINKBEINER, M. SCHEINMAN, and P. STAUFFER, "Catheter ablation of the atrioventricular junction using a helical microwave antenna: A novel means of coupling energy to the endocardium," *Pacing Clin. Electrophysiol.*, vol. 14, no. 12, pp. 2105–2113, 1991.

[96] Z. Gu, M. Rappaport, P. J. Wang, and B. A. VanderBrink, "Development and experimental verification of the wide-aperture catheter-based microwave cardiac ablation antenna," *IEEE Trans. Microw. Theory Tech.*, vol. 48, no. 11, pp. 1892–1900, 2000.

[97] M. L. Swicord and C. C. Davis, "Energy absorption from small radiating coaxial probes in lossy media," *IEEE Trans. Microw. Theory Tech.*, vol. 29, no. 11, pp. 1202–1209, 1981.

[98] Y. Eshet, R. R. Mann, A. Anaton, T. Yacoby, A. Gefen, and E. Jerby, "Microwave drilling of bones," *IEEE Trans. Biomed. Eng.*, vol. 53, no. 6, pp. 1174–1182, 2006.

[99] E. Colebeck and E. Topsakal, "Ultra-wideband Microwave Ablation Therapy (UMAT)," in *Microwave Symposium Digest (IMS), 2013 IEEE MTT-S International*, 2013, pp. 1–3.

[100] K. Kim *et al.*, "A Ku-band miniaturized microwave ablation system integrated on a micromachined silicon applicator," in *Microwave Symposium Digest (IMS), 2013 IEEE MTT-S International*, 2013, pp. 1–4.

[101] C. Reimann *et al.*, "Planar microwave sensor for theranostic therapy of organic tissue based on oval split ring resonators," *Sensors*, vol. 16, no. 9, p. 1450, 2016.

[102] S. Sharma and C. D. Sarris, "Inversely-designed printed microwave ablation antenna for controlled temperature profile synthesis," *J. Appl. Phys.*, vol. 121, no. 7, p. 074701, 2017.

[103] C. P. Hancock *et al.*, "A new wave in electrosurgery: A review of existing and introduction to new radio-frequency and microwave therapeutic systems," *IEEE Microw. Mag.*, vol. 16, no. 2, pp. 14–30, 2015.

[104] P.-Y. Cresson, C. Ricard, N. Bernardin, L. Dubois, and J. Pribetich, "Design and modeling of a specific microwave applicator for the treatment of snoring," *IEEE Trans. Microw. Theory Tech.*, vol. 54, no. 1, pp. 302–308, 2006.

[105] K. Meredith, F. Lee, M. B. Henry, T. Warner, and D. Mahvi, "Microwave ablation of hepatic tumors using dual-loop probes: results of a phase I clinical trial," *J. Gastrointest. Surg.*, vol. 9, no. 9, pp. 1354–1360, 2005.

[106] P. Qian *et al.*, "A novel microwave catheter can perform noncontact circumferential endocardial ablation in a model of pulmonary vein isolation," *J. Cardiovasc. Electrophysiol.*, vol. 26, no. 7, pp. 799–804, 2015.

[107] S. A. Shock *et al.*, "Microwave ablation with loop antenna: in vivo porcine liver model," *Radiology*, vol. 231, no. 1, pp. 143–149, 2004.

[108] S. Meeson, J. Reeves, M. Birch, C. Swain, K. Ikeda, and R. Feakins, "Preliminary findings from tests of a microwave applicator designed to treat Barrett's oesophagus," *Phys. Med. Biol.*, vol. 50, no. 19, p. 4553, 2005.

[109] P. C. Qian *et al.*, "Transcatheter non-contact microwave ablation may enable circumferential renal artery denervation while sparing the vessel intima and media.," *EuroIntervention J. Eur. Collab. Work. Group Interv. Cardiol. Eur. Soc. Cardiol.*, vol. 12, no. 15, pp. e1907–e1915, 2017.

[110] H. Rosen, A. Rosen, and P. Walinsky, "Microwave balloon systems in medicine," *IEEE Pulse*, vol. 1, no. 2, pp. 8–15, 2010.

[111] T. Livraghi *et al.*, "Hepatocellular carcinoma: radio-frequency ablation of medium and large lesions," *Radiology*, vol. 214, no. 3, pp. 761–768, 2000.

[112] M. D. Sherar, A. S. Gladman, S. R. Davidson, J. Trachtenberg, and M. R. Gertner, "Helical antenna arrays for interstitial microwave thermal therapy for prostate cancer: tissue phantom testing and simulations for treatment," *Phys. Med. Biol.*, vol. 46, no. 7, p. 1905, 2001.

[113] C. J. Simon *et al.*, "Intraoperative triple antenna hepatic microwave ablation," *Am. J. Roentgenol.*, vol. 187, no. 4, pp. W333–W340, 2006.

[114] V. Kumar, R. Chodankar, and J. K. Gupta, "Endometrial Ablation for Heavy Menstrual Bleeding," *Womens Health*, vol. 12, no. 1, pp. 45–52, Jan. 2016, doi: 10.2217/whe.15.86.

[115] H. T. Sharp, "Assessment of new technology in the treatment of idiopathic menorrhagia and uterine leiomyomata," *Obstet. Gynecol.*, vol. 108, no. 4, pp. 990–1003, 2006.

[116] S. J. Leathersich and P. M. McGurgan, "Endometrial resection and global ablation in the normal uterus," *Best Pract. Res. Clin. Obstet. Gynaecol.*, vol. 46, pp. 84–98, Jan. 2018, doi: 10.1016/j.bpobgyn.2017.09.006.

[117] J. Garza-Leal, I. Hernandez, L. Castillo, M. L. Jessop, N. Chill, and J. E. Coad, "Successful vapor-based endometrial ablation: in vivo peri-hysterectomy study," *J. Minim. Invasive Gynecol.*, vol. 18, no. 4, pp. 445–448, 2011.

[118] "NovaSure Impedance Controlled Endometrial Ablation System -- P010013," p. 21.

[119] G. H. Lipscomb, "Endometrial Ablation," *Glob. Libr. Womentextquotesingles Med.*, 2009, doi: 10.3843/glowm.10024.

[120] N. Goldstuck, "Assessment of uterine cavity size and shape: a systematic review addressing relevance to intrauterine procedures and events," *Afr. J. Reprod. Health*, vol. 16, no. 3, pp. 129–138, 2012.

[121] V. Saadat, *Heated balloon having a reciprocating fluid agitator*. Google Patents, 1998.

[122] S. L. Corson, "A multicenter evaluation of endometrial ablation by Hydro ThermAblator and rollerball for treatment of menorrhagia," *J. Am. Assoc. Gynecol. Laparosc.*, vol. 8, no. 3, pp. 359–367, 2001.

[123] N. R. van der Walt, J. H. Xiao, and D. W. Vancelette, *Cryosurgical devices for endometrial ablation*. Google Patents, 2008.

[124] M. Wortman, A. Cholkeri, A. M. McCausland, and V. M. McCausland, "Late-onset Endometrial Ablation Failure—Etiology, Treatment, and Prevention," *J. Minim. Invasive Gynecol.*, vol. 22, no. 3, pp. 323–331, 2015.

[125] Y. Kanaoka, K. Hirai, and O. Ishiko, "Microwave endometrial ablation for an enlarged uterus," *Arch. Gynecol. Obstet.*, vol. 269, no. 1, pp. 30–32, 2003.

[126] C. Pusceddu, B. Sotgia, R. M. Fele, and L. Melis, "Treatment of bone metastases with microwave thermal ablation," *J. Vasc. Interv. Radiol.*, vol. 24, no. 2, pp. 229–233, 2013.

[127] T. P. Ryan and C. L. Brace, "Interstitial microwave treatment for cancer: historical basis and current techniques in antenna design and performance," *Int. J. Hyperthermia*, vol. 33, no. 1, pp. 3–14, 2017.

[128] G. Schaller, J. Erb, and R. Engelbrecht, "Field simulation of dipole antennas for interstitial microwave hyperthermia," *IEEE Trans. Microw. Theory Tech.*, vol. 44, no. 6, pp. 887–895, 1996.

[129] F. H. Martini and E. F. Bartholomew, *Essentials of Anatomy & Physiology*, 6th edition. Boston: Pearson, 2012.

[130] R. W. King, B. S. Trembly, and J. W. Strohbehn, "The electromagnetic field of an insulated antenna in a conducting or dielectric medium," *IEEE Trans. Microw. Theory Tech.*, vol. 31, no. 7, pp. 574–583, 1983.

[131] H. Kawakami and T. Ohira, "Electrically steerable passive array radiator (ESPAR) antennas," *IEEE Antennas Propag. Mag.*, vol. 47, no. 2, pp. 43–50, 2005.

[132] K. Q. Da Costa, V. Dmitriev, D. C. Nascimento, and J. da S. Lacava, "Broadband L-probe fed patch antenna combined with passive loop elements," *IEEE Antennas Wirel. Propag. Lett.*, vol. 6, pp. 100–102, 2007.

[133] R. H. Phillion and M. Okoniewski, "Lenses for circular polarization using planar arrays of rotated passive elements," *IEEE Trans. Antennas Propag.*, vol. 59, no. 4, pp. 1217–1227, 2011.

[134] H. H. Pennes, "Analysis of tissue and arterial blood temperatures in the resting human forearm," *J. Appl. Physiol.*, vol. 1, no. 2, pp. 93–122, 1948.

[135] S. A. Baldwin, A. Pelman, and J. L. Bert, "A heat transfer model of thermal balloon endometrial ablation," *Ann. Biomed. Eng.*, vol. 29, no. 11, pp. 1009–1018, 2001.

[136] Z. Ji and C. L. Brace, "Expanded modeling of temperature-dependent dielectric properties for microwave thermal ablation," *Phys. Med. Biol.*, vol. 56, no. 16, p. 5249, 2011.

[137] S. K. Hall, E. H. Ooi, and S. J. Payne, "Cell death, perfusion and electrical parameters are critical in models of hepatic radiofrequency ablation," *Int. J. Hyperthermia*, vol. 31, no. 5, pp. 538–550, 2015.

[138] J. A. Pearce, "Relationship between Arrhenius models of thermal damage and the CEM 43 thermal dose," in *Energy-based Treatment of Tissue and Assessment V*, 2009, vol. 7181, p. 718104.

[139] H. Fallahi, J. Šebek, E. Frattura, J. Schenck, and P. Prakash, "Global microwave endometrial ablation for menorrhagia treatment," in *Proc. of SPIE Vol*, 2017, vol. 10066, pp. 100660K–1, Accessed: Aug. 30, 2017. [Online]. Available: http://proceedings.spiedigitallibrary.org/pdfaccess.ashx?url=/data/conferences/spiep/91624/100660k.pdf.

[140] K. Shroff, C. Y. Chu, D. I. Mody, C. Emmons, and A. J. Walke, *Methods and devices for applying energy to bodily tissues*. Google Patents, 2015.

[141] T. W. Duerig, A. Pelton, and D. Stöckel, "An overview of nitinol medical applications," *Mater. Sci. Eng. A*, vol. 273, pp. 149–160, 1999.

[142] R. Pearson, S. A. Daniel, D. J. Balbierz, K. S. Lee, J. Liang, and M. Getaneh, "Tissue ablation apparatus and method," Jan. 2007.

[143] X. Yu *et al.*, "Comparison of contrast enhanced ultrasound and contrast enhanced CT or MRI in monitoring percutaneous thermal ablation procedure in patients with hepatocellular carcinoma: a multi-center study in China," *Ultrasound Med. Biol.*, vol. 33, no. 11, pp. 1736–1749, 2007.

[144] S. Garrean *et al.*, "Ultrasound monitoring of a novel microwave ablation (MWA) device in porcine liver: lessons learned and phenomena observed on ablative effects

near major intrahepatic vessels," *J. Gastrointest. Surg.*, vol. 13, no. 2, pp. 334–340, 2009.

[145] P. Liang *et al.*, "Practice guidelines for ultrasound-guided percutaneous microwave ablation for hepatic malignancy," *World J. Gastroenterol. WJG*, vol. 19, no. 33, p. 5430, 2013.

[146] Y. Kurumi *et al.*, "MR-guided microwave ablation for malignancies," *Int. J. Clin. Oncol.*, vol. 12, no. 2, pp. 85–93, 2007.

[147] G. P. Rossi *et al.*, "A Prospective Study of the Prevalence of Primary Aldosteronism in 1,125 Hypertensive Patients," *J. Am. Coll. Cardiol.*, vol. 48, no. 11, pp. 2293–2300, Dec. 2006, doi: 10.1016/j.jacc.2006.07.059.

[148] P. Milliez, X. Girerd, P.-F. Plouin, J. Blacher, M. E. Safar, and J.-J. Mourad, "Evidence for an increased rate of cardiovascular events in patients with primary aldosteronism," *J. Am. Coll. Cardiol.*, vol. 45, no. 8, pp. 1243–1248, 2005.

[149] W. F. Young, "Primary aldosteronism: renaissance of a syndrome," *Clin. Endocrinol. (Oxf.)*, vol. 66, no. 5, pp. 607–618, May 2007, doi: 10.1111/j.1365-2265.2007.02775.x.

[150] M. Boscaro, V. Ronconi, F. Turchi, and G. Giacchetti, "Diagnosis and management of primary aldosteronism," *Curr. Opin. Endocrinol. Diabetes Obes.*, vol. 15, no. 4, pp. 332–338, Aug. 2008, doi: 10.1097/MED.0b013e3283060a40.

[151] P. R. Stauffer, "Evolving technology for thermal therapy of cancer," *Int. J. Hyperthermia*, vol. 21, no. 8, pp. 731–744, 2005.

[152] C. J. Diederich, "Thermal ablation and high-temperature thermal therapy: overview of technology and clinical implementation," *Int. J. Hyperthermia*, vol. 21, no. 8, pp. 745–753, 2005.

[153] M.-H. Yang, Y.-S. Tyan, Y.-H. Huang, S.-C. Wang, and S.-L. Chen, "Comparison of radiofrequency ablation versus laparoscopic adrenalectomy for benign aldosterone-producing adenoma," *Radiol. Med. (Torino)*, vol. 121, no. 10, pp. 811–819, Oct. 2016, doi: 10.1007/s11547-016-0662-1.

[154] S. Curto, M. Taj-Eldin, D. Fairchild, and P. Prakash, "Microwave ablation at 915 MHz vs 2.45 GHz: A theoretical and experimental investigation," *Med. Phys.*, vol. 42, no. 11, pp. 6152–6161, Nov. 2015, doi: 10.1118/1.4931959.

[155] R. Hoffmann *et al.*, "Comparison of four microwave ablation devices: an experimental study in ex vivo bovine liver," *Radiology*, vol. 268, no. 1, pp. 89–97, Jul. 2013, doi: 10.1148/radiol.13121127.

[156] R. C. Ward, T. T. Healey, and D. E. Dupuy, "Microwave ablation devices for interventional oncology," *Expert Rev. Med. Devices*, vol. 10, no. 2, pp. 225–238, Mar. 2013, doi: 10.1586/erd.12.77.

[157] I. B. Feldberg and N. J. Cronin, "A 9.2 GHz microwave applicator for the treatment of menorrhagia," in *1998 IEEE MTT-S International Microwave Symposium Digest (Cat. No.98CH36192)*, Jun. 1998, vol. 2, pp. 755–758 vol.2, doi: 10.1109/MWSYM.1998.705100.

[158] C. L. Brace *et al.*, "Microwave Ablation with a Single Small-Gauge Triaxial Antenna: In Vivo Porcine Liver Model 1," *Radiology*, vol. 242, no. 2, 2007.

[159] F. J. Wolf, D. E. Dupuy, J. T. Machan, and W. W. Mayo-Smith, "Adrenal neoplasms: effectiveness and safety of CT-guided ablation of 23 tumors in 22 patients," *Eur. J. Radiol.*, vol. 81, no. 8, pp. 1717–1723, 2012.

[160] X. Li *et al.*, "CT-guided percutaneous microwave ablation of adrenal malignant carcinoma: Preliminary results," *Cancer*, vol. 117, no. 22, pp. 5182–5188, 2011.

[161] Y. Wang, P. Liang, X. Yu, Z. Cheng, J. Yu, and J. Dong, "Ultrasound-guided percutaneous microwave ablation of adrenal metastasis: preliminary results," *Int. J. Hyperthermia*, vol. 25, no. 6, pp. 455–461, 2009.

[162] T. Kigure, T. Harada, Y. Satoh, N. Fujieda, and Y. Wakayama, "Microwave ablation of the adrenal gland: experimental study and clinical application," *Br. J. Urol.*, vol. 77, no. 2, pp. 215–220, 1996.

[163] P. T. Donlon *et al.*, "Tackling hypertension via adrenal ablation-the development of novel immunohistochemical ablation biomarkers."

[164] G. Zorbas and T. Samaras, "Parametric study of radiofrequency ablation in the clinical practice with the use of two-compartment numerical models," *Electromagn. Biol. Med.*, vol. 32, no. 2, pp. 236–243, 2013.

[165] E. Y. K. Ng and M. Jamil, "Parametric sensitivity analysis of radiofrequency ablation with efficient experimental design," *Int. J. Therm. Sci.*, vol. 80, pp. 41–47, 2014.

[166] A. Sarwar *et al.*, "Clinical outcomes following percutaneous radiofrequency ablation of unilateral aldosterone-producing adenoma: comparison with adrenalectomy," *J. Vasc. Interv. Radiol.*, vol. 27, no. 7, pp. 961–967, 2016.

[167] "ITU Radio Regulations, CHAPTER II – Frequencies, ARTICLE 5 Frequency allocations, Section IV – Table of Frequency Allocations." .

[168] G. Ruvio, J. Eaton-Evans, A. Shahzad, and M. O'Halloran, "Numerical evaluation of microwave thermal ablation to treat small adrenocortical masses," *Int. J. RF Microw. Comput.-Aided Eng.*, vol. 28, no. 3, p. e21236, 2018.

[169] M. Cavagnaro, R. Pinto, and V. Lopresto, "Numerical models to evaluate the temperature increase induced by ex vivo microwave thermal ablation," *Phys. Med. Biol.*, vol. 60, no. 8, p. 3287, 2015.

[170] P. A. Hasgall *et al.*, *IT'IS Database for thermal and electromagnetic parameters of biological tissues. Version 3.0, September 1st. 2015.* .

[171] A. Shahzad, D. Clausing, P. Prakash, M. C. Dennedy, and M. O'halloran, "Broadband dielectric properties of adrenal gland for accurate anatomical modelling in medical applications," in *Electromagnetics in Advanced Applications (ICEAA), 2017 International Conference on*, 2017, pp. 1465–1468.

[172] V. Lopresto, R. Pinto, G. A. Lovisolo, and M. Cavagnaro, "Changes in the dielectric properties of ex vivo bovine liver during microwave thermal ablation at 2.45 GHz," *Phys. Med. Biol.*, vol. 57, no. 8, p. 2309, 2012.

[173] C. Rossmann and D. Haemmerich, "Review of temperature dependence of thermal properties, dielectric properties, and perfusion of biological tissues at hyperthermic and ablation temperatures," *Crit. Rev. Biomed. Eng.*, vol. 42, no. 6, 2014.

[174] T. Herbold, R. Wahba, C. Bangard, M. Demir, U. Drebber, and D. L. Stippel, "The laparoscopic approach for radiofrequency ablation of hepatocellular carcinoma—indication, technique and results," *Langenbecks Arch. Surg.*, vol. 398, no. 1, pp. 47–53, 2013.

[175] J. Yu, P. Liang, X. Yu, Z. Cheng, Z. Han, and B. Dong, "Needle track seeding after percutaneous microwave ablation of malignant liver tumors under ultrasound guidance: analysis of 14-year experience with 1462 patients at a single center," *Eur. J. Radiol.*, vol. 81, no. 10, pp. 2495–2499, 2012.

[176] T. Nguyen, E. Hattery, and V. P. Khatri, "Radiofrequency ablation and breast cancer: a review," *Gland Surg.*, vol. 3, no. 2, p. 128, 2014.

[177] M. F. Marqa, S. Mordon, and N. Betrouni, "Laser interstitial thermotherapy of small breast fibroadenomas: Numerical simulations," *Lasers Surg. Med.*, vol. 44, no. 10, pp. 832–839, 2012.

[178] O. Adeyanju, H. Al-Angari, and A. Sahakian, "The optimization of needle electrode number and placement for irreversible electroporation of hepatocellular carcinoma," *Radiol. Oncol.*, vol. 46, no. 2, pp. 126–135, 2012.

[179] C. Rappaport, "Cardiac tissue ablation with catheter-based microwave heating," *Int. J. Hyperthermia*, vol. 20, no. 7, pp. 769–780, 2004.

[180] J. Sebek, N. Albin, R. Bortel, B. Natarajan, and P. Prakash, "Sensitivity of microwave ablation models to tissue biophysical properties: A first step toward probabilistic modeling and treatment planning," *Med. Phys.*, vol. 43, no. 5, p. 2649, May 2016, doi: 10.1118/1.4947482.

[181] J. L. Schepps and K. R. Foster, "The UHF and microwave dielectric properties of normal and tumour tissues: variation in dielectric properties with tissue water content," *Phys. Med. Biol.*, vol. 25, no. 6, p. 1149, 1980.

[182] D. Yang, M. C. Converse, D. M. Mahvi, and J. G. Webster, "Measurement and analysis of tissue temperature during microwave liver ablation," *IEEE Trans. Biomed. Eng.*, vol. 54, no. 1, pp. 150–155, 2006.

[183] S. A. Sapareto and W. C. Dewey, "Thermal dose determination in cancer therapy," *Int. J. Radiat. Oncol. Biol. Phys.*, vol. 10, no. 6, pp. 787–800, 1984.

[184] C. Bircan and S. A. Barringer, "Determination of protein denaturation of muscle foods using the dielectric properties," *J. Food Sci.*, vol. 67, no. 1, pp. 202–205, 2002.

[185] R. Scapaticci, V. Lopresto, R. Pinto, M. Cavagnaro, and L. Crocco, "Monitoring thermal ablation via microwave tomography: An ex vivo experimental assessment," *Diagnostics*, vol. 8, no. 4, p. 81, 2018.

[186] M. Lazebnik, M. C. Converse, J. H. Booske, and S. C. Hagness, "Ultrawideband temperature-dependent dielectric properties of animal liver tissue in the microwave frequency range," *Phys. Med. Biol.*, vol. 51, no. 7, p. 1941, 2006.

[187] V. Lopresto, R. Pinto, and M. Cavagnaro, "Experimental characterisation of the thermal lesion induced by microwave ablation," *Int. J. Hyperthermia*, vol. 30, no. 2, pp. 110–118, 2014.

[188] D. D. Yero, F. G. González, D. Van Troyen, and G. A. Vandenbosch, "Dielectric Properties ofEx VivoPorcine Liver Tissue Characterized at Frequencies Between 5 and 500 kHz When Heated at Different Rates," *IEEE Trans. Biomed. Eng.*, vol. 65, no. 11, pp. 2560–2568, 2018.

[189] R. Scapaticci, G. G. Bellizzi, M. Cavagnaro, V. Lopresto, and L. Crocco, "Exploiting microwave imaging methods for real-time monitoring of thermal ablation," *Int. J. Antennas Propag.*, vol. 2017, 2017.

[190] S. Kidera, L. M. Neira, B. D. Van Veen, and S. C. Hagness, "TDOA-based microwave imaging algorithm for real-time microwave ablation monitoring," *Int. J. Microw. Wirel. Technol.*, vol. 10, no. 2, pp. 169–178, 2018.

[191] T. S. England and N. A. Sharples, "Dielectric properties of the human body in the microwave region of the spectrum," *Nature*, vol. 163, no. 4143, p. 487, 1949.

[192] S. S. Chaudhary, "Dielectric properties of normal and malignant human breast tissues at radiowave and microwave frequencies," *Indian J Biochem Biophs*, vol. 21, pp. 76–79, 1984.

[193] A. J. Surowiec, S. S. Stuchly, J. R. Barr, and A. Swarup, "Dielectric properties of breast carcinoma and the surrounding tissues," *IEEE Trans. Biomed. Eng.*, vol. 35, no. 4, pp. 257–263, 1988.

[194] A. M. Campbell and D. V. Land, "Dielectric properties of female human breast tissue measured in vitro at 3.2 GHz," *Phys. Med. Biol.*, vol. 37, no. 1, p. 193, 1992.

[195] S. Salahuddin, E. Porter, P. M. Meaney, and M. O'Halloran, "Effect of logarithmic and linear frequency scales on parametric modelling of tissue dielectric data," *Biomed. Phys. Eng. Express*, vol. 3, no. 1, p. 015020, 2017.

[196] J. Barthel, K. Bachhuber, R. Buchner, and H. Hetzenauer, "Dielectric spectra of some common solvents in the microwave region. Water and lower alcohols," *Chem. Phys. Lett.*, vol. 165, no. 4, pp. 369–373, 1990.

[197] J. Sebek, R. Bortel, and P. Prakash, "Broadband lung dielectric properties over the ablative temperature range: Experimental measurements and parametric models," *Med. Phys.*, vol. 46, no. 10, pp. 4291–4303, 2019, doi: 10.1002/mp.13704.

[198] W. C. Dewey, "Arrhenius relationships from the molecule and cell to the clinic," *Int. J. Hyperthermia*, vol. 10, no. 4, pp. 457–483, 1994.

[199] S. Curto, M. Taj-Eldin, D. Fairchild, and P. Prakash, "Microwave ablation at 915 MHz vs 2.45 GHz: A theoretical and experimental investigation," *Med. Phys.*, vol. 42, no. 11, pp. 6152–6161, 2015.

[200] E. Alanen, T. Lahtinen, and J. Nuutinen, "Variational formulation of open-ended coaxial line in contact with layered biological medium," *IEEE Trans. Biomed. Eng.*, vol. 45, no. 10, pp. 1241–1248, 1998.

[201] P. M. Meaney, A. P. Gregory, J. Seppälä, and T. Lahtinen, "Open-ended coaxial dielectric probe effective penetration depth determination," *IEEE Trans. Microw. Theory Tech.*, vol. 64, no. 3, pp. 915–923, 2016.

[202] A. P. O'rourke *et al.*, "Dielectric properties of human normal, malignant and cirrhotic liver tissue: in vivo and ex vivo measurements from 0.5 to 20 GHz using a precision open-ended coaxial probe," *Phys. Med. Biol.*, vol. 52, no. 15, p. 4707, 2007.

[203] E. Porter *et al.*, "Minimum information for dielectric measurements of biological tissues (MINDER): A framework for repeatable and reusable data," *Int. J. RF Microw. Comput.-Aided Eng.*, vol. 28, no. 3, p. e21201, 2018.

[204] G. Maenhout, T. Markovic, I. Ocket, and B. Nauwelaers, "Effect of Open-Ended Coaxial Probe-to-Tissue Contact Pressure on Dielectric Measurements," *Sensors*, vol. 20, no. 7, p. 2060, 2020.

[205] G. Galloro, *Revisiting Barrett's Esophagus*. Springer, 2019.

Appendix A: Supplemental Data for Chapter 6

A.1 Piecewise linear function for measured dielectric data

The piecewise linear functions used to model the measured dielectric datasets in chapter 6 follows the below form:

$$\hat{d}_{e,p}\,[f,T] = \begin{cases} \frac{b_0(f)\cdot(T_1-T)+b_1(f)\cdot(T-20)}{T_1-20}, & 20\,°C < T < T_1, \\ \frac{b_1(f)\cdot(T_2-T)+b_2(f)\cdot(T-T_1)}{T_2-T_1}, & T_1 < T < T_2, \\ b_2(f), & T_2 < T < 130\,°C, \end{cases} \tag{1}$$

where $\hat{d}_{e,p}\,[f,T]$ is the parametrized envelope of the measured values, T_1 and T_2 are the transition temperatures between the above mentioned temperature intervals, and $b_0(f)$, $b_1(f)$ and $b_2(f)$ are frequency-dependent fitting coefficients. Quadratic functions were chosen to model each frequency dependent fitting coefficient based on the shape of the data along the frequency axis:

$$b_0(f) = b_{01}\cdot f^2 + b_{02}\cdot f + b_{03}, \tag{2}$$
$$b_1(f) = b_{11}\cdot f^2 + b_{12}\cdot f + b_{13}, \tag{3}$$
$$b_2(f) = b_{21}\cdot f^2 + b_{22}\cdot f + b_{23}, \tag{4}$$

where b_{01}, b_{02}, b_{03}, b_{11}, b_{12}, b_{13}, b_{21}, b_{22} and b_{23} are fitting coefficients. The linear least squares (LS) optimization described in [197] was utilized to estimate all nine fitting coefficients as well as for the given transition temperatures T_1 and T_2.

Calculated coefficients of the proposed temperature-dependent functions for overall, slow, medium and fast heating rate data are summarized in Table A-1 to Table A-4. Calculated coefficients of the proposed thermal dose-dependent dielectric properties are summarized in Table A-5. All of the tables include standard deviation for their corresponding data.

Table A-1: Overall data coefficients for the piecewise functions for the temperature dependent dielectric properties of *ex vivo* bovine liver.

	ϵ_r(T) Mean env.	ϵ_r(T) Upper env.	ϵ_r(T) Lower env.	std(T) of ϵ_r	σ_{eff}(T) Mean env.	σ_{eff}(T) Upper env.	σ_{eff}(T) Lower env.	std(T) of σ_{eff}
T_1	90	103	79	105	89	92	76	105
T_2	108	111	98	108	108	113	106	111
b_{01}	0.41	0.26	0.38	-0.05	0.06	0.13	0.05	0.03
b_{02}	-4.48	-3.00	-4.33	0.51	0.32	0.04	0.35	-0.11
b_{03}	56.00	59.66	54.24	-0.69	0.67	1.01	0.45	0.14
b_{11}	0.59	0.44	0.49	0.13	0.00	0.01	-0.02	0.01
b_{12}	-5.11	-3.97	-4.33	-1.10	0.22	0.23	0.28	0.03
b_{13}	40.31	42.75	33.20	11.11	0.99	1.59	0.68	0.33
b_{21}	0.14	-0.01	0.06	0.10	-0.01	0.02	-0.01	0.00
b_{22}	-1.27	-0.30	-0.64	-0.82	0.08	0.06	0.03	0.02
b_{23}	8.31	11.58	3.19	4.00	0.09	0.11	-0.02	0.11

Table A-2: Slow heating rate Coefficients for the piecewise functions for the temperature dependent dielectric properties of *ex vivo* bovine liver.

	ϵ_r(T) Mean env.	ϵ_r(T) Upper env.	ϵ_r(T) Lower env.	std(T) of ϵ_r	σ_{eff}(T) Mean env.	σ_{eff}(T) Upper env.	σ_{eff}(T) Lower env.	std(T) of σ_{eff}
T_1	97	99	97	105	101	105	98	105
T_2	105	106	104	100	106	100	102	100
b_{01}	0.24	0.22	0.28	-0.03	0.08	0.12	0.04	0.05
b_{02}	-3.08	-2.84	-3.53	0.40	0.25	0.13	0.36	-0.14
b_{03}	54.61	60.01	51.94	3.75	0.70	0.93	0.54	0.19
b_{11}	0.42	0.27	0.36	-0.05	0.02	0.01	0.01	0.01
b_{12}	-3.65	-2.35	-3.53	0.53	0.14	0.16	0.23	-0.02
b_{13}	40.65	39.39	39.29	1.32	0.69	0.77	0.53	0.21
b_{21}	0.28	0.06	0.16	0.22	0.00	0.00	0.00	0.00
b_{22}	-2.38	-0.65	-1.40	-1.79	0.03	0.13	0.00	0.04
b_{23}	11.28	9.71	7.58	5.33	0.03	-0.05	0.02	0.07

Table A-3: Medium heating rate coefficients for the piecewise functions for the temperature dependent dielectric properties of *ex vivo* bovine liver.

	ϵ_r(T) Mean env.	ϵ_r(T) Upper env.	ϵ_r(T) Lower env.	std(T) of ϵ_r	σ_{eff}(T) Mean env.	σ_{eff}(T) Upper env.	σ_{eff}(T) Lower env.	std(T) of σ_{eff}
T_1	88	106	75	106	90	92	72	106
T_2	111	107	96	108	111	113	105	108
b_{01}	0.42	0.43	0.44	-0.08	0.06	0.06	0.06	0.01
b_{02}	-4.51	-4.45	-4.69	0.62	0.29	0.23	0.31	-0.07
b_{03}	54.78	54.68	53.75	-3.33	0.77	1.02	0.53	0.12
b_{11}	0.63	0.84	0.53	0.33	0.00	0.02	-0.01	0.02
b_{12}	-5.34	-7.01	-4.46	-2.79	0.20	0.17	0.22	0.06
b_{13}	40.23	45.91	37.63	19.66	1.10	1.29	1.04	0.39
b_{21}	0.13	0.15	0.09	0.03	-0.01	0.01	-0.01	-0.01
b_{22}	-1.30	-1.35	-1.05	-0.18	0.12	0.07	0.06	0.06
b_{23}	8.31	10.53	7.08	1.70	0.17	0.10	0.08	0.15

Table A-4: Fast heating rate coefficients for the piecewise functions for the temperature dependent dielectric properties of *ex vivo* bovine liver.

	ϵ_r(T) Mean env.	ϵ_r(T) Upper env.	ϵ_r(T) Lower env.	std(T) of ϵ_r	σ_{eff}(T) Mean env.	σ_{eff}(T) Upper env.	σ_{eff}(T) Lower env.	std(T) of σ_{eff}
T_1	94	93	93	101	95	95	95	100
T_2	104	105	100	105	103	104	99	102
b_{01}	0.40	0.58	0.30	0.13	0.05	0.05	0.04	0.00
b_{02}	-4.46	-5.73	-3.77	-0.85	0.33	0.33	0.33	-0.01
b_{03}	53.13	54.86	51.25	1.10	0.59	0.69	0.49	0.09
b_{11}	0.72	0.70	0.70	0.03	-0.01	-0.01	-0.01	0.00
b_{12}	-6.30	-6.19	-6.20	-0.28	0.29	0.30	0.29	0.02
b_{13}	46.05	49.71	44.80	4.40	1.21	1.51	0.96	0.30
b_{21}	0.06	0.11	0.03	0.04	0.00	0.00	0.00	0.00
b_{22}	-0.67	-1.07	-0.40	-0.34	0.05	0.04	0.05	0.00
b_{23}	6.43	8.19	5.57	1.57	0.10	0.14	0.07	0.05

Table A-5: Overall data coefficients for the piecewise functions for the thermal dose dependent dielectric properties of *ex vivo* bovine liver

	ϵ_r(TD) Mean env.	ϵ_r(TD) Upper env.	ϵ_r(TD) Lower env.	std(TD) of ϵ_r	σ_{eff}(TD) Mean env.	σ_{eff}(TD) Upper env.	σ_{eff}(TD) Lower env.	std(TD) of σ_{eff}
TD_1	12.08	21.08	2.08	21.08	13.08	21.08	5.08	21.08
TD_2	22.96	22.96	18.96	22.96	22.96	22.96	19.96	22.96
b_{01}	0.34	0.20	0.12	-0.07	0.07	0.16	0.04	0.04
b_{02}	-4.21	-3.04	-2.86	0.61	0.36	0.01	0.47	-0.14
b_{03}	56.46	62.32	50.63	-1.42	0.54	1.11	0.19	0.14
b_{11}	0.60	0.37	0.63	0.13	0.00	0.00	-0.01	0.01
b_{12}	-5.20	-3.18	-5.78	-1.17	0.22	0.25	0.32	0.04
b_{13}	44.37	41.88	49.94	12.56	1.01	1.19	0.73	0.35
b_{21}	0.15	0.02	0.10	0.10	-0.01	0.02	-0.01	0.00
b_{22}	-1.39	-0.50	-0.86	-0.79	0.08	0.03	0.06	0.02
b_{23}	8.95	10.43	3.47	3.45	0.08	0.12	0.00	0.11

A.2 Fitting errors

To assess the goodness of the fit, $\hat{d}_{e,p}(f,T)$, a histogram of RMSE values across all 401 frequencies was computed for each envelope and dielectric property type as a function of temperature (similar to [197]), and is shown in Figure A-1. In the shown histograms, one can observe low average values of error for each envelope, which are specifically 1.06 for average, 6.92 for upper, 2.52 for lower and 1.84 for standard deviation in case of relative permittivity. In case of effective conductivity, the respective errors are 0.0051, 0.0505, 0.0083 and 0.0051 S/m.

Figure A-2 illustrates the error for each envelope computed as a function of thermal isoeffective dose. One can observe low average values of error for each envelope, which are specifically 1.96 for average, 6.71 for upper, 3.49 for lower and 3.89 for standard deviation in case of relative permittivity. In case of effective conductivity, the respective errors are 0.0055, 0.0716, 0.0081 and 0.0097 S/m.

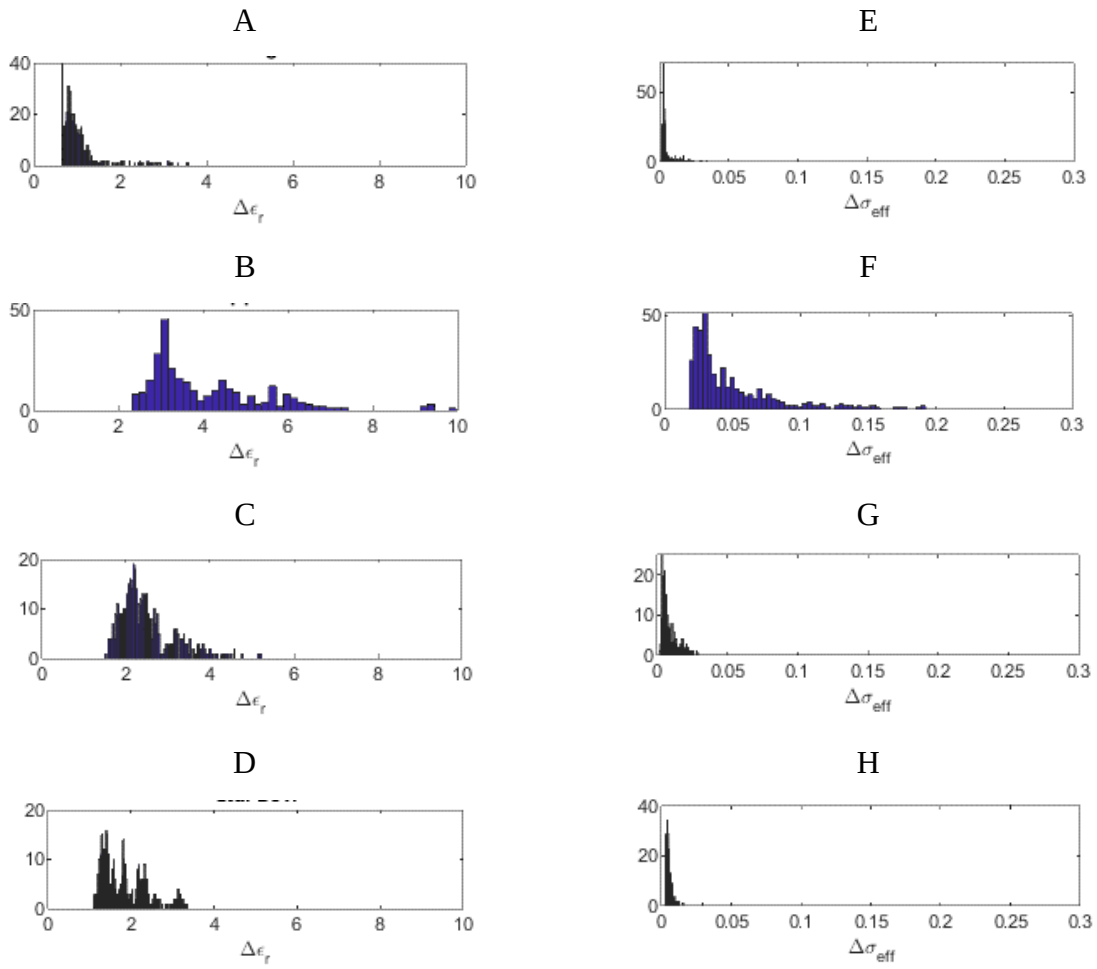

Figure A-1: Error histograms of the individual parametrized envelopes $\widehat{\boldsymbol{d}}_{e,p}(\boldsymbol{f},\boldsymbol{T})$ for temperature dependent data. Left column shows mean (A), upper (B), lower (C), and standard deviation (D) envelope errors for relative permittivity. Right column shows mean (E), upper (F), lower (G), and standard deviation (H) envelope errors for effective conductivity.

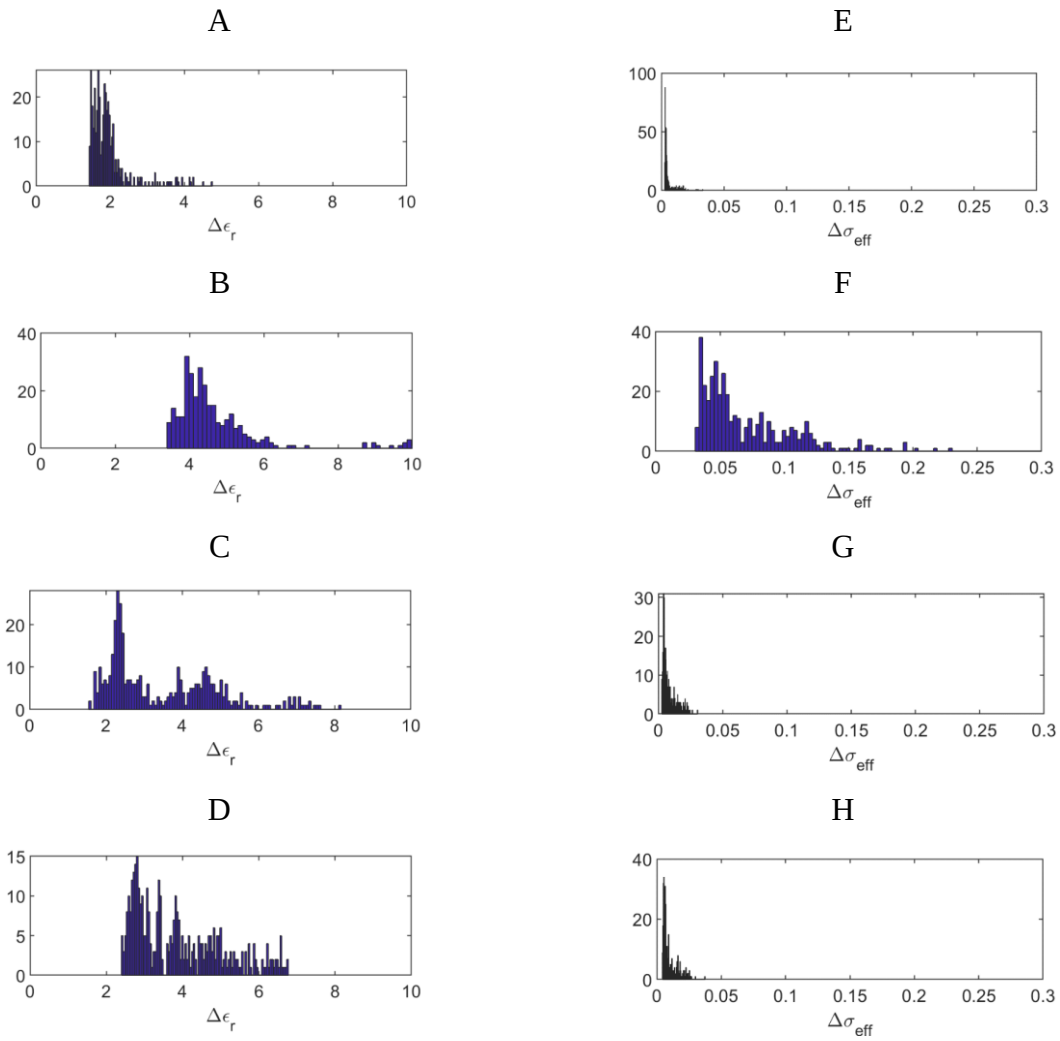

Figure A-2: Error histograms of the individual parametrized envelopes $\widehat{\boldsymbol{d}}_{e,p}(\boldsymbol{f},\boldsymbol{T})$ for thermal dose dependent data. Left column shows mean (A), upper (B), lower (C), and standard deviation (D) envelope errors for relative permittivity. Right column shows mean (E), upper (F), lower (G), and standard deviation (H) envelope errors for effective conductivity.

A.3 Details of the computational model for simulating microwave ablation

We employed finite element method (FEM) simulations, implemented using COMSOL Multiphysics v5.3, to model electromagnetic power absorption and heat transfer during microwave ablation with the interstitial dipole antennas tuned to operate at 2.45 (dipole tip length = 10.9 mm) and 5.8 GHz (dipole tip length = 5 mm). Due to the cylindrically symmetric geometry of the applicator, the 3D geometry can be modeled with a 2D axially symmetric model. The model geometry illustrated in Figure A-3. The solver computes the electric fields in the model by solving the Helmholtz wave equation:

$$\nabla^2\mathbf{E} - k_0^2\left(\epsilon_r - \frac{j\sigma}{\omega\epsilon_0}\right)\mathbf{E} = 0 \qquad (5)$$

where $\mathbf{E}\,[\mathrm{V}\cdot\mathrm{m}^{-1}]$ is the electric field, k_0 is the free space wave-number, ϵ_r is the relative permittivity, $\sigma\,[\mathrm{S}\cdot\mathrm{m}^{-1}]$ is the effective electrical conductivity, $\omega\,[\mathrm{rads}\cdot\mathrm{s}^{-1}]$ is the angular frequency, and $\epsilon_0\,[\mathrm{F}\cdot\mathrm{m}^{-1}]$ is the permittivity of free space. Microwave power was applied to the coaxial input port defined on the proximal end of the applicator as illustrated in Figure A-3. A first-order scattering boundary condition was used on the external surfaces of the model as:

$$\mathbf{n}\times(\nabla\times\mathbf{E}) - jk\mathbf{n}\times(\mathbf{E}\times\mathbf{n}) = 0 \qquad (6)$$

where $\mathbf{n}$ is normal vector to the boundary. Time-averaged electromagnetic power losses are calculated from the computed electric field using

$$Q_{em} = \frac{1}{2}\sigma|\mathbf{E}|^2 \qquad (7)$$

Electromagnetic power loss is coupled to the heat equation in order to compute the temperature profile inside the tissue:

$$\rho c_l \frac{\partial T}{\partial t} = \nabla \cdot (k \cdot \nabla T) + Q_{em} \quad (8)$$

where T [K] is temperature of the tissue, ρ is the density of tissue (1050 kg/m3), c_l [J/kg·K] is the heat capacity of tissue at constant pressure, and k [W/m·K] is the thermal conductivity of liver. The initial temperature of the tissues was set to 37 °C. Other than relative permittivity and effective conductivity, the heat capacity c_l and thermal conductivity k are other temperature-dependent tissue parameters. The temperature calculated from solving Equation 4 is used to update temperature dependent physical properties of the tissue at each time step taken by the solver. Temperature-dependent models of the heat capacity and thermal conductivity are summarized in Table A-6. Updated parameters are used in the next time step to compute new values for the electric field and temperature. This procedure continues for the defined simulation time.

Table A-6: Tissue physical properties used in the simulations.

Parameter	Unit	Value @ 37 °C	Temperature-dependent formula
Volumetric heat capacity, ρc_l [137]	J/(m³·K)	4,000,000	$\rho c(T) = \begin{cases} \rho c_0 & for\ T < (100 - \frac{\Delta T}{2}) \\ \frac{\rho c_0 + \rho c_v}{2} + \frac{\rho_w . L . C}{\Delta T} & for\ (100 - \frac{\Delta T}{2}) < T < (100 + \frac{\Delta T}{2}) \\ \rho c_v & for\ T > (100 + \frac{\Delta T}{2}) \end{cases}$
Thermal conductivity, k [137]	W/(m·K)	0.5	$k(T) = \begin{cases} k_0 + \Delta k[T - T_0] & T \leq 373\ K \\ k_0 + \Delta k[373 - T_0] & T > 373\ K \end{cases}$

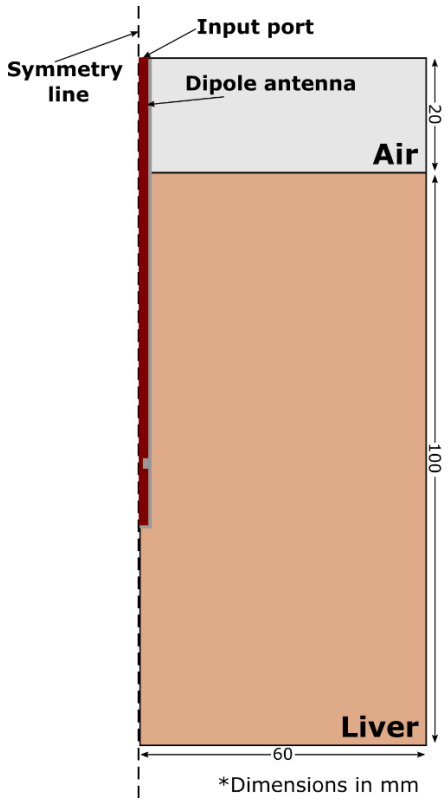

Figure A-3: Illustration of the geometry employed in computational models.

A.4 Change of effective conductivity slope at low temperatures

An important observation is the change of the effective conductivity slope in the first temperature region from positive values at lower frequencies (0.5–1.64 GHz) to negative values at higher frequencies (1.64–6 GHz). The positive slope of effective conductivity at low temperatures is in agreement with the measurements in [186], where broadband dielectric properties were presented up to temperatures of ~65 °C. Figure A-4 shows slope of the effective conductivity at low temperatures as a function of frequency.

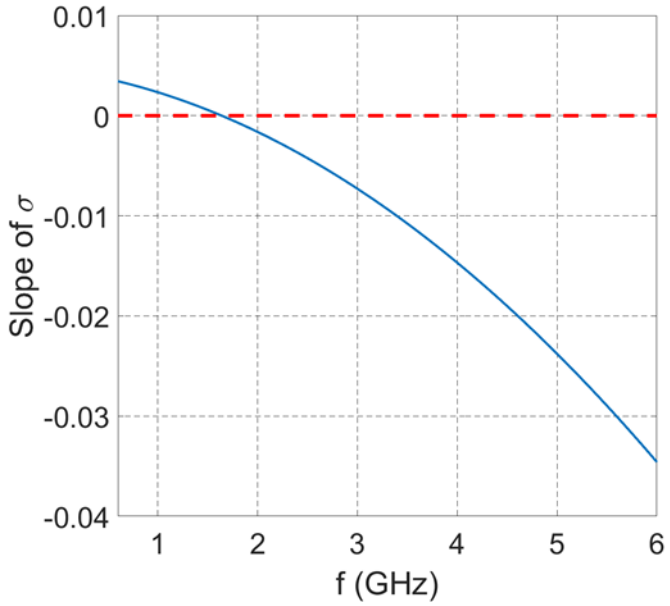

Figure A-4: Change of effective conductivity slope at low temperatures as a function of frequency

A.5 Max/Min envelopes vs. mean ± 2×STD envelopes

As illustrated in Figure A-5, Max/Min envelopes are similar to mean ± 2×STD envelopes. Thus, the fit function from these envelopes lead to similar fir function coefficients. Standard deviation for the overall data, SH, MH and FH rates, thermal dose-dependent data are included in Table A-1 to Table A-5.

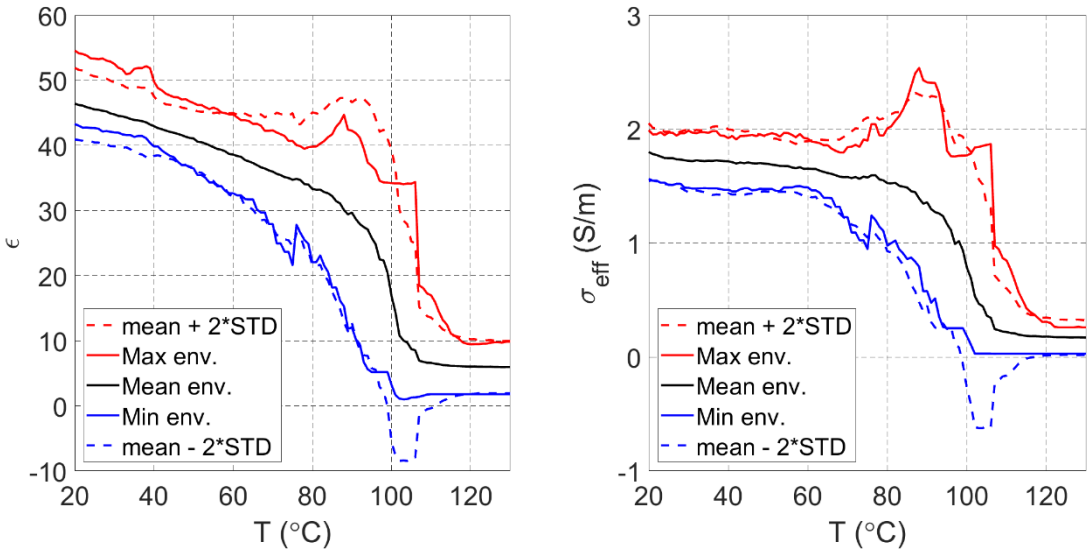

Figure A-5: Comparison of maximum/minimum envelopes with mean ± 2×STD of the measured data at 2.45 GHz.

Appendix B: Applicator Fabrication Example

The process for fabricating a water-cooled coaxial microwave ablation applicator is described. The applicator consists of a monopole antenna made of coaxial cable, concentric tubes for cooled water circulation, water inflow and outflow ports, and a microwave connector. Table B-1 shows example diameter and wall thickness values in gauge, millimeter and inch units.

The following parts are used in the fabrication of our example microwave applicator. Example photo of each part is illustrated in Figure B-1.

1) **Coaxial cable:** semi-rigid UT-034-M17 (M17/154-00001)
2) **Connector:** Huber+Suhner, 21_SMA-50-1-1/111_NE
3) **Inflow tube:** American Durafilm, Polyimide, ID = 0.0572'', OD = 0.0651''
4) **Outflow tube:** American Durafilm, Polyimide, ID = 0.0743'', OD = 0.0844''
5) **Y-connector:** Qosina P/N 83010, 2 female Luer lock, 3.2 mm
6) **Valve:** Qosina P/N 80460, Tuohy borst adaptor, Swivel male Luer lock female Luer lock side port
7) **Epoxy glue:** JB weld, Clearweld 5 min epoxy

Table B-1: Example dimensions of hypodermic tubes and catheters in gauge, millimeter and inch.

Needle	Nominal outer diameter			Nominal inner diameter			Nominal wall thickness		
				Not strictly defined, and may vary for a given gauge.					
Gauge	inches	mm	tol. inches (mm)	inches	mm	tol. inches (mm)	inches	mm	tol. inches (mm)
13	0.095	2.413	±0.001 (±0.025)	0.071	1.803	±0.003 (±0.076)	0.012	0.305	±0.001 (±0.025)
14	0.083	2.108	±0.001 (±0.025)	0.063	1.600	±0.003 (±0.076)	0.01	0.254	±0.001 (±0.025)
15	0.072	1.829	±0.0005 (±0.013)	0.054	1.372	±0.0015 (±0.038)	0.009	0.229	±0.0005 (±0.013)
16	0.065	1.651	±0.0005 (±0.013)	0.047	1.194	±0.0015 (±0.038)	0.009	0.229	±0.0005 (±0.013)
17	0.058	1.473	±0.0005 (±0.013)	0.042	1.067	±0.0015 (±0.038)	0.008	0.203	±0.0005 (±0.013)
18	0.050	1.270	±0.0005 (±0.013)	0.033	0.838	±0.0015 (±0.038)	0.0085	0.216	±0.0005 (±0.013)
19	0.042	1.067	±0.0005 (±0.013)	0.027	0.686	±0.0015 (±0.038)	0.0075	0.191	±0.0005 (±0.013)

(a) Coaxial cable

(b) SMA connector

(c) Polyimide tubes

(d) Y-connector

(e) Valve

(f) Epoxy glue

Figure B-1: Parts used in the fabrication of the example water-cooled microwave ablation applicator.

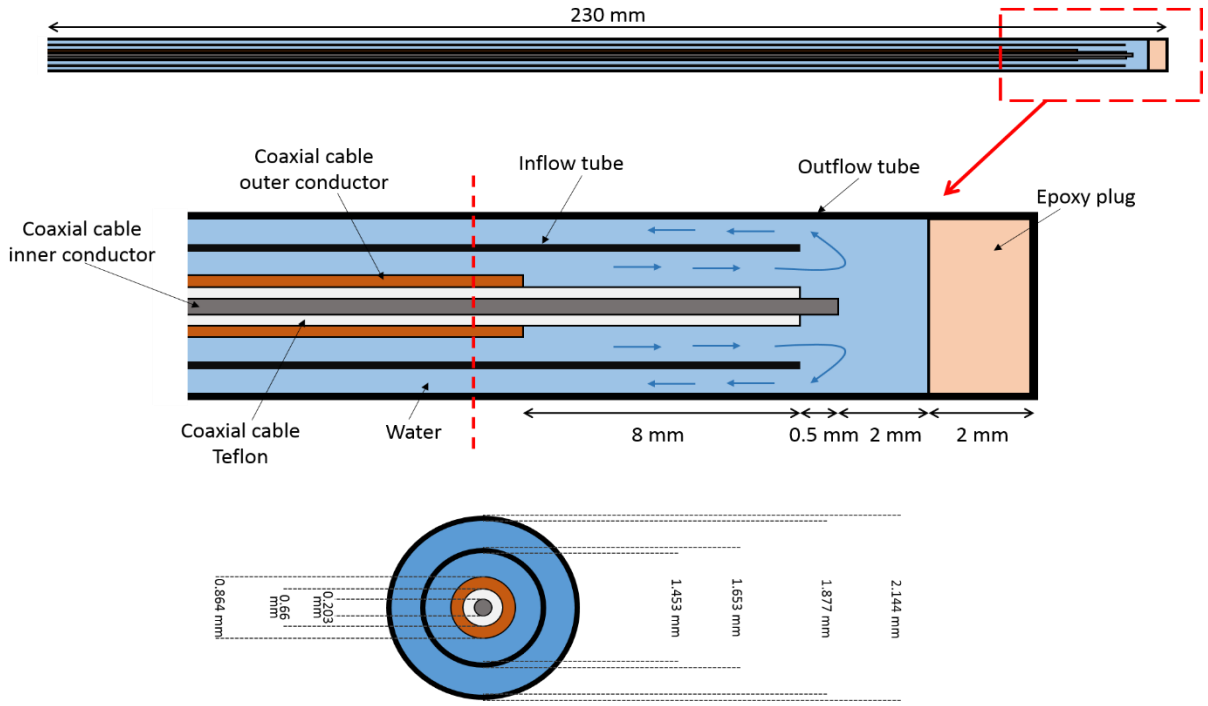

Figure B-2: Dimension and structure of the water-cooled microwave ablation applicator.

The applicator specifications are as follows and its dimensions are shown in Figure B-2. Photo of two fabricated antennas is illustrated in Figure B-3.

- Water flow: $>$ 100 ml/min
- Operation frequency: 2.45 GHz
- S_{11} @2.45 GHz in water $<$ -18 dB

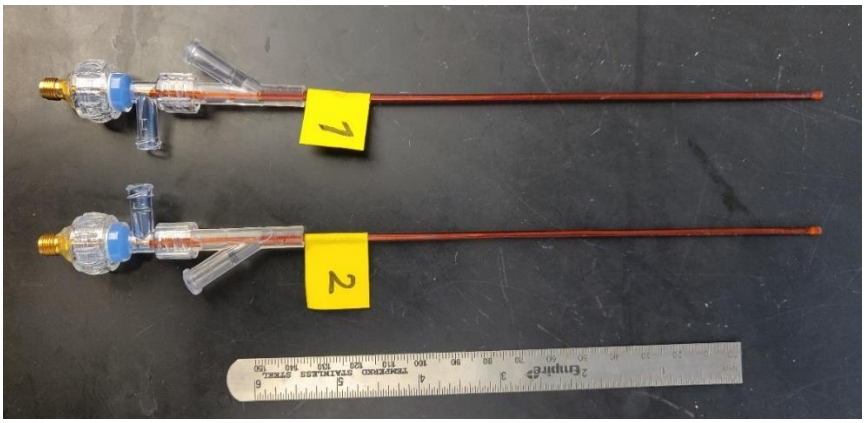

Figure B-3: Fabricated examples of the microwave ablation applicator.

B.1 Fabrication steps

Follow the following steps for building the microwave applicator shown in Figure B-3.

1) Cut a length of 225 mm of UT-034 coaxial cable.

2) In this step, we build the monopole antenna on one end of the coaxial cable piece. Strip off 8.5 mm of the outer conductor on the coaxial cable to expose the Teflon.

3) Strip off 0.5 mm of the Teflon to expose the coaxial cable inner conductor. The monopole is now complete.

4) In this step, we prepare the other end of the coaxial cable for soldering the SMA connector. Strip off a length of 2.5 mm of the outer conductor and Teflon to expose the inner conductor.

5) The SMA connector has four parts as shown in Figure B-4. Slide sleeve A onto the cable as shown in Figure B-5(a). Push insulator disk B onto the exposed inner conductor. Then, slide contact C onto the inner conductor. Pay attention that

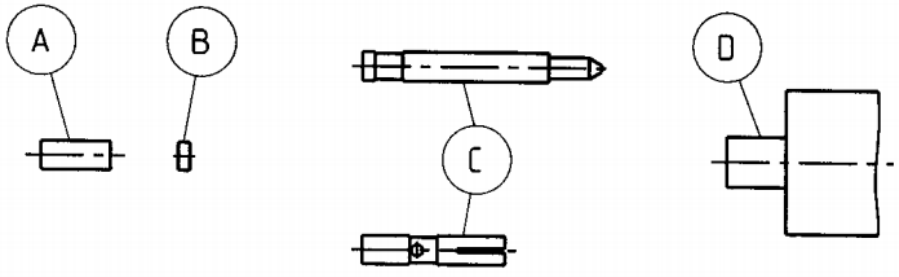

Figure B-4: Different parts of SMA connector 21_SMA-50-1-1/111_NE

contact C has two ridges on one side. This side should not face insulator disk B when mounted on the cable inner conductor. Push contact C against insulator disk B (see Figure B-5(b)) and solder it to the cable inner conductor. Apply a very small amount of solder to the hole on contact C. Remove any excess solder on contact C. You can use Dremel rotary tool with a cutting wheel to do that. Next, push sleeve A to insulator disk B and solder it to the cable outer conductor.

Finally, insert the cable from the side with contact C into SMA knot D. Since you may not have access to the tool and fixture for this step, be careful to insert the cable into the knot slowly and gently. Any excessive force would break the cable and soldered connections. You should never rotate the cable or the SMA knot. This would also break the cable. When edge of contact C is aligned with the white Teflon cylinder inside the knot, solder the cable to the knot at point Z shown in Figure B-5(c). Do not apply excessive heat and pay attention to the orientation of the cable while soldering. It is better the keep the cable and the knot in horizontal orientation and in a fixed position. This would prevent the knot to slide and misalignment of contact C inside the knot. There is usually two holes on the knot. After soldering when the knot is cooled down, apply some glue to the hole for further stability of the connection between the cable and the connector.

A good practice at this stage is to perform a continuity check with a digital multimeter. Inner conductor of the monopole antenna should be electrically

connected to contact C inside the SMA connector knot while outer conductor of the coaxial cable should be electrically connected to the SMA connector knot. There are times when continuity test is passed but the connection between the coaxial cable and the SMA connector is flawed. Look at the monopole antenna S_{11} on the vector network analyzer while the monopole is inserted into water. If you see a resonance, the connection between the SMA connector and coaxial cable is solid. It is noted that the resonance frequency may not be tuned to the operation frequency (here 2.45 GHz). This is expected as the antenna fabrication is not complete. The antenna would be resonant at its designed operation frequency when all the applicator parts such as the inflow and outflow tubes are in place and water is circulating inside the applicator.

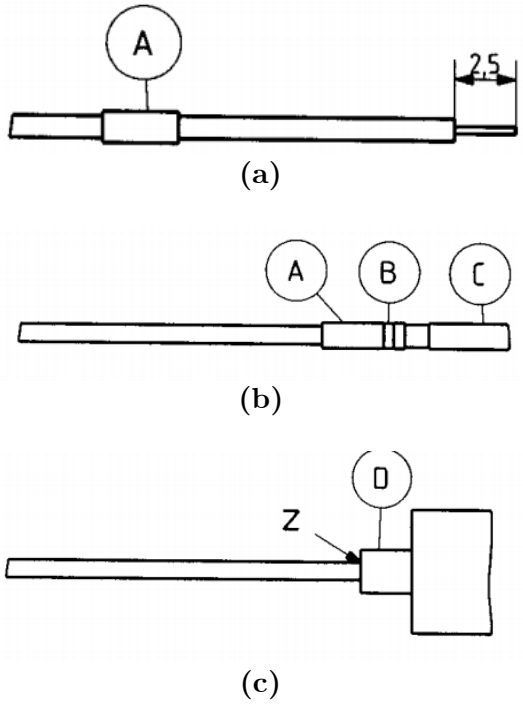

Figure B-5: Steps in soldering the SMA connector to the coaxial cable.

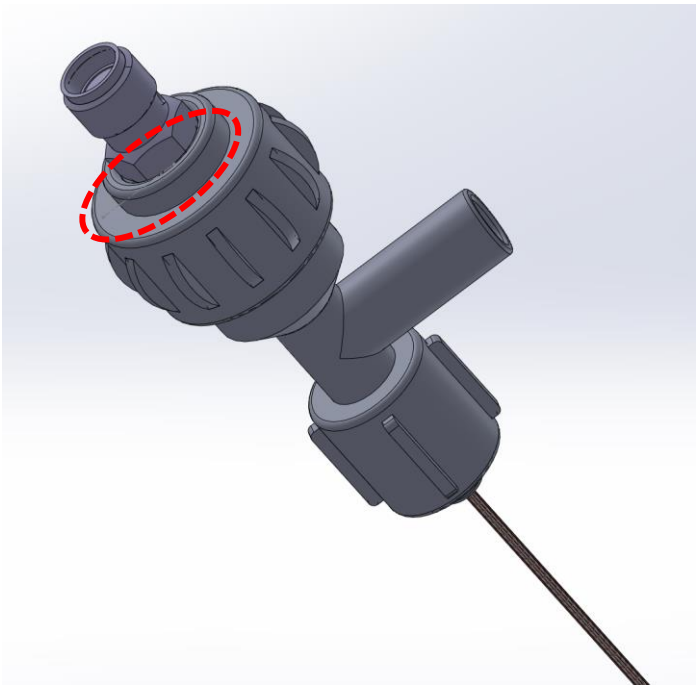

Figure B-6: Mounting of the valve onto the coaxial cable. Red indicates where epoxy glue should be applied.

6) In this step, the valve (shown in Figure B-1(e)) is attached to the antenna. The size of the aperture in the valve can be adjusted by rotating its screw. Open the aperture large enough to slide it over the coaxial cable. Slide the valve from the antenna side and push it to the SMA connector. Then, rotate the valve screw to close its aperture as tight as possible. Apply enough epoxy glue where the SMA connector meets the valve (indicated in red in Figure B-6). Be careful not to pour any glue on the threads of the SMA connector. It takes at least 30 minutes for the epoxy to dry at room temperature.

7) Cut off a length of 205 mm from the polyimide tube with outer diameter of 0.0651 in. This tube is the water inflow tube. Slide the tube over the coaxial cable until it is close to the valve Luer (see Figure B-7). The other end of the

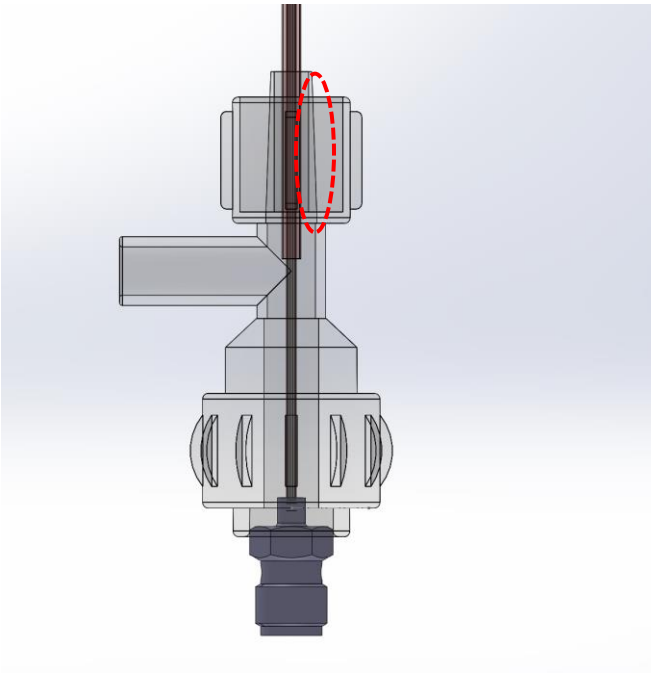

Figure B-7: Positioning of the inflow polyimide tube. The location where epoxy glue should be applied is shown in red.

tube should be aligned with the monopole antenna tip as illustrated in Figure B-2. Pour some epoxy glue onto the tube where it is inserted to the valve (indicated in red in Figure B-7). By keeping the valve in vertical orientation, the glue will move down because of gravity. It is very important not to pour excess glue because it may pass the tube opening in the valve and clog it.

8) When the epoxy glue completely dried, slide the Y-connector onto the coaxial cable and fasten it to the valve. Pay attention to align the Y-connector output Luer in the opposite direction of the valve input Luer. With this arrangement, connection to the water circulation tubing will be easier. Figure B-8 shows the applicator with the Y-connector fastened to the valve.

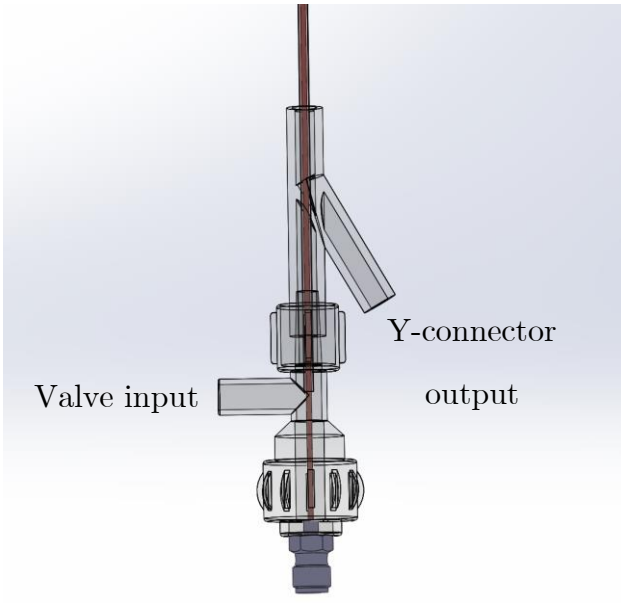

Figure B-8: Addition of the Y-connector to the applicator and its orientation with respect to the valve.

9) In this step, cut off a length of 165 mm from the polyimide tube with outer diameter of 0.0844 in. Water that flows into the applicator from the valve Luer reaches the monopole antenna at the tip of the applicator and travels back toward the Y-connector Luer inside this tube. Slide the tube onto the applicator until it reaches the Y-connector output Luer. The other end of the tube should be aligned with the monopole antenna tip as illustrated in Figure B-2. The tube end should not pass the Luer opening. Fix the applicator in upright position and pour epoxy glue to the Y-connector opening where the tube has been inserted (indicated in red in Figure B-9). Epoxy will move downward due to gravity. Do not pour excessive amount of epoxy as it may clog the tube opening. You may cut off a longer tube length in this step and size it based on Figure B-2 when the epoxy is dry.

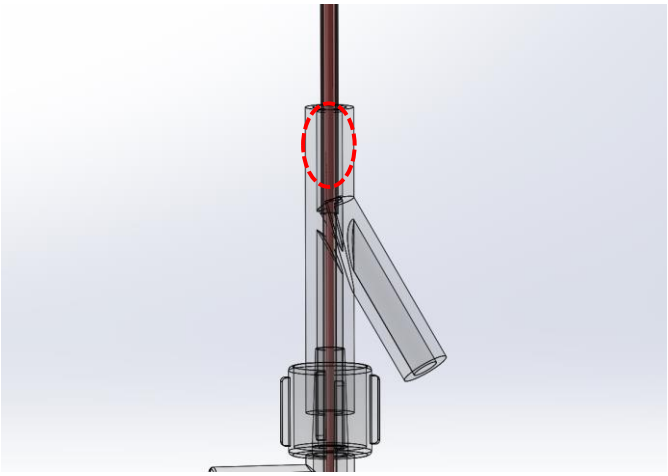

Figure B-9: Addition of the outflow polyimide tube. Red indicates where epoxy glue should be applied.

10) In the final step of the fabrication, tip of the applicator is blocked by epoxy glue to have a closed water circulation path. Fix the applicator in upright position. Pour a very small amount of glue into the applicator tip. Figure B-10 shows the location of the epoxy glue at the tip of the applicator in red.

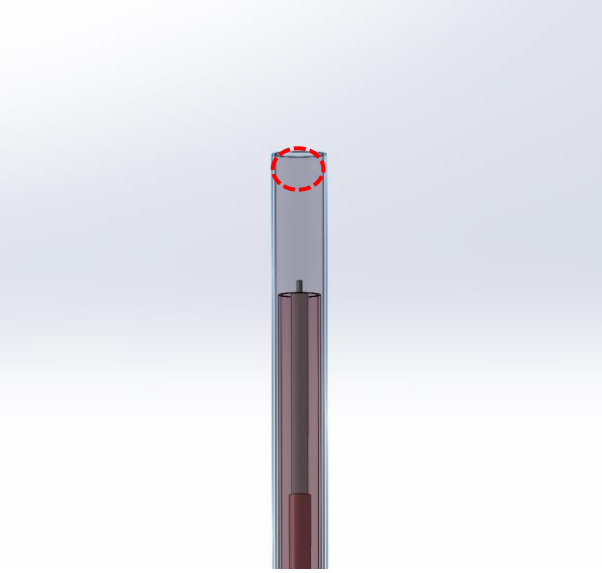

Figure B-10: Alignment of the inflow and outflow polyimide tubes with respect to the monopole antenna at the tip of the applicator. Red circle indicates where epoxy glue is applied to block the applicator tip and close the water circulation circuit.

Two of the example antenna were built as shown in Figure B-3. Performance of the applicator is evaluated in terms of antenna return loss and ablation profile inside tissue (usually *ex vivo* bovine liver). However, one preliminary test is to measure the antenna return loss in water. Water dielectric properties (relative permittivity and effective conductivity) is higher than tissue but it can provide us with a rough approximation of the antenna return loss. Measured return loss of the fabricated applicators in water is plotted in Figure B-11. Return loss is larger than 21 dB at 2.45 GHz for both antennas.

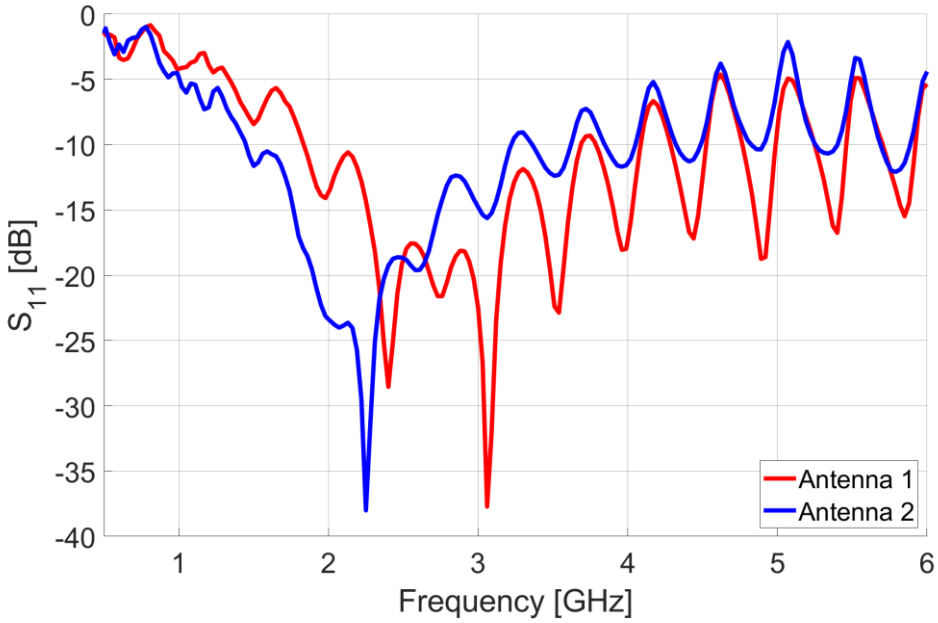

Figure B-11: Measure return loss of the fabricated antenna shown in Figure B-3 inside water.